cces
Leading in Education, Research and Decision Support
Competence Center Environment and Sustainability
COGEAR: COupled seismogenic GEohazards in Alpine Regions

COGEAR

MODULE 3:

Joint inversion of surface waves and refracted P- and S-waves

Del. No.: 3.1.1

Author: Juerg Schuler

Institute of Applied and Environmental
Geopyhsics

August, 1 2008

Eidgenössische Technische Hochschule Zürich
Swiss Federal Institute of Technology Zurich

Joint inversion of surface waves and refracted P- and S-waves

MASTER OF SCIENCE THESIS

submitted by

Juerg Schuler

Department of Earth Sciences
Institute of Applied and Environmental Geopyhsics

August 2008

Thesis title:	Joint inversion of surface waves and refracted P- and S-waves
Author:	Juerg Schuler
Date:	August 2008
Principal adviser:	Dr. Jan van der Kruk
Co-adviser:	Sabine Latzel
Co-examiner:	Prof. Dr. Evert Slob
	Prof. Dr. Hansruedi Maurer

A thesis submitted to the Institute of Geophysics at ETH Zürich in partial fulfillment of the requirements for the degree of Master of Science in Applied Geophysics. This thesis finishes the first two year joint master program shared with ETH Zürich, TU Delft and RWTH Aachen.

IDEA League
A focused network of leading European universities
of science and technology

Abstract

Characterization of shallow subsurface layer properties is of particular interest for geotechnical engineering. Classical seismic techniques often encounter difficulties in determining the properties for the uppermost thirty meters. A powerful method, which delivers material property information in this depth range, makes use of dispersive surface waves.
We present a method, which inverts dispersive Love and Rayleigh waves together with first break compressional (P) and shear (S) waves to obtain medium properties of a layered earth. First step involves the calculation of the phase velocity spectra. A wave field and frequency-wavenumber method to calculate these spectra were compared. Superior resolution was achieved by the frequency-wavenumber method using relatively few receivers with respect to the wave field method. Next step is to pick dispersion curves in the phase velocity spectra and invert these curves. In addition, first breaks of P- and S-wave seismograms were picked and jointly inverted using both a Pareto and relative objective approach. A global and local optimization scheme is applied in the inversion process to find model parameters that represent the subsurface parameters.
Synthetic datasets demonstrated that joint inversion of Rayleigh and Love waves and refracted waves returned more accurate and better constrained results than separate inversions. Consequently, the joint Rayleigh, Love and first arrival P- and S-wave inversions were able to determine all medium properties well, which is due to the complementary information from the different methods. Shallow layer information was best obtained by the surface wave method whereas deeper layer properties were better reconstructed using the first arrival inversion.
To verify the applicability of our method, a geophysical campaign in poorly consolidated alluvia was performed in Visp, Switzerland. By the use of the method, a three layer subsurface model was found to be representative for the present geology integrating the S-wave velocity, thickness, Poisson's ratio, and guess of the material density. The S-wave velocity and thickness of the upper two layers could be well determined whereas the velocity of the lower halfspace could not be accurately reconstructed due to the low signal to noise ratio for the refracted waves coming from the halfspace. The obtained results will be taken into account when interpreting measurements of the new seismological station that will be installed there soon.

Contents

1. Introduction **1**

2. Basic concepts **5**
- 2.1. Notational convention 5
- 2.2. Temporal and spatial Fourier transform 5
- 2.3. Temporal and spatial sampling 6
- 2.4. Wave propagation in homogeneous media 7
  - 2.4.1. Cauchy-Navier equation of motion 7
  - 2.4.2. P-waves 8
  - 2.4.3. S-waves 9
- 2.5. Medium parameters 9
  - 2.5.1. Quality factor 9
  - 2.5.2. Poisson's ratio 10
  - 2.5.3. Density estimation 11
- 2.6. Refraction and reflection seismic 11
- 2.7. Surface wave method 14

3. Surface waves **17**
- 3.1. Love waves 17
  - 3.1.1. Homogeneous layer over halfspace 19
- 3.2. Rayleigh waves 22

4. Phase velocity spectra calculation **25**
- 4.1. Resolving power of transformation methods 27

5. Inversion theory **31**
- 5.1. Cost-functions for inversion 32
  - 5.1.1. Separate and joint inversion of refracted P- and S-waves 32
  - 5.1.2. Separate inversion of Love and Rayleigh waves 32
  - 5.1.3. Joint inversion of Love and Rayleigh waves 33
  - 5.1.4. Joint Pareto inversion of refraction and dispersion data 33
  - 5.1.5. Joint relative inversion of refraction and dispersion data 34
- 5.2. Inversion methods 35
  - 5.2.1. Global search methods 35
  - 5.2.2. Local search methods 35
- 5.3. Applied approach 36
  - 5.3.1. Applied global search scheme 37

5.3.2. Applied local search scheme . . . 38

6. Synthetic data **39**
6.1. Models . . . 39
6.2. Processing . . . 40
6.3. Separate and joint inversion results of Love and Rayleigh waves . . . 40
6.3.1. Multilayer inversion results . . . 41
6.3.2. Frequency reduction . . . 43
6.4. Integration of refraction information to find the optimized search space . . . 45
6.5. Joint inversion of surface waves and refracted waves . . . 47
6.6. Discussion . . . 48

7. Experimental data **51**
7.1. Data acquisition . . . 51
7.1.1. Three component P- and S-wave measurements . . . 51
7.1.2. Measured data Visp . . . 52
7.2. Source quality . . . 54
7.3. Refraction analysis . . . 54
7.4. Phase velocity spectra calculation . . . 54
7.5. Validation of the assumption of lateral homogeneity . . . 57
7.6. Inversion results . . . 60
7.6.1. Separate inversion of Love and Rayleigh waves . . . 61
7.6.2. Joint inversion of Love and Rayleigh waves . . . 62
7.6.3. Joint inversion of surface waves and refracted waves . . . 63
7.7. Borehole information and comparison . . . 65
7.8. Discussion . . . 67

8. Conclusion and Outlook **69**
8.1. Future developments and applications . . . 70

Bibliography **71**

Acknowledgments **78**

A. Rayleigh wave dispersion equation **85**

B. Velocity reversal **91**

C. Extraction of refraction information **93**

D. Expanded experimental data analysis **95**
D.1. Statistics of the joint Love and Rayleigh wave inversion . . . 95

1. Introduction

In recent years, near-surface characterization became more and more important. The shallow earth subsurface contains information that is of particular interest for water resources, environmental and engineering studies. Furthermore, in geotechnical earthquake and foundation engineering, knowledge about the dynamic behaviour of a site is of importance, since the destructiveness of an earthquake is highly dependent on the subsurface properties. In the case, where an earthquake wave travels from a high to low velocity medium, a velocity-decrease is observed. A part of the energy is transformed at the media boundary and leads to an amplification of the wave amplitudes - see Figure 1.1. The high amplitudes cause a strong soil motion. Especially in mountain valleys, low velocity sediments are overlying high velocity rocks of the basement. Possible effects of earthquakes close to valleys are tried to estimate and therefore, properties of valley fills have to be characterized. The necessary information can be delivered by geophysical methods and especially from seismic shear wave analyses.

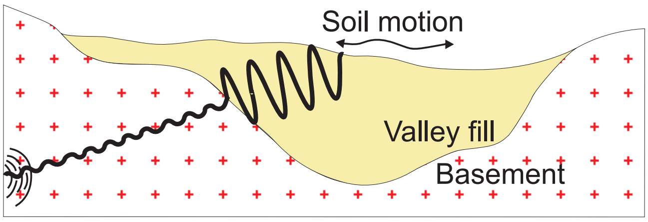

Figure 1.1: An earthquake wave travels from a high (basement) to low velocity medium (valley fill). An amplification of the wave amplitudes is observed due to the energy conservation over the media boundary. High amplitudes finally lead to strong soil motion.

In classical seismic prospecting, reflected and refracted waves are investigated to image the subsurface. However, they do not always possess the ability to uniquely resolve the shallow subsurface (0-30m) as a stand-alone technique. At shallow depth or in seismograms at short travel times, the window, where we find distinct reflections, is narrow. This so-called optimum reflection window acts consequently as a constraint to extract useful near-surface information. It is surrounded by the air, guided wave and ground roll zone (Roth et al., 1998; Robertsson, Holliger, & Green, 1996). An optimal reflection window with the surrounding waves is shown in Figure 1.2a. The air wave travels with the sonic speed directly from source to receiver whereas a guided wave represents a multiply reflected wave captured in a subsurface layer. Surface waves, like Rayleigh and Love waves, are the main components of ground roll and propagate close to the surface. They are generally the dominating part in seismic records because of their large energy content and little energy lost. For these body waves, the energy is spread on a cirle instead of a sphere. In reflection and refraction seismics, those waves and resulting amplitude events are regarded as coherent, non-random or source generated noise. Their signal is usually attenuated or removed in data processing by deconvolution, stacking and migration (Yilmaz, 2001; Strobbia, 2002).

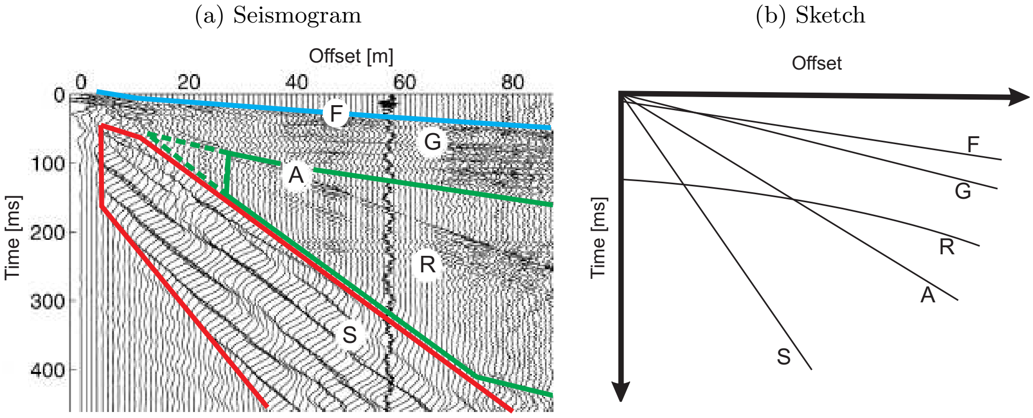
(a) Seismogram
(b) Sketch

Figure 1.2: The narrow optimal reflection window is indicated in (a) with a green line in the seismogram. It is surrounded by the guided (G) and surface wave (S). At short travel times (dashed line), reflected waves (R) are disturbed by surrounded waves and cannot be clearly identified. The air wave (A) goes here through the window, but it is easily removable. In our presented approach, we use dispersive surface waves and refracted waves (F) indicated with a red and blue line, respectively. A sketch of the seismogram is shown in (b).

In contrast to classical seismic, where surface waves are suppressed, they can be analyzed within the surface wave method (SWM) for shallow subsurface characterization. Usage of surface waves goes back to the middle of the 20^{th} century and was applied for example by Ewing et al. (1957). They employed these waves in seismology to cover the upper-mantle structure.

The physical phenomenon we are looking at is called dispersion and describes the frequency dependence of the phase velocity. Material and geometrical dispersion are distinguished. Former explains that the response of a material to waves is frequency dependent. Geometrical dispersion depicts the frequency dependence of the phase velocity due to the geometry of a medium, which is a typical feature in layered media. Surface wave techniques analyze geometrical dispersion. Using either Rayleigh or Love waves (or both), subsurface properties can be inferred since these waves are directly related to the soil stiffness. The application of surface wave methods is many-sided. On sites where no possibility exist to do an invasive investigation, e.g. waste deposits, non-invasive methods like SWM become important. The feasibility of rapid and cost-effective surveying of a target area represents another advantage. Limitations of refraction seismics can be overcome for example gradual velocity changes with depth, blinding of shallow water tables and hidden layers (Foti et al., 2003). These advantages illustrate the power of the method to characterize the shallow subsurface parameters. Research on surfaces waves in engineering seismology was mainly focusing on Rayleigh waves (Stokoe et al., 1994; Xia et al., 2005) because they can be recorded by classical vertical geophones. Love waves can only be observed, when special sources are used and horizontal geophones employed, which are sensitive to horizontal displacements. Geophones, which sample the wave movement in all spatial dimensions, are called three-component geophones and the corresponding method is referred to as 3-C seismic. In marine seismics, an additional measurement, the water pressure, is included and forms the 4-C seismic method.

In several studies (Gabriels et al., 1987; Xia J., 1999; Safani et al., 2005), shear waves were observed to be highly sensitive to soil and rock properties. The Love wave, a pure shear wave, can therefore provide useful information. Nevertheless, Love waves are not widely used. With the upcoming three component seismics, both types of surface waves can be analysed and combined to achieve the best subsurface model.

The technique that extracts useful information about the subsurface from measurements is known as inversion. In the case where different measurements are combined in such a procedure, we are speaking of a joint inversion. Separate inversions of Love, Rayleigh and refracted waves are performed and their ad-/ and disadvantages are presented in this work. A combined inversion benefits of all the advantages and renders the best possible result. Such an analysis of seismic data allows to identify compressional and shear wave velocities, Poisson's ratio, thickness and a density guess for shallow subsurface layers. The algorithms are primarily tested on synthetic datasets and finally employed onto a field dataset acquired in Visp, Switzerland.

In Chapter 2, we describe signal processing and introduce the wave propagation concept. Surface waves are explained in detail in Chapter 3 as well as the most simple case of Love wave dispersion. Chapter 4 examines the phase velocity spectra calculation with different methods and shows a comparison between selected methods. Inversion theory and schemes are covered in Chapter 5. They are tested and discussed in Chapter 6 on synthetic datasets. Finally, the attained knowledge is applied on a field dataset and discussed in Chapter 7. Conclusions are then given in Chapter 8. Further results, explanations and derivations are reflected in the Appendices.

2. Basic concepts

Mathematical terms, which are used in further expressions, are introduced in this chapter. Furthermore, basics of the wave propagation theory are presented and the terms phase and group velocity are explained. We finally describe the refraction, reflection and surface wave seismic methods.

2.1. Notational convention

A point in space is defined by three Cartesian coordinates. The space vector to this position is $\mathbf{x} = (x_1, x_2, x_3)^T$ for a right-handed system where ^{T} means transposition. Variables written in bold refer to vectors. Horizontal coordinates are x_1 and x_2 whereas x_3 points towards increasing depth. Spatial and temporal derivatives are denoted as ∂_i and ∂_t, respectively. The subscript $_i$ indicates the coordinate x_i of which the derivative is taken. According to this convention, we can formulate for instance $\boldsymbol{\nabla} = (\partial_1, \partial_2, \partial_3)^T$. Einstein's summation convention, a shorthand notation, is used to express the sum of products with subscripts. Every repeated subscript is given the value 1, 2, 3 and is added to the previous one. An example of an inner product would be

$$a_m b_m = \sum_{m=1}^{3} a_m b_m = a_1 b_1 + a_2 b_2 + a_3 b_3. \tag{2.1}$$

Small Greek subscripts also follow the summation rule, but they only take on values 1 and 2. In some cases, distinction between variables needs additional subscripts. If there already exist subscripts, additional ones are separated by comma. Capital super- or subscripts and added subscripts separated by commas are excluded from the summation rule. If subscripts occur under summation signs, they are used as running variables and do not follow the Einstein's convention. And finally, variables without any subscripts indicate equal properties in all directions.

2.2. Temporal and spatial Fourier transform

In signal processing, we often transform a time signal in space into frequency and wavenumber domain. Working in those two spectral domains can considerably simplify the analysis. The method to decompose a signal or function in sine and cosine waves is known as Fourier analysis. A forward and backward transformation from the space-time to space-frequency domain in x_1-direction and vice versa can be written as

$$G(x_1,\omega) = \int_{-\infty}^{\infty} g(x_1,t)e^{-i\omega t}dt \tag{2.2}$$

$$g(x_1,t) = \frac{1}{2\pi}\int_{-\infty}^{\infty} G(x_1,\omega)e^{i\omega t}d\omega, \tag{2.3}$$

where g indicates an arbitrary function, $\omega= 2\pi f$ the angular frequency and f temporal frequency. A spatial Fourier transformation from space-frequency to wavenumber-frequency domain in x_1-direction and vice versa reads

$$\tilde{G}(k_1,\omega) = \int_{-\infty}^{\infty} G(x_1,\omega)e^{ik_1x_1}dx_1 \tag{2.4}$$

$$G(x_1,\omega) = \frac{1}{2\pi}\int_{-\infty}^{\infty} \tilde{G}(k_1,\omega)e^{-ik_1x_1}dk_1, \tag{2.5}$$

where k describes the wavenumber. The sign convention between time and spatial Fourier transform in the exponential is opposed. Temporal and spatial Fourier transforms can also be combined in a way that we can write it in a compact form

$$g(x_1,t) = \frac{1}{(2\pi)^2}\int_{-\infty}^{\infty}\int_{-\infty}^{\infty} \tilde{G}(k_1,\omega)e^{i(\omega t-k_1x_1)}dk_1d\omega. \tag{2.6}$$

Such a transform is known as the double Fourier transform. In the following, capital letters for functions (G) are used for the space-frequency domain and the additional tilde ($\tilde{G}$) indicates wavenumber-frequency domain.

2.3. Temporal and spatial sampling

In real environment, we sample discrete and not continuous time signals at discrete spatial positions. The former section described the contiuous Fourier transformations, which can be discretized using summations. To reconstruct a continuous wave signal in time by discret sampling, our sampling interval has to fulfill the Nyquist criterium

$$f^N = \frac{1}{2\Delta t}, \tag{2.7}$$

where f^N is the Nyquist frequency. Our time sampling has to be chosen equal or smaller than Δt defined in equation 2.7. Another point related with time sampling is the record length. It should be long enough to record surface waves also at the last receiver. Since surface waves partly contain very low velocities, recording windows can achieve lengths of more than one second for long offsets considering engineering scale.

Spatial sampling has stronger effects on the resolution of dispersive phenomena. Similar to time sampling, the Nyquist relation can be applied to space. Spatial under-sampling of the wave field is avoided as long as the receiver spacing Δx_1 is equal or smaller than defined in

$$k_1^N = \frac{1}{2\Delta x_1}. \tag{2.8}$$

This expression is the spatial sampling criterium.

2.4. Wave propagation in homogeneous media

Seismology makes use of the wave propagation through the subsurface. Principally, two categories of elastic waves are distinguished: body waves and surface waves. Waves, which can occur in bounded and unbounded media, are referred to as body waves. The two types of body waves are known as longitudinal and transverse waves.

2.4.1. Cauchy-Navier equation of motion

Longitudinal waves are also known as compressional, dilatational or abbreviated P-waves. Particles in the subsurface that are disturbed by a P-wave, move in the same direction as the wave propagates. The compressional stress causes a short change of the particle volume in the elastic frame (Yilmaz, 2001). A velocity expression is derived in the following using Newton's and Hook's relation.
Starting point is Newton's third law $F^E = ma^C$ to achieve the conservation of momentum (Snieder, 1994) with F^E as force, m mass and a^C acceleration. The total force acting on an elastic solid can be formulated as $F^E \delta V^E$ where F^E describes the force per unit volume and δV^E a certain volume. Its mass is defined as $\delta m = \rho \delta V^E$ where ρ is density. Newton's third law can now be expressed in our defined parameters as

$$F^E \delta V^E = \frac{d}{dt}(\rho \delta V^E v) = \frac{d}{dt}(\delta m v), \tag{2.9}$$

where v describe the velocity in the media. Formulation of the linearized Newton's law in the Eulerian form gives

$$F^E = \rho \frac{\partial v}{\partial t}. \tag{2.10}$$

The force F^E includes internal and external agents. Here, we only consider internal agents as stresses on a finite volume $\partial \sigma_{ij} / \partial x_i$. We introduce the displacement notation with u as displacement, where $v = \frac{\partial u}{\partial t}$. We may rewrite the right-hand side of equation 2.10 in terms of stresses acting on a finite volume as

$$\rho \frac{\partial^2 u_i}{\partial t^2} = \frac{\partial \sigma_{\mathrm{ij}}}{\partial x_i} = \frac{\partial \sigma_{11}}{\partial x_1} + \frac{\partial \sigma_{21}}{\partial x_2} + \frac{\partial \sigma_{31}}{\partial x_3}. \tag{2.11}$$

σ_{ij} describes the stress components of the stress tensor $\boldsymbol{\sigma}$. The first subscript represents the coordinate axis normal to plane and the second indicates the axis parallel to the traction. Shear stress components σ_{21}, σ_{31} acting on a medium cause shear strains. In geophysics, the medium is often assumed to have an elastic behaviour for the sake of simplicity. Hook's law for elastic isotropic media states

$$\sigma_{ij} = \lambda\delta_{ij}\epsilon_{kk} + 2\mu\epsilon_{ij} = \lambda\delta_{ij}\epsilon_{kk} + 2\mu\frac{1}{2}\left(\frac{\partial u_j}{\partial x_i} + \frac{\partial u_i}{\partial x_j}\right), \tag{2.12}$$

where δ_{ij} represents the Kronecker delta. In case where $i = j$, the delta becomes 1 and elsewise zero. ϵ_{kk} represents the normal strain or dilatation. For $i = j$, equation 2.12 leads to

$$\sigma_{ii} = \lambda\epsilon_{ii} + 2\mu\frac{1}{2}\left[\frac{\partial u_i}{\partial x_i} + \frac{\partial u_i}{\partial x_i}\right] = \lambda\epsilon_{ii} + 2\mu\partial_i u_i. \tag{2.13}$$

To simplify these equations, we reformulate the strain for instance in x_1-direction as $\epsilon_{11} = \frac{\partial u_1}{\partial x_1} = \partial_1 u_1$ using Newton's third law. The complete expression may be written as $\sigma_{11} = E\epsilon_{11} = E\partial_1 u_1$, where E is called Young's modulus (Lowrie, 1997). Applying the last statement for i=1 to equation 2.13, we obtain

$$\sigma_{11} = (\lambda + 2\mu)\partial_1 u_1. \tag{2.14}$$

Similar derivations are carried out for σ_{21} and σ_{31} in equation 2.12. To achieve the Cauchy-Navier equation of motion (Giardini, 2006), we take the partial derivative in x_1, x_2 and x_3 direction for σ_{11}, σ_{21} and σ_{31}, respectively. We conduct this to obtain an expression shown on the right-hand side of equation 2.11. Those expressions are replaced. The final Cauchy-Navier equation can be expressed as

$$\rho\partial_t^2 u_i = (\lambda + \mu)\partial_i\partial_j u_j + \mu\partial_i^2 u_j. \tag{2.15}$$

Different cases can be studied based on this equation. In the following, we will apply this equation for the P- and S-waves.

2.4.2. P-waves

A wave propagating along the x_1-axis leads to $\partial_2 = \partial_3 = 0$ resulting in $u_2 = u_3 = 0$. Equation 2.15 simplifies to

$$\rho\partial_t^2 u_1 = (\lambda + 2\mu)\partial_1^2 u_1. \tag{2.16}$$

A solution for this kind of differential equation can be found. A general solution for P-waves is $u_1 = f(t - x_1/v^P) + g(t + x_1/v^P)$ where f and g are arbitrary functions (Strobbia, 2002). Substitution of f into equation 2.16 leads to the P-wave velocity v^P in isotropic media

$$v^P = \sqrt{\frac{\lambda + 2\mu}{\rho}} = \sqrt{\frac{K + \frac{4}{3}\mu}{\rho}}, \tag{2.17}$$

where λ and μ are Lamé constants and K bulk modulus or incompressibility. The Lamé constant μ represents the shear modulus defined as the ratio of shear stress to shear strain. The second Lamé constant is related to bulk and shear moduls as $\lambda = K - \frac{2}{3}\mu$.

2.4.3. S-waves

Transverse waves, also called shear or S-waves cause a particle motion in the direction perpendicular to the wave propagation. Characteristic for that kind of wave is that the shear stress deforms the particle shape. The fact that transverse waves orginate shear effects on particles in different directions can be used to split up the wave in two components. Horizontal shear (SH-) waves possess a motion parallel to the surface whereas vertical shear (SV-) waves move normal with respect to the surface. A shear velocity expression v^S is obtained again from the Cauchy-Navier equation 2.15, where a wave travels along the x_1 axis but with x_2-displacement. For $\partial_2 = \partial_3$ and $u_1 = u_3 = 0$ we obtain

$$\rho \partial_t^2 u_2 = \mu \partial_1^2 u_2. \tag{2.18}$$

This describes a SH-wave. A similar substitution as done for the P-waves leads to the S-wave solution in isotropic media

$$v^S = \sqrt{\frac{\mu}{\rho}}. \tag{2.19}$$

Note that S-waves cannot propagate in liquids since we have in liquids $\mu = 0$. A shear wave with vertical displacement is derived in the same way as the SH-wave, it only differs in the vertical displacement u_3. We can reformulate equation 2.15 as

$$\rho \partial_t^2 u_3 = \mu \partial_1^2 u_3. \tag{2.20}$$

Both shear wave expressions have the same structure. If we solve equation 2.20, the same expression for the shear wave velocity is obtained as in equation 2.19.

2.5. Medium parameters

2.5.1. Quality factor

Near-surface rocks with often poor rigidity cannot be regarded to behave as nearly elastic materials. Seismic waves lose energy travelling through non-perfect elastic media mainly due to friction loss, which is called attenuation. Attenuation is dependent on the frequency of the signal (Lowrie, 1997). High frequency signals are more attenuated than low frequency ones. Therefore, near-surface rocks act as a low-pass filter. An equation that represents the simplest case of a plane wave in homogeneous medium, can be defined as

$$Q = \frac{\pi f}{\alpha v}, \tag{2.21}$$

where α represents attenuation. For dry rocks, Q is mainly frequency independent over a broad frequency band (10^{-2}-10^{7}Hz), where it is negligible frequency dependent in porous, permeable rocks (Johnston et al., 1979). Having α, v^P and v^S, one can invert for the quality factors. A summarizing article about Q inversion using dispersive Rayleigh

waves and the relation to the v^P/v^S ratio was published by Xia et al. (2002).
In our synthetic seismograms, the Q-factors are kept fixed. Instead of Q^K and Q^μ, the quality factor notation Q^P and Q^S are often used. The superscripts indicate bulk and shear wave modulus and are related as

$$\frac{1}{Q^P} = \frac{1}{Q^\mu} + \left(1 - \frac{4}{3}\left(\frac{v^S}{v^P}\right)^2\right)\left(\frac{1}{Q^K} - \frac{1}{Q^\mu}\right) \tag{2.22}$$

and $Q^S = Q^\mu$ (Forbriger & Friederich, 2005). Q values for different kind of rocks are tabulated in the literature for example by Yilmaz (2001).

2.5.2. Poisson's ratio

The ratio between v^P/v^S is uniquely determined in material by

$$\left(\frac{v^P}{v^S}\right)^2 = \frac{2(1-\nu)}{1-2\nu}, \tag{2.23}$$

where ν is the Poisson's ratio. It is defined as $\nu = -\frac{\epsilon_{22}}{\epsilon_{11}}$ for a solid extended by a force in x_1 direction. Physically meaningful values for rocks are $\nu = 0 - 0.5$, where the lower and upper limit have no lateral contraction and no volume change, respectively (Lowrie, 1997). The upper limit is not reachable because completely incompressible solids do not exist. For v^P/v^S less than 1.42, the Poisson's ratio becomes negative. Rigid plutonic rocks for instance have $\nu = 0.45$. In near-surface investigations, Poisson's values of unconsolidated and slightly consolidated rocks are often of more interest because the earth surface is mainly covered by weathered rocks and sediments, see Table 2.1. Unconsolidated brine-saturated Quartz sand and silty alluvia comprise a Poisson's value of $\nu = 0.4$, which corresponds to $v^P/v^S = 2.37$. This ratio is used for all synthetic models, if not mentioned otherwise.
Having already an outlook to the experimental dataset, Poisson's ratios of alluvial, wet or brine-saturated, unconsolidated rocks are of interest. Brine usually means saltwater, but the corresponding ratio can also be taken for freshwater since its physical behaviour differs not drastically. Another important fact has to be pointed out. Soils, which underlie permafrost due to low temperatures, include ice with $\nu = 0.33$ instead of water. This case should be considered in surveys in cold areas because the shallow subsurface can be frozen there. We have seen that unconsolidated sediments can have variable Poisson's ratios. They are not only affected by the rock composition but also by compaction, cementation, saturation and condition of the saturating fluid (e.g. ice). Later, the v^P/v^S ratio is adjusted by including refraction information.

Table 2.1: Poisson ratios of various rocks

Rock type	ν [-]	Description	Source
General	0.05	poorly consolidated	*a)*
Quartz-sand	0.1-0.15	gas-saturated, unconsolidated	*b)*
Sand	0.14-0.15	dry, unconsolidated, granular	*c)*
General	0.25	consolidated	*d)*
Ice	0.33	consolidated	
Quartz-sand	0.4-0.5	brine-saturated, unconsolidated	*b)*
Silty alluvia	0.4-0.45	unconsolidated	*e)*
Granite	0.45	consolidated, rigid	*a)*
Alluvial	0.46	unsaturated, unconsolidated	*f)*
Silt/sand	0.47	unconsolidated	*g)*
Gravel/sand	0.47	wet, unconsolidated	*g)*

---

[a] Lowrie (1997)
[b] Domenico (1977)
[c] Manificat and Guéguen (1998)
[d] Kearey et al. (2002)
[e] Ivanov et al. (2000b)
[f] Roth et al. (1998)
[g] Robertsson, Holliger, Green, Pugin, and Iaco (1996); Lanz et al. (1996)

2.5.3. Density estimation

P- and S-wave velocities can be used to estimate material densities. We applied the empirical density relation defined by Gardner et al. (1974)

$$\rho = 1.74 \left(v^P\right)^{0.25} . \tag{2.24}$$

This relation is valid between 1.5km/s < v^P <6.1 km/s, where it is originally derived for sedimentary rocks and mainly incorporates changes in porosity (Brocher, 2005; Barnola & White, 2001). Evaluation of first arrivals and calculation of densities showed in all synthetic models that P-wave velocities below 1.5km/s lead to slightly erroneous density estimations. A density relation considering v^S velocity is given by Dal Moro et al. (2007)

$$\rho = 0.77 log_{10} \left(v^S\right) + 0.15. \tag{2.25}$$

Since densities have only small influence on the surface wave inversion result, a rough density guess (e.g. eq. 2.25) is sufficient for the inversion.

2.6. Refraction and reflection seismic

Refraction seismic is the oldest seismic method and mainly applied to determine the depth to the bedrock. Usual assumption is that the underlying layer exhibits a higher velocity than the overlying layer. In almost any record, the direct body wave at small offsets and refracted waves at greater offset can be identified. They form the first observable seismic events in a seismogram and are known as first arrivals. Refraction seismic analyzes these first arrivals. As the name says, a refracted wave is a wave that is critically refracted at layer boundaries and emits head waves back to the surface. An overview of the important seismic wave paths is given in Figure 2.1.

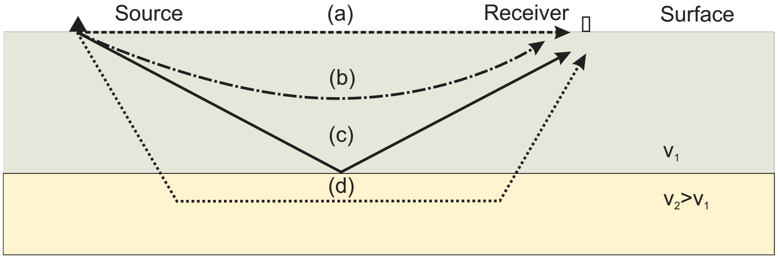

Figure 2.1: Possible raypath of a (a) direct wave, (b) dispersive wave, (c) reflected and (d) refracted wave

We derive in the following a multilayer formula for refracted waves to finally obtain velocity and thickness of each identifyable layer. The simplest case to study is to consider horizontally layered, laterally homogeneous and isotropic media. We imagine a wave as a ray traveling along a layer interface. A ray is defined as a normal vector on a wavefront pointing in the direction of propagation. Snell's law for the critical angle can be written as

$$\frac{\sin\Theta^C}{v_1} = \frac{1}{v_2}, \tag{2.26}$$

where Θ^C indicates the critical angle. Under this angle, an incident wave is refracted and travels along the interface in the underlying layer with v_2. In Figure 2.2, a refracted ray is schematically illustrated. An expression for the first and third part can be obtained by using Pythagoras. We read

$$t^T_{1,3} = \frac{\Delta x^{1,3}_\alpha \sin\Theta^C}{v_1} + \frac{d_1\cos\Theta^C}{v_1}, \tag{2.27}$$

where the subscripts 1, 3 stand for the critical incident and back radiated head wave, respectively. t^T is travel time and d layer thickness. Over length Δx^2_α and travel time t_2 in part two, the ray is travelling with v_2. All separated terms are brought together to write the entire raypath and travel time t^T. A compact formula is read as

$$t^T = \frac{x_\alpha}{v_2} + \frac{2d_1\cos\Theta^C}{v_1}, \tag{2.28}$$

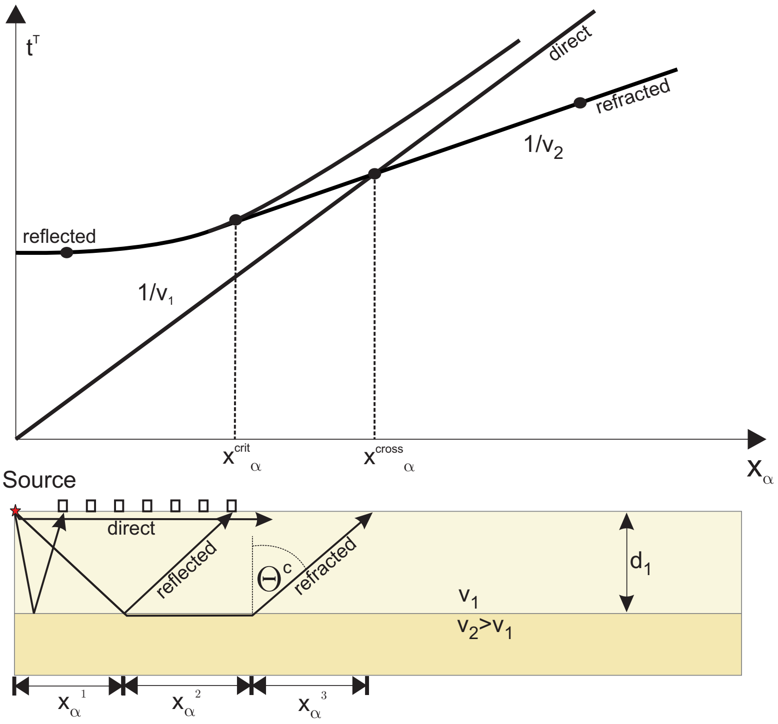

Figure 2.2: Raypaths of direct, refracted and reflected waves are displayed and a corresponding travel time curve on top.

where $x_\alpha = \Delta x_\alpha^1 + \Delta x_\alpha^2 + \Delta x_\alpha^3$, $t^T = t_1^T + t_2^T + t_3^T$ and the relation 2.26 is used. We can also rewrite $\cos\Theta^C = \sqrt{v_2^2 - v_1^2}/v_2$ hence, no angle is encountered anymore. Starting from the obtained equation, we can simply expand the presented two layer equation to a n-layer equation. For each additional layer, only down- and upgoing raypath parts have to be added similar to equation 2.28. In a two-layer model, these parts are indicated with $x_\alpha^{1,3}$. The travel time of a ray in a n-layered media is then written as

$$t_n^T = \frac{x_\alpha}{v_n} + \sum_{i=1}^{n-1} \frac{2d_i\sqrt{v_n^2 - v_i^2}}{v_n v_i}. \tag{2.29}$$

i is a running variable and indicates a specified layer excluding the homogeneous halfspace. The number of layers including the halfspace is described with n. Second term on the right-hand side of equation 2.29 represents the intercept time $t_{n,int}$. If more than one layer is present, different grades and corresponding travel-time intercepts on the time axis can be read. The inverse declination of the gradient directly gives the velocity of the respective layer. Rewriting equation 2.29, we obtain for example the thickness of the first layer

$$d_1 = \frac{t_{1,int}^T}{2} \frac{v_2 v_1}{\sqrt{v_2^2 - v_1^2}}. \tag{2.30}$$

If heights and velocities were calculated, they can be used as model parameter estimate (initial guess) for the inversion process.
In nature, we often deal with undulating layers. To avoid erroneous travel time curves, shots in opposite directions are made. The travel time versus distance figure, in which the opposite shot is included, comprises in case of dipping layers two asymmetric refracted curves. In cases where $v_2 < v_1$ or the layer thickness is too thin (Kirsch & Rabbel, 1997), the corresponding refracted waves cannot be recorded at the surface. In latter case, we are speaking of 'over-shooting' a layer. A comprehensive overview for further reading is given by Lowrie (1997); Kirsch and Rabbel (1997). First breaks can also be analyzed by employing a tomographic scheme (Lanz et al., 1998). Travel times of first arrivals and corresponding raypaths are computed to obtain a subsurface model.

In contrast to first breaks, where we are only interested in travel times by means of velocity contrasts, reflection seismic integrates the entire sequence of wave trains and their amplitudes. Depending on the acoustic impedance in the subsurface, different amplitudes are obtained. This method has many applications since it can deliver 2- and 3-dimensional images of the subsurface.

2.7. Surface wave method

Dispersion phenomena are examined within the surface wave method to achieve information about the subsurface. From now on, we abbreviate surface wave method with SWM. Unlike in refraction and reflection seismics, surface waves are extracted from a seismic record as useful information.
In context of dispersion analysis, two velocities are commonly used: group and phase velocity. The difference between these two terms can be explained by taking two waves, which interfere with each other. A periodic wave function propagating in positive x_1-direction may read as

$$a(x_1, t) = a_0 \cos(\omega t - k_1 x_1), \tag{2.31}$$

where a is the amplitude of the wave with starting value a_0. If we superimpose now two waves with slightly different angular frequencies and wavenumbers, equation 2.31 can be reformulated as

$$a(x_1, t) = \cos[(\omega - \Delta\omega)t - (k_1 - \Delta k_1)x_1] + \cos[(\omega + \Delta\omega)t - (k_1 + \Delta k_1)x_1], \tag{2.32}$$

where $\Delta\omega$ and Δk_1 indicate the differences between the waves and a_0 is set to 1. On both terms on the right-hand side, the following trigonometric identity (Abramowitz & Stegun, 1965) is applied

$$\begin{aligned}\cos[(\omega t - k_1 x_1) \pm (\Delta\omega t - \Delta k_1 x_1)] = {} & \cos(\omega t - k_1 x_1)\cos(\Delta\omega t - \Delta k_1 x_1) \\ & \mp \sin(\omega t - k_1 x_1)\sin(\Delta\omega t - \Delta k_1 x_1),\end{aligned} \tag{2.33}$$

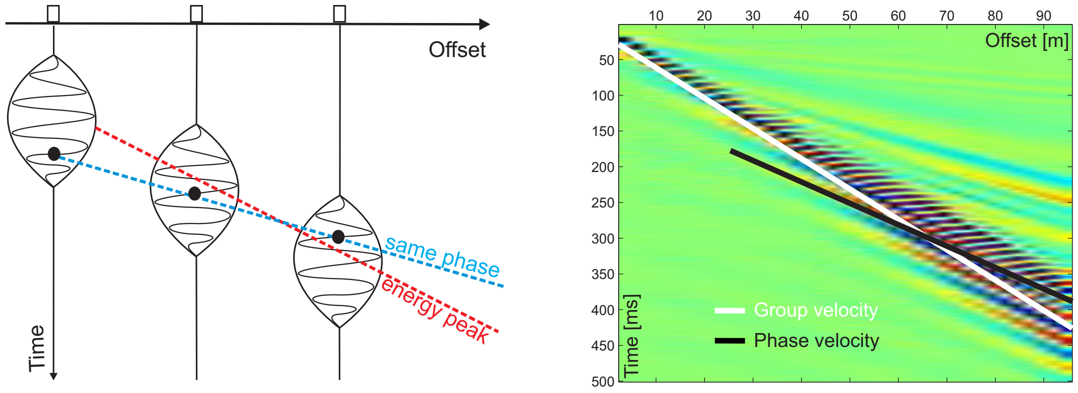
(a) (b)

Figure 2.3: We see in (a) two interfering waves with different frequencies propagating in positive offset direction. The energy peak travels with the group and phase with the phase velocity. Within the shingling events of the surface waves in (b), we also identify group and phase velocity.

to finally obtain

$$a(x_1, t) = 2\cos(wt - k_1 x_1)\cos(\Delta\omega t - \Delta k_1 x_1). \tag{2.34}$$

The resulting wave equation contains two cosine functions with different arguments. These two interfering waves are illustrated as wave package propagating in positive direction in Figure 2.3a. An inner and outer oscillation can be identified. The propagation velocity of the enveloping wave or outer oscillation is identical to the group velocity v^G equal to

$$v^G = \frac{\partial\omega}{\partial k} = \frac{\partial}{\partial k}(ck) = c + k\frac{\partial c}{\partial k} = c - \lambda^L \frac{\partial c}{\partial \lambda^L}. \tag{2.35}$$

The velocity of the inner oscillation, see Figure 2.3a, corresponds to the phase velocity c. The frequency dependence of $c(\omega)$ is also called *dispersion*. The energy travels with the speed of the group velocity under normal dispersion conditions. Normal dispersion is present, if longer wavelengths λ^L propagate faster than short ones and $c > v^G$. Under the special case where $c < v^G$, the energy propagation differs from the group velocity.

Dispersion is indicated in the shingling character of surface waves on a record - see Figure 2.3b. Similar as shown in Figure 2.3a, phase and group velocity can be distinguished. The overall wave energy travels slower than the phase of the wave. As already mentioned in the introduction, SWM deals with geometric dispersion. The obtained curve in a frequency versus phase velocity plot is then defined as dispersion curve. Waves in vertically heterogeneous media with larger wavelengths and corresponding lower frequencies can penetrate deeper into the media than shorter wavelengths with higher frequencies. The low frequency spectrum is therefore more influenced by deeper layers shown in Figure 2.4. In addition, several phase velocities with different wavelength at one specific fre-

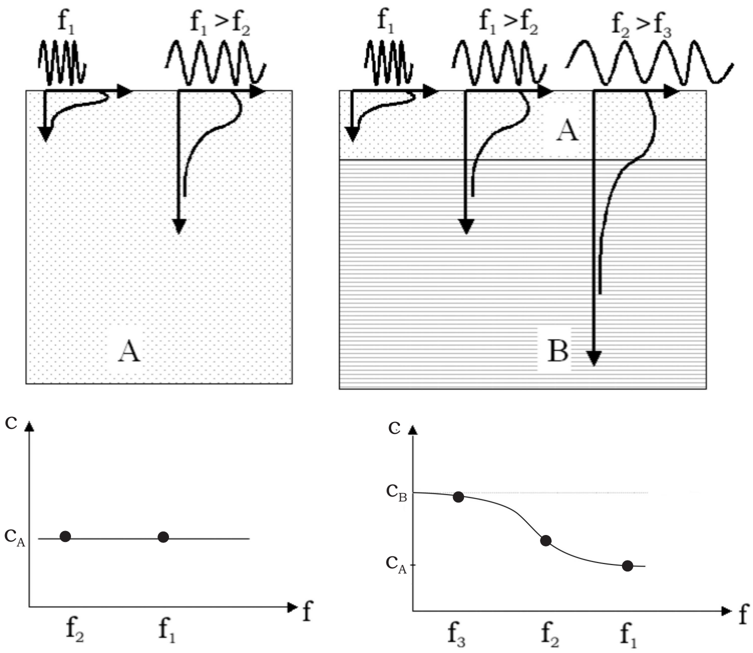

Figure 2.4: Homogeneous media show no dispersion where in heterogeneous media, geometric dispersion and the resulting phase velocity change with frequency occur.

quency can occur (Strobbia, 2002). Those higher order phase velocities are called modes and are also known as overtones. Higher order modes only exist above a certain cut-off frequency. Their presence is dependent on the energy and depth of the source as well as of the geological stratigraphy.

3. Surface waves

A special set of waves, which can be summarized as surface waves, are created at the medium boundaries. In marine environment along the sea bottom or in fluid filled boreholes, different kinds of surface waves are generated during a seismic survey compared to land environment. Scholte or Stoneley waves propagate along interfaces of solid and fluid media. Exploration companies investigate them to extract information about the rock properties. Another surface wave, the Lamb wave, can appear in bounded plate surfaces. It is a kind of longitudinal wave and is caused by the wave-guide effect.
Focus of this work is on surface waves recorded in land seismics. An interesting aspect of surface waves is their high energy. If we consider the geometric attenuation, energy-decrease can be explained with the spreading of a wavefront. Surface waves spread cylindrically at the surface so that their energy decreases with a factor $(r^D)^{-1}$ with r^D equals the radial distance away from the source. Body waves contrarily propagate spherically and lose therefore energy proportional to $(r^D)^{-2}$. The energy, which is proportional to amplitude squared, is represented in the amplitudes in a seismogram. In case of surface waves, which have a smaller energy-decrease than P-waves, we can observe their high amplitudes over long distances. Therefore, they dominate seismic records at great offsets.
Wood (1968) observed that the main part of the source energy goes into surface waves. For a vertically oscillating circular source for example, 67% of the source energy is converted into Rayleigh wave energy and only 26% into S-wave energy. The remaining percentage is transformed into P-wave energy.

3.1. Love waves

Love waves are guided and dispersive and used in land seismic surveys. In layered media, where the S-wave velocity of the underlying layer is different, Love waves can propagate

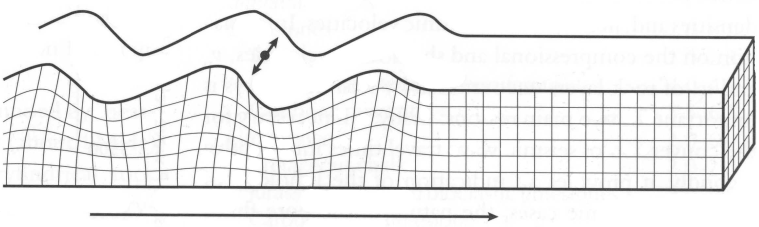

Figure 3.1: Particle motion of a propagating Love wave

- see Figure 3.1 after Bolt (1982). A Love wave is a polarized S-wave generated by multiple, total reflection of horizontal S-waves. That is why they cannot occur in homogeneous media. If one receives Love waves, the subsurface has to be layered in the reachable depth range of our sources.

An expression for Love waves is derived in the following (Butler, 2005; Wapenaar & Berkhout, 1989) based on plane waves. Describing the problem with plane waves is justified, because spherical waves can be theoretically decomposed into a sum of plane waves. We consider harmonic plane waves, which propagate through a verticall heterogeneous linear elastic media on top of an isotropic halfspace. Homogenous (propagating) and inhomogeneous (evanescent) plane waves can be consecutively written as

$$p^{\pm} = p_0^{\pm} \cos\left[\omega_0(t - s_1x_1 - s_2x_2 - s_3x_3) + \Theta_0\right] \tag{3.1}$$

$$p^{\pm} = p_0^{\pm} \cos\left[\omega_0(t - s_1x_1 - s_2x_2) + \Theta_0\right] e^{\mp\omega_0\sigma_3x_3}, \tag{3.2}$$

where p describes the acoustic wave field and p_0 the amplitude factor. The variable σ_3 is defined as $\sigma_3 = \pm\sqrt{s_1^2 + s_2^2 - \frac{1}{c^2}}$, c indicates the phase velocity and ± indicates down- and upgoing waves, respectively. s_i stands for slowness, the reciprocal of velocity, and Θ_0 describes the phase difference. The second term in equation 3.2 is referred to as evanescent term. We reformulate the plane wave equations in complex notation for downgoing waves for the sake of simplicity using

$$e^{a+ib} = e^a[\cos b + i \sin b]. \tag{3.3}$$

Homogeneous plane waves can be partly decomposed in an expression $\cos(b) = Re(e^{ib})$ and evanescent waves into $\cos(b)e^a = Re(e^{ib})e^a$. We read the homogeneous plane wave

$$p^+ = \hat{p}_0 Re[e^{i(\omega_0(t - s_1x_1 - s_2x_2 - s_3x_3) + \Theta_0)}], \tag{3.4}$$

and inhomogeneous plane wave

$$p^+ = \hat{p}_0 Re[e^{i(\omega_0(t - s_1x_1 - s_2x_2) + \Theta_0)}] e^{-i\sigma_3\omega_0x_3}. \tag{3.5}$$

Two-way wave equations can, of course, also be transformed into one-way wave equations. In our vertically heterogeneous model only depth variations (x_3-coordinate) are allowed for example density $\rho(x_3)$. We find

$$\frac{\partial p^{\pm}}{\partial x_3} = \mp\omega_0 s_3 \hat{p}^{\pm}. \tag{3.6}$$

The solution of this differential equation is given by

$$\hat{p}^{\pm} = \hat{w}^{\pm}(x_3)\hat{p}^{\pm}(x_1, x_2, x_3, t) \tag{3.7}$$

with $\hat{p}^{\pm}(x_1, x_2, x_3, t) = \hat{p}_0^{\pm} e^{i\omega_0(t - s_1x_1 - s_2x_2 \mp s_3x_3)}$ and $\hat{w}^{\pm}(x_3) = e^{i\omega_0 s_3 x_3}$ represents the one-way extrapolation operator (Wapenaar & Berkhout, 1989). At the surface boundary $x_3 = 0$, equation 3.7 can be simplified. For propagating waves, the case we are looking at with Love waves, $\hat{w}^{\pm}(x_3)$ is equals one. The inhomogeneous plane waves are neglected here. However, they are used to describe the Rayleigh waves, because their wave movement is elliptical. A combination of inhomogeneous P- and S-waves leads to the Rayleigh wave equation.

Love as well as Rayleigh wave equations are often expressed in displacement notation for the sake of convenience. Plane wave equation 3.4 can be reformulated as plane displacement wave $u_i(u_1, u_2, u_3)$ for three coordinates of displacement x_i. In particular, the displacement components of the amplitude factor $z_i(z_1, z_2, z_3)$ can be written as $z_1(x_1, x_3, t)$, $z_2(x_1, x_3, t)$ and $z_3(x_1, x_3, t)$ by considering the $x_1 - x_3$ plane. The amplitude factor is Fourier transformed into $k - \omega$ domain. We write the plane wave equation as

$$u_i(x_1, x_2, x_3, t) = z_i(k_j, \omega, x_3) Re[e^{i(\omega t - \omega s_1 x_1 - \omega s_2 x_2 - \omega s_3 x_3)}], \tag{3.8}$$

where k_j comprise the vector

$$\boldsymbol{k} = \begin{pmatrix} k_1 = \omega s_1 \\ k_2 = \omega s_2 \\ k_3 = \omega s_3 \end{pmatrix}. \tag{3.9}$$

We neglect the x_2-coordinate in our case. Depth and propagation direction x_1 are taken into account and we find

$$u_j(x_1, x_3, t) = z_i(k_j, \omega, x_3) Re[e^{i(\omega t - k_j x_i)}]. \tag{3.10}$$

The Love waves only involve $u_2(x_1, x_3, t)$ whereas Rayleigh waves comprise components $u_1(x_1, x_3, t)$ and $u_3(x_1, x_3, t)$. In dispersive media, the wavenumber in equation 3.10 is a function of frequency and has to be replaced with $k_j^n(\omega)$ where n indicates modes. Substituting the wavenumber into equation 3.10 leads to

$$u_i(x_1, x_3, t) = z_i(k_j^n(\omega), \omega, x_3) Re\left[e^{i[k_j^n(\omega)\left(\frac{\omega}{k_j^n(\omega)} t - x_i\right)]} \right], \tag{3.11}$$

where the phase velocity can be recognized in the exponent.

3.1.1. Homogeneous layer over halfspace

We examine in this section Love waves in the simplest case of a homogeneous layer over a halfspace and follow the derivation of Aki and Richards (2002) to obtain the Love wave dispersion equation. Let start us with the plane wave definition in the $x_1 - x_3$ plane as used before. We read

$$u_i(x_1, x_3, t) = z_i(x_3) e^{i(wt - k_i x_j)}, \tag{3.12}$$

where $z_i(x_3)$ represents a weigthing or amplitude factor acting in depth direction. The exponential term is a solution term of the differential wave equation. Separation of

Figure 3.2: Layer and parameter annotation: ρ density and μ shear modulus. The simplest medium in which Love waves (supercritically reflected SH-waves) can be generated.

variables is applied to solve this equation.
Consider our two layer model where $\mu_{1,2}$, $\rho_{1,2}$ are the shear modulus and density for the first layer and halfspace, respectively - see Figure 3.2. We assume again that the underlying layers have higher velocities than the overlying layers. The wave equation is given for both layers

$$\partial_t^2 u_2 = \frac{\mu_{1,2}}{\rho_{1,2}} \left(\partial_1^2 u_2 + \partial_3^2 u_2\right). \tag{3.13}$$

Note that only the u_2 displacement in x_2 direction is included for Love waves. A solution for equation 3.13 has to be found. Hence, equation 3.12 is employed as

$$u_2 = [d_1^G e^{-u_{2,1}x_3} + u_1^G e^{u_{2,1}x_3}]e^{i(wt-kx_1)} \tag{3.14}$$

$$u_2 = [d_2^G e^{-u_{2,2}^2 x_3} + u_2^G e^{u_{2,2}^2 x_3}]e^{i(wt-kx_1)}, \tag{3.15}$$

where the first terms between the brackets on the right side represent z_i. Equations 3.14 and 3.15 include downgoing and upgoing waves indicated by the variables d^G and u^G. We further state that $u_{2,\alpha} = \sqrt{k^2 - \frac{\omega^2}{(v_\alpha^S)^2}}$, where $Re(u_{2,\alpha} \geq 0)$ and α=1 stands for the first layer and α=2 for the halfspace. As stated before, displacement u_2 is real and positive implying that d^G and u^G must be constants. Furthermore, for real ω, k and v^S, the displacements $u_{2,\alpha}$ are real and positive, if the root is taken to give $iu_{2,\alpha}$. Equation 3.14 describes the displacement u_2 in the top layer whereas equation 3.15 explains the displacement in the halfspace. We define the interface depth between the two media as d.
Here, boundary conditions are involved. The wave equation has to fulfill three conditions: the equation of motion must be valid and the boundary conditions at the surface and infinity have to be considered. Latter boundary condition implies that there is no upcoming wave, so u_2^G becomes zero. Boundary condition two states that there is no traction at the surface according to $\frac{\partial u_2}{\partial x_3} = 0$. Using this condition in equation 3.14, we see that $d_1^G = u_1^G$. Third condition says that continuity of displacement and traction over an interface must hold. We principally compare $z_i(x_3)$ in equation 3.14 and

3.15 and keep the results we achieved before in mind. Imagine an interface at depth d and remember that there are only two unknowns d_1^G and d_2^G left. We remain with the expressions

$$2d_1^G \cos\left(iu_{2,1}d\right) = d_2^G e^{-u_{2,2}d}, \tag{3.16}$$

$$2i\mu_1 u_{2,1} d_1^G \sin\left(iu_{2,1}d\right) = \mu_2 u_{2,2} d_2^G e^{-u_{2,2}d}. \tag{3.17}$$

These equations can be rearranged to obtain

$$\frac{d_2^G}{d_1^G} = \frac{2\cos\left(iu_{2,1}d\right)}{e^{-u_{2,2}d}} = \frac{2i\mu_1 u_{2,1}\sin\left(iu_{2,1}d\right)}{\mu_2 u_{2,2} e^{-u_{2,2}d}}, \tag{3.18}$$

and finally

$$\tilde{F}(k) = \tan\left(iu_{2,1}d\right) - \frac{\mu_2 u_{2,2}}{i\mu_1 u_{2,1}}, \tag{3.19}$$

where $\tilde{F}(k) = 0$ is a solution of this equation with the so-called wavenumber eigenvalues k^n. The superscript n is the mode number. The tangent in equation 3.19 is obtained by applying $\tan\left(iu_{2,1}d\right) = \frac{\cos iu_{2,1}d}{\sin iu_{2,1}d}$ on (3.18). The wavenumber is linked to the phase velocity and therefore also to phase velocity eigenvalues over $c^n = \frac{\omega}{k^n}$. We shall put $u_{2,\alpha}$ into equation 3.19 for the solution $\tilde{F}(k) = 0$ that we get

$$\tan\left(\omega d\sqrt{(v_1^S)^{-2} - c^{-2}}\right) = \frac{\mu_2}{\mu_1}\frac{\sqrt{c^{-2} - (v_2^S)^{-2}}}{\sqrt{(v_1^S)-2 - c^{-2}}}. \tag{3.20}$$

The final solution of the Love wave displacement is obtained by setting equation 3.18 into the initially stated solutions (3.14) and (3.15). To explicitely highlight the frequency dependence of phase velocity and wavenumber, we replace them by $c(\omega)$ and $k(\omega)$. We obtain

$$u_2^n(x_1, x_3, t) = 2d_1^G \cos\left(\omega\sqrt{(v_1^S)^{-2} - (c^n(\omega))^{-2}}x_3\right) e^{i(\omega t - k^n(\omega)x_1)} \tag{3.21}$$

for the top layer $0 \leq x_3 \leq d$ and

$$u_2^n(x_1, x_3, t) = 2d_1^G \cos\left(\omega\sqrt{(v_1^S)-2 - (c^n(\omega))^{-2}}d\right) e^{-\omega\sqrt{(c^n(\omega))^{-2} - (v_2^S)^{-2}}(x_3 - d)} e^{i(\omega t - k^n(\omega)x_1)} \tag{3.22}$$

for the homogeneous halfspace. Surface waves occur in a vertically heterogeneous medium in different modes as we have seen for Love waves in the derivation. However, higher order modes will not appear before a certain cut-off frequency is reached. How these cut-off values are obtained, is shown in the following. The same model and assumptions are considered as before. We remember first the argument of the tangent in equation 3.20. The argument part $d\sqrt{(v_1^S)^{-2} - c^{-2}(\omega)}$ is plotted in Figure 3.3a from v_1^S to v_2^S. The left-hand side of (3.20) gives the typical tangent curves whereas the right-hand side curve crosses the tangent lines. Each intersection point represents a root of equation

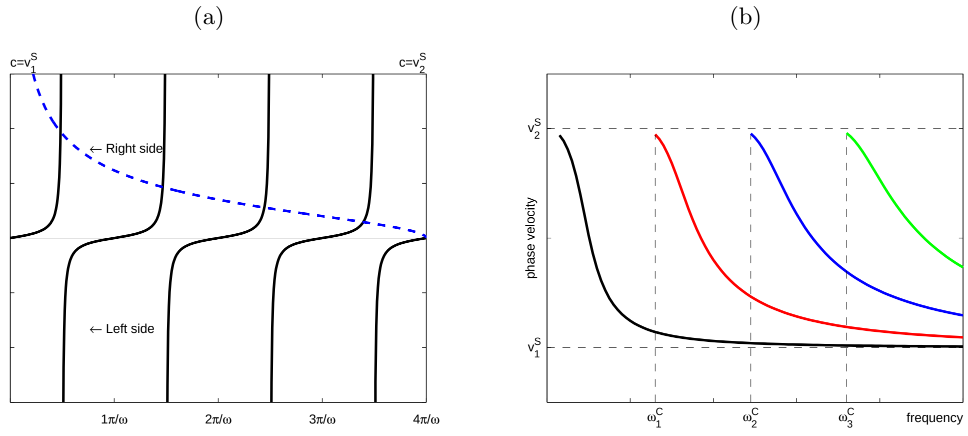

Figure 3.3: Equation 3.20 is illustrated in (a). Each new tangent indicates a higher order mode. Intersection points are the roots of this equation. The phase velocity spectrum in (b) is calculated for the following model: $v_1^S = 200\text{ms}^{-1}$, $v_2^S = 400\text{ms}^{-1}$, $d_1 = 5\text{m}$, $\rho_1 = 1.9\text{gcm}^{-3}$ and $\rho_2 = 2\text{gcm}^{-3}$.

3.20 . Beside that, each entering of a tangent curve with angular frequency ω indicates a cut-off frequency for a new higher mode. We find that a new mode can appear, if π/ω is equal to the plotted argument. In Figure 3.3b, a phase velocity spectrum is calculated with four higher order modes that results from the discussed two layer model. It is obvious that only a limited number of modes can exist in case of two layers and for a certain angular frequency. In the forward model calculations for the dispersion curve, height and v^S are free parameters whereas ρ is obtained using equation 2.25.

3.2. Rayleigh waves

Rayleigh waves are formed by interference of P-SV waves at the free surface. The interference produce a coupled particle motion in the medium shown in Figure 3.4. If we consider such a wave travelling from left to right on a macroscopic scale, we see that the wave has a retrograde elliptical movement. At the wavefront, the particle displacement is vertical due to the vertical shear component. Lord Rayleigh described first this kind of waves in 1885 and therefore they bear his name. Low propagation velocity, low frequency and high amplitudes are characteristic for this kind of wave. In contrast to Love waves, Rayleigh waves can occur in a semi-infinite halfspace as well as in layered media (Lowrie, 1997). In a homogeneous solid halfspace, however, no dispersion is observed. In layered media, Rayleigh waves become dispersive if their wavelength is 1-30 times the layer thickness (Stokoe et al., 1994). Rayleigh waves are slower than S-waves; in a homogeneous halfspace their velocity approaches $0.9194v^S$ when assuming a Poisson's ratio of 0.25.

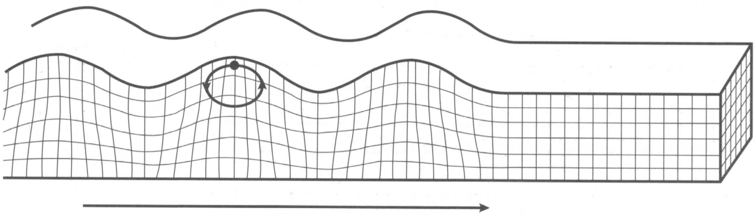

Figure 3.4: Particle motion of a propagating Rayleigh wave

We know that Rayleigh waves travel along the surface and do not lose much energy over a large offset range. In fact, they do not deeply penetrate into the subsurface. In a homogeneous halfspace, the amplitude of the wave decreases exponentially. The penetration depth of Rayleigh waves is typically defined as the depth, where the surface-amplitude fall to the value of e^{-1} (Lowrie, 1997). Roughly spoken, the penetration depth of Rayleigh waves is about $0.4\lambda^L$.
In Appendix A, the Rayleigh wave dispersion equation is derived, which depends on v^P, v^S, ρ, and thickness of the layer. In the forward modeling, v^P is obtained using equation 2.23 and ρ is estimated using equations 2.24 and 2.25.

4. Phase velocity spectra calculation

We make use of the dispersion phenomena. It is therefore essential to properly calculate dispersion curves. Different methods were proposed in the past to obtain and distinguish curves of different modes. We discuss them in the following.
We start with the three-step wavefield transformation method (TST) by Park et al. (1998), which was widely applied in recent years. Fourier, integral and phase transforms are conducted. This method is used throughout this work, if not mentioned otherwise. Pre-processing of synthetic or field data comprises the generation of single shot gathers. Hence, we can transform the wave field $w^F(x_\alpha, t)$ into the frequency domain (van der Kruk et al., 2006):

$$W^F(x_\alpha, f) = \int w^F(x_\alpha, t) e^{-i2\pi f t} dt. \tag{4.1}$$

For each frequency of $W^F(x_\alpha, f)$, an amplitude $|W^F(x_\alpha, f)|$ exists that has a certain phase velocity c. The phase of the wave amplitude appears later in records with increasing offset. Therefore, it is corrected with an offset dependent phase-shift $\Delta\theta$

$$\Delta\theta = -\frac{2\pi f}{c(f)} \Delta x_\alpha. \tag{4.2}$$

Furthermore, attenuation and spherical divergence reduces the amplitude with increasing offset. We compensate for that by normalizing the wave field. The phase velocity spectrum $P^S(c, f)$ is now obtained by applying the inverse of the offset dependent phase change to the normalized wave field. Summation over the entire offset range leads to

$$P^S(c, f) = \sum_{x_\alpha} \frac{W^F(x_{\alpha,f})}{|W^F(x_{\alpha,f})|} e^{i2\pi f x_\alpha / c}. \tag{4.3}$$

If more than one maximum amplitude $|W^F(x_{\alpha,f})|$ exists at one frequency, higher order modes are present.

Another way to extract dispersion curves is the slowness-frequency (s-ω) method proposed by McMechan and Yedlin (1981). The processing includes two transformations of the entire wave field. Similar to the previous method, starting point is the decomposition of the wave field spectrum

$$w^F(x_\alpha, t) = \int\int e^{i(\omega t - k_\alpha x_\alpha)} \frac{\tilde{S}(k_\alpha, \omega)}{\tilde{D}(k_\alpha, \omega)} d\omega dk_\alpha. \tag{4.4}$$

The two split terms, $\tilde{S}(k_\alpha, \omega)$ and $\tilde{D}(k_\alpha, \omega)$, are related to source excitation and dispersion, respectively. The wave field in the entire offset is corrected for the offset dependent phase-shift, or phase distortion, and is summed up as

$$w^{Fs}(s_\alpha, \tau) = \int w^F(x_\alpha, (\tau + s_\alpha x_\alpha))dx_\alpha = \int\int\int e^{i[\omega(\tau+s_\alpha x_\alpha)-k_\alpha x_\alpha]}\frac{\tilde{S}(k_\alpha,\omega)}{\tilde{D}(k_\alpha,\omega)}d\omega dk_\alpha dx_\alpha. \tag{4.5}$$

w^{Fs} indicates the wave field after a slant stack. Integration over the offset x_α leads first to a delta-function $\delta(k_\alpha - \omega s_\alpha)$, such that the integration over k_α results in the integrand taken at $k_\alpha = \omega s_\alpha$. The last integral over the angular frequency leads to the desired expression

$$W^{Fs}(s_\alpha, \omega) = \frac{\tilde{S}(\omega s_\alpha, \omega)}{\tilde{D}(\omega s_\alpha, \omega)}. \tag{4.6}$$

At points, where the term related to dispersion is $\tilde{D}(\omega s_\alpha, \omega) = 0$, we get a maximum for $W^{Fs}(s_\alpha, \omega)$. By plotting these maxima in the $s_\alpha - \omega$ plane, dispersion curves are directly obtained. An advantage of the two presented wave field transformation methods is that they include the whole data set and no assumptions have to be made for the kind of waves we are considering.
In contrast to the two methods discussed above, there are methods, where the data is fk- Fourier transformed. Different lines in the resulting fk-spectrum belong to different modes of the surface waves (Gabriels et al., 1987). Dispersion curves are then obtained using the simple relation $c = 2\pi f/k$. Unfortunately, the overall resolution for short offsets is relatively low compared to the two methods discussed above.

A more sophisticated high-resolution fk-spectrum method belongs to the parametric methods and is referred to as fk-MUSIC method for Multiple Signal Classification (Iranpour, Muyzert, & Grion, 2002). The method is based on the correlation matrix $\mathbf{R}$ between receivers. Similar to the wave field transformation methods, $\mathbf{R}$ is then phase-shift corrected. A steering vector $\mathbf{e}^S$ is defined in the form

$$\mathbf{e}^S = \begin{bmatrix} e^{(-ik_\alpha x_{1,0})} \\ \dots \\ e^{(-ik_\alpha x_{\alpha,N^R-1})} \end{bmatrix}, \tag{4.7}$$

where N^R represents the number of receivers. The vector sweeps through possible k_α and seeks for the signal. To minimize the energy (power) output and keep the signal energy constant, a weighting vector $\mathbf{w}$ is used. In other words, sweeping for k_α and minimizing the energy output is an optimization problem. The solution can be written in terms of

$$P^W(x_\alpha) = [\mathbf{e}^{S'}(x_\alpha)\mathbf{R}^{-1}\mathbf{e}^S(x_\alpha)]^{-1}, \tag{4.8}$$

where x_α is the propagation direction in that we are looking for the power spectrum P^W and $'$ is the Hermitian transpose. If the correlation matrix has eigenvalues λ^E and eigenvectors $\mathbf{v}^E$, we can write $\mathbf{e}^{S'}\mathbf{R}\mathbf{e}^S = \sum_{n=1..N^R} \lambda^E|\mathbf{e}^{S'}\mathbf{v}^E_n|^2$. A threshold is applied to separate signal eigenvalues of small noise eigenvalues. The number of significant eigenvalues (signals) is given by N^S. Combining all terms we can reformulate equation 4.8 after Iranpour et al. (2002) and obtain

$$P^W(x_\alpha) = \left[\sum_{n=1..N^S} (\lambda_n^E)^{-1} |\mathbf{e}^{S'}(x_\alpha)\mathbf{v}_n^E|^2 + \sum_{m=N^S+1..N^R} (\lambda_m^E)^{-1} |\mathbf{e}^{S'}(x_\alpha)\mathbf{v}_m^E|^2 \right]^{-1} , \quad (4.9)$$

where first and second term belong to signal and noise subspace, respectively, which are orthogonal to each other. Since the energy output does not include the signal output, the signal subspace is set to zero. Finally, the noise is whitened (Yilmaz, 2001) and the eigenvalues of the noise subspace are replaced by one. We gain a power spectrum expression

$$P^{W,MUSIC}(x_\alpha) = \left[\sum_{m=N^S+1..N^R} |(\mathbf{e}^{S'}(x_\alpha)\mathbf{v}_m^E)|^2 \right]^{-1} . \quad (4.10)$$

Using the relation $c(\omega) = \omega/k_\alpha$, we finally obtain the phase velocity spectrum. If the fk-MUSIC method is applied to synthetic or real data, a high resolution with a few channels can be achieved (Winsborrow et al., 2003). In surveys, often a limited number of channels can be used due to the predicted lateral heterogeneity. Or, the interest is to use a few traces to study lateral heterogeneity. Short arrays average then velocities over shorter distances because we can only obtain a 1D model from our surface waves analysis.

Four different methods were presented to obtain dispersion curves. Transformation of data to determine dispersion curves with high resolution is crucial. The entire inversion process is influenced by that. $s\omega$ and fk methods require in comparison to the three-step transformation and fk-MUSIC method an exceptional large source-receiver offset and a high number of collected traces. A resolution comparison is done by Park et al. (1998) between three-step and $s\omega$ method. He showed that the three-step method attains a higher resolution.

4.1. Resolving power of transformation methods

A comparison between fk-MUSIC and three-step transformation method is made on a synthetic dataset to estimate the resolving power. The used model parameters are given in Table 6.1 for model 1. The first geophone is placed 2.5m away from the source and the receivers with 2.5m interspace between each other. Each receiver or channel comprises three traces to sample each space direction. If we speak in the following about traces, we only regard one trace in each channel. Consecutively, the considered number of traces is equal to the number of channels.
The overall resolution is examined by transforming the trace information into the phase velocity spectrum. Fundamental and two higher modes are separately picked in the phase velocity spectrum with each method and finally compared with the theoretical

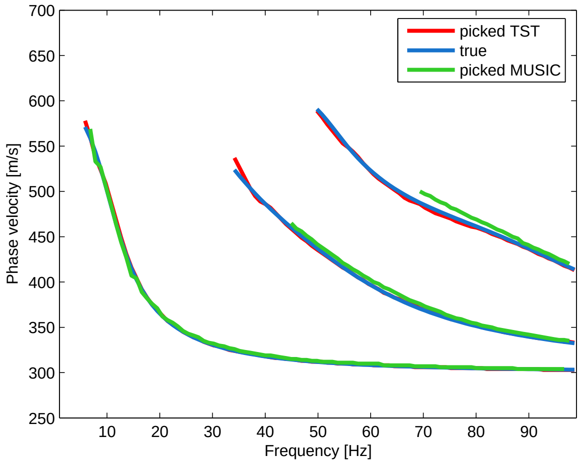

Figure 4.1: A Love wave phase velocity spectrum was calculated for model 1 in Table 6.1 considering 80 traces. The dispersion curves were then picked with the TST and fk-MUSIC method and compared here with the true dispersion curve.

dispersion curve calculated by a forward modeling algorithm after Lai and Rix (1998). A high number of traces, here 80 traces, are transformed. The three-step transformation (TST) resolves the higher order modes better than the fk-MUSIC algorithm (see Figure 4.1). Improved fk-MUSIC algorithms, however, exist and can probably overcome the bad fit of the higher order modes but they are not investigated here.

Another comparison between the methods is carried out considering a few traces. The fk-MUSIC method shows in this case a much higher resolving power. Already five traces lead to a clear, sharp defined dispersion curve image, especially at low frequencies (Figure 4.2a). The wave field transformation method (Figure 4.2b) is not able to produce such a high resolution using a few traces. The fk-MUSIC method is therefore a method of outstanding resolving power when treating with short offset ranges. Working with a limited number of traces hold the risk to neglect frequency information. If we loose either high or low frequency information depends on the offset position of the selected traces. Missing frequency information results in slightly erroneous picked dispersion curves. The curves of both analysed transformation methods tend to have a steeper gradient than the true dispersion curve in the Love wave phase velocity spectrum - see Figure 4.3a. In the Rayleigh wave case (Figure 4.3b), the picked dispersion curves contrarily show a weaker gradient than the theoretical curve. To study these effects of erroneous gradients to the inversion result can be a task for the future.

The important question for SWM is: how should the offset be chosen to achieve the maximum result? Long array lengths allow the seperation of different modes and additionally reduce the data uncertainty since we include more data points. In contrast, short arrays provide a higher S/N ratio and are less influenced by lateral variations and high frequency attenuation. Different offsets are therefore analyzed to determine an

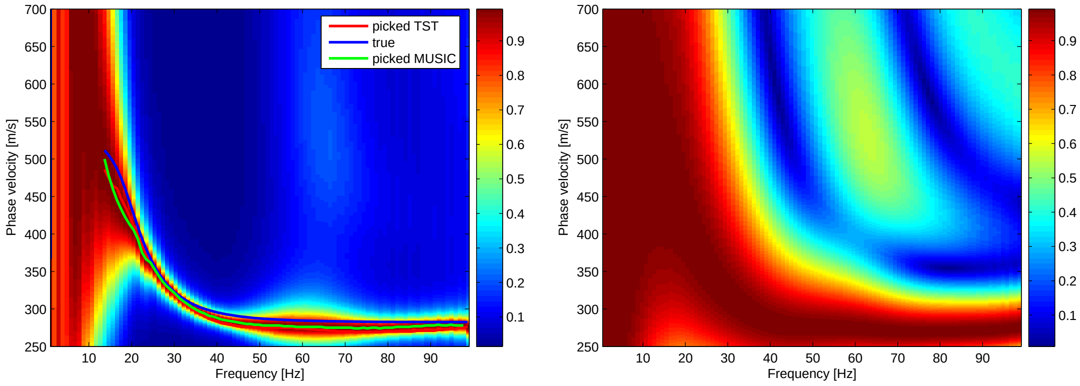
(a) fk-MUSIC method

(b) TST method

Figure 4.2: Trace-normalized Rayleigh wave phase velocity spectra calculated for model 1 in Table 6.1 considering five traces. The synthetic data was transformed with the (a) fk-MUSIC and (b) the three-step transformation method (TST). The true and picked dispersion curve obtained in (b) are illustrated in the phase velocity spectrum (a) together with their corresponding picked dispersion curve. We recognize that the resolution in (a) is superior compared to (b).

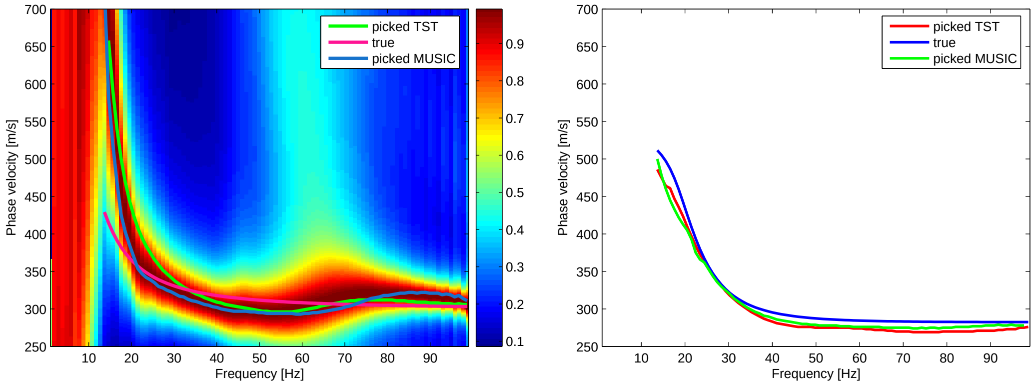
(a) Love wave

(b) Rayleigh wave

Figure 4.3: Trace-normalized phase velocity spectra for Love (a) and Rayleigh (b) waves were calculated based on model 1 in Table 6.1. The background spectrum shown in (a) was calculated with the fk-MUSIC method but both spectra were calculated with the TST and fk-MUSIC method. The corresponding dispersion curves were picked considering five traces away from the source and plotted. They are compared with the true dispersion curve in the Love and Rayleigh wave case and show different gradients in the frequency range between 10-30Hz.

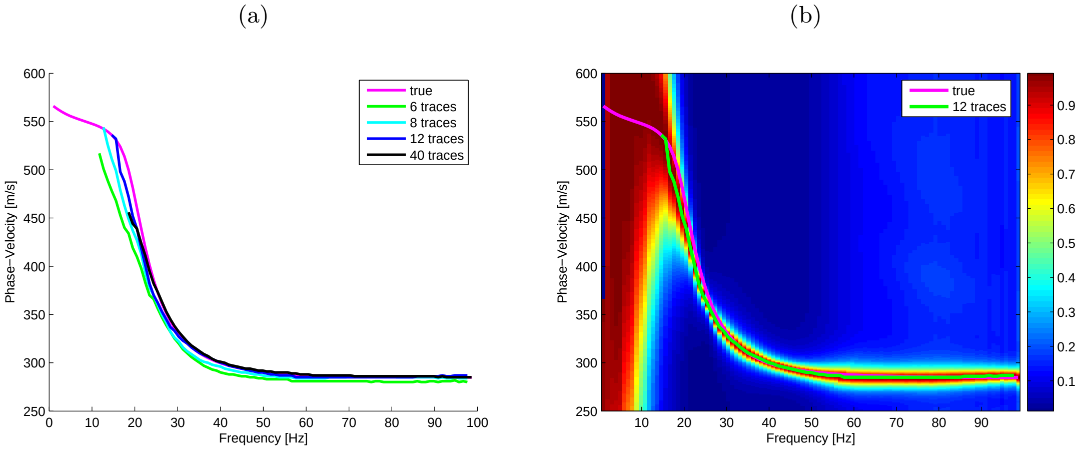
(a)

(b)

Figure 4.4: Dispersion curves were picked in (a) in trace-normalized Rayleigh phase velocity spectra including different offset ranges (traces). The fk-MUSIC was used. We see in (b) that 12 traces are sufficient to fit the maxima in the Rayleigh wave spectrum.

optimal offset range. The same source-receiver array is considered as before where the wave field transformation is conducted by the fk-MUSIC method. Figure 4.4a shows that beyond a certain offset, the dispersion curve fits not better the true curve than a corresponding dispersion curve with shorter offset. In the Rayleigh wave case (Figure 4.4b), we need at least 12 traces or 30m to fit well the true dispersion curve. But even 20m offset (8 traces) are acceptable. As a comparison, a 90m offset (40 traces) does not fit better the true dispersion curve than the one calculated with 30m offset. After Park et al. (1998), a rule of dumb is suggested that the array length should be chosen equal to the desired investigation depth. We found that an offset range of 20-40m is needed to properly resolve two 5m thick layers plus halfspace. This range is appropriate to get accurate fundamental mode dispersion curves and also higher order modes for both surface waves.

5. Inversion theory

Inversion is the key procedure for deriving subsurface models from measured data. A short introduction in terms and techniques of inversion are given here.
Observations, synthetic or real, are a synonym for data labelled with $\mathbf{d}$. The number of observations can be given by N^O. It is often tried to reproduce the nature with a simple model. Such a model contains all major properties to adequately describe the reality. The properties of a model are known as model parameters $\mathbf{m}$ of length M^P. In forward modeling, data is predicted by using the known model parameters. Inverse modeling as opposed uses data to obtain model parameters. The model represents the link between data and model parameters. In our surface wave and first arrival problem, the model includes the theoretically derived wave, dispersion and refraction equations. S-wave velocity and layer thickness represent the variables, which we want to get out from the inversion process. To reduce the number of variables for which have to be inverted, the P-wave velocity is fixed on the basis of a pre-defined Poisson's ratio using equation 2.23 and densities of the layer using equations 2.24 and 2.25. Figure 5.1 illustrates the SWM and its inversion step. We minimize for

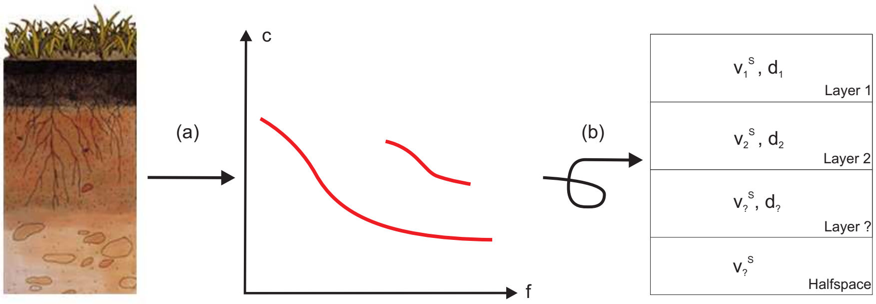

Figure 5.1: Surface waves are aquired in a 3-C survey and processed (a) to obtain dispersion curves. These curves are inverted (b) with an appropriate model to gain subsurface parameters.

$$\mathbf{d} - \mathbf{g}(\mathbf{m}), \tag{5.1}$$

where $\mathbf{g}$ indicates the link between observed data and model parameters also known as data kernel (Menke, 1989; Tarantola, 2005). We can express $\mathbf{g}(\mathbf{m}) = \mathbf{d}^{syn}$, where $\mathbf{d}^{syn}$ represents the theoretically calculated data obtained by estimated model parameters. A reformulation of the minimization problem leads to

$$\mathbf{e}^M = \mathbf{d}^{obs} - \mathbf{d}^{syn}, \tag{5.2}$$

where $\mathbf{e}^M$ is known as prediction error, residual vector or misfit. In other words, we minimize the error between measured and modeled data. The cost-function is defined as the sum of these errors and denoted with C. If the cost-function finally becomes zero, the model parameters perfectly fit the observed data. We can also look to equation (5.1) and imagine a n-dimensional surface, where we seek for the maximum likelihood point of the data distribution. The maximum likelihood point is defined as the most likely measurement with the highest probability.
Some outliers or bad data points are usually present in a dataset. Therefore, we try to minimize the data using equation 5.2, which is a L_1-norm and robust to outliers.

5.1. Cost-functions for inversion

The aim is to solve equation (5.1) for unknown model parameters. This is an optimization problem. We subsequently discuss cost-functions, which are the basis to jointly invert Love, Rayleigh and refracted waves.

5.1.1. Separate and joint inversion of refracted P- and S-waves

First arrivals of P- and S-waves can be inverted using equation 2.29. The corresponding cost-function $C^{\{P,S\}}$ for P- and S-wave first arrivals can be written as

$$C^{\{P,S\}}\left(v_{N^L}^{\{P,S\}}, h_{N^L-1}\right) = \sum_{n=1}^{N^T} \frac{\left| t_{Data}^{\{P,S\}}\left(t_n^R\right) - t_{Theo}^{\{P,S\}}\left(t_n^R, v_{N^L}^{\{P,S\}}, h_{N^l-1}\right)\right|}{N^T}, \tag{5.3}$$

where the variable $t^{\{P,S\}}$ indicates the travel time of P- and S-wave first arrivals, t^R is trace and N^T is the number of considered traces. A joint inversion of refracted P- and S-waves can be performed:

$$C^{P,S} = C^P + C^S. \tag{5.4}$$

5.1.2. Separate inversion of Love and Rayleigh waves

Observed dispersion curves are used to deduce the medium parameters v^S and thickness. v^P, which also influences the Rayleigh wave dispersion curve, is indirectly calculated from v^S using the Poisson's ratio - see equation 2.23. For each frequency, the error between observed and theoretical phase velocity is calculated (van der Kruk et al., 2006) and the relative error is minimized by inverting for the medium parameters. The cost functional $C^{\{L,R\}}$ for Love (L) and Rayleigh (R) waves for a certain mode N^M can be written as

$$C^{\{L_{N^M},R_{N^M}\}}\left(v_{N^L}, h_{N^L-1}\right) = \sum_{n=1}^{N^F} \frac{\left| v_{Data}^{\{L_{N^M},R_{N^M}\}}\left(f_n\right) - v_{Theo}^{\{L_{N^M},R_{N^M}\}}\left(f_n, v_{N^L}, h_{N^L-1}\right)\right|}{N^F}, \tag{5.5}$$

where v_{Data} indicates the phase velocity of the picked dispersion curve and v_{Theo} represents the velocity of the calculated theoretical dispersion curve. Subscript N^L defines the number of layers including the homogeneous halfspace and N^F is the number of frequencies.

5.1.3. Joint inversion of Love and Rayleigh waves

Similar as described for GPR by van der Kruk (2006); van der Kruk et al. (2007), a joint inversion can be performed for seismic data by combining Love and Rayleigh wave modes:

$$C^{L_{0..NM}-R_{0..NM}} = C^{L_0} + ... + C^{L_{NM}} + C^{R_0} + ... + C^{R_{NM}}. \tag{5.6}$$

Of course, arbitrary modes can be combined so that an optimal inversion can be carried out. The more modes can be regarded, the better the result will be. We often encounter the case that for Rayleigh wave data, only the fundamental modes can be picked. Assuming that in the same experiment the fundamental and first higher mode for the Love wave can be picked, we can minimize for

$$C^{L_{01},R_0} = C^{L_0} + C^{L_1} + C^{R_0}. \tag{5.7}$$

5.1.4. Joint Pareto inversion of refraction and dispersion data

Beside dispersion, also reflection and refraction information can be extracted from a seismic record. Dal Moro and Pipan (2007a) presented a procedure to jointly invert reflection and Rayleigh wave dispersion data as well as refraction and Rayleigh wave dispersion data (Dal Moro & Pipan, 2007b) based on the concept of Pareto optimal solutions. The idea is to solve a multi-objective problem (MOP) with often conflicting quantities and constraints.

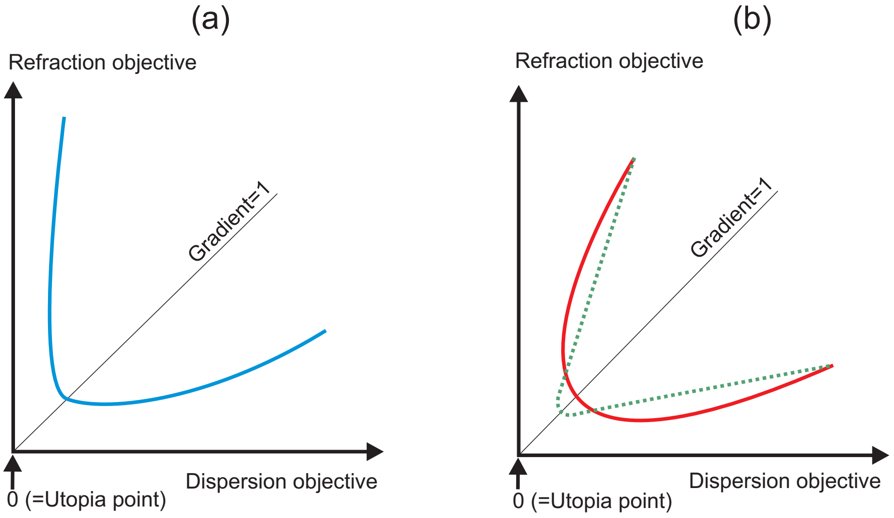

Figure 5.2: Pareto fronts of a bi-objective problem are shown for (a) severely-conflicting objective functions and (b) correct (dashed line) and misinterpreted (solid) models.

Pareto based techniques use the dominance criterion to find an optimal set of solutions. When such a set is plotted in an objective space, nondominated solution vectors define the Pareto front (van Veldhuizen & Lamont, 2000). Nondominated as such that no improvement in one of the objective function leads to a dominating solution vector with respect to the previous one. No better function value can be obtained in one objective without producing a simultaneous degradation in one of the other objectives. A set of possible solutions is generated by evaluating each objective function separately. Based on the resulting model parameters, the corresponding objective error of the other objective functions is calculated to obtain a point in the n-dimensional objective space. In our case, we combine dispersion curve and refraction travel time minimization and hence deal with a bi-objective problem. The shape of the Pareto optimal front shows, if we are dealing with severely-conflicting objectives (Figure 5.2a) and if we correctly interpreted the number of layers and refraction data (Figure 5.2b).

5.1.5. Joint relative inversion of refraction and dispersion data

Another way to invert objectives with different physical units is to include their corresponding relative errors in one dimensionless misfit functional. It is further abbreviated as relative-objective problem (ROP). To obtain the relative error of the dispersion cost-function of equation 5.5, we simply divide the argument by the theoretical calculated value at each frequency. We read

$$C^{\{L_{NM},R_{NM}\}} = \sum_{n=1}^{N^F} w^D\left(f_n\right) \frac{\left(\frac{\left| v_{Data}^{\{L_{NM},R_{NM}\}}(f_n) - v_{Theo}^{\{L_{NM},R_{NM}\}}\left(f_{n,v_{NL},h_{NL-1}}\right)\right|}{v_{Theo}^{\{L_{NM},R_{NM}\}}(f_{n,v_{NL},h_{NL-1}})} \right)}{N^F}, \tag{5.8}$$

where w^D is a weighting factor. It ensures that higher misfits in regions of high uncertainty do not dominate over low misfits in regions of small uncertainty. Dal Moro and Pipan (2007a) proposed $w^D(f_n) = \sqrt{\frac{f_n}{f_{n_{max}}}}$. In a similar way, we can write a relative objective function $C^{\{P,S\}}$ for the P- and S-wave first arrivals

$$C^{\{P,S\}} = \sum_{n=1}^{N^T} w^R\left(t_n^R\right) \frac{\left(\frac{\left| t_{Data}^{\{P,S\}}\left(t_n^R\right) - t_{Theo}^{\{P,S\}}\left(t_n^R, v_{NL}^{\{P,S\}}, h_{NL-1}\right)\right|}{t_{Theo}^{\{P,S\}}\left(t_n^R, v_{NL}^{\{P,S\}}, h_{NL-1}\right)} \right)}{N^T}. \tag{5.9}$$

w^R is a weighting factor and has the same purpose as w^D. A joint inversion is accomplished by combining our dispersion and refraction objectives as

$$C = C^{\{L_{NM},R_{NM}\}} + C^{\{P,S\}}. \tag{5.10}$$

It is worthwile to mention that dispersion curve minimization is slower than first arrival curve minimization. This is mainly due to the time intensive forward modeling of the strongly nonlinear dispersion curve but also dependent on the number of considered frequencies.

5.2. Inversion methods

This section presents suitable methods to solve non-linear mixed-determined inverse problems. The non-linear optimization problem usually comprises several minima. The aim is to find the global minimum in stead of a local minimum. These kind of inverse problems can be solved with a combination of global- and local-search algorithms.

5.2.1. Global search methods

Global approaches have in common that they find the region near the global minimum by seeking over the entire solution space. We describe the two methods, which we have tested below.

Pattern search

Pattern, direct or grid search is a simple method, where the search space for each model parameter is sampled between the search boundaries.

Genetic algorithm

A more sophisticated global search method is the Genetic algorithm or abbreviated GA. It can be seen in analogy to a biological evolution system. Starting models represent an initial gene sequence. Reproduction of the fittest leads to the result that the models with the smallest value of the objective function survive but not only. The mimiking of crossover and mutation of models give unfit ones the chance to survive as well. The advantage of this algorithm is that it converges fast and is robust. In addition, it can be run in defined limits without setting explicit starting models (Faeh et al., 2001, 2008; Dal Moro et al., 2006, 2007). A disadvantage is that there is not always found a global minimum. Since fit models are continuously enriched in the inverse procedure, it becomes difficult to partly escape local minima. Further is to say that we also tested this algorithm as local searcher.
Another frequently used global search method is the Monte Carlo method. Due to time intensive computational effort, the two previously mentioned algorithms are initiated. But for further reading, Tarantola (2005) and Socco and Boiero (2008) is recommended.

5.2.2. Local search methods

Local search methods are iterative schemes, which try to converge by generating improved starting models at each iteration.

Occam's inversion

We employed the Occam's inversion scheme in combination with the global grid search algorithm. The smoothest profile of the model parameter is tried to find by minimizing the objective function. This procedure calculates the forward problem to obtain theoretical dispersion curves and linearizes the functional of the current model parameters. Linearization of the functional comprises the description of the Jacobian matrices of the Rayleigh and Love wave velocities. The remaining constrained inverse problem is solved by using the *Lagrange multiplier* (Menke, 1989), where the multiplier itself acts as a smoothing parameter. The necessary equations for the inversion input for Rayleigh waves are given by Lai and Rix (1998) and for the corresponding Love waves by Safani et al. (2005).

Simplex search algorithm

The Simplex algorithm is a widely used direct search method (Lagarias et al., 1997; Lewis et al., 2000), which acts as a local optimizer. This class does not follow gradients or higher derivatives but implements an initial pattern or grid, from where the minimization is started.

A positive space of data and model parameters is assumed. The constraint of the non-negative space defines a convex polyhedron in the solution space (Menke, 1989). The solution is then located at the boundary of the polyhedron so that the search after a solution is initiated at an arbitrary extreme point (vertex). This algorithm follows the deepest descending edge to the next extreme point (Tarantola, 2005) until the solution at one of the polyhedron's vertices is found. If there is no solution, a point outside of the polyhedron is introduced and the procedure starts from the beginning until a minimum of the objective function will be achieved. Advantages of the method are that almost any objective function can be minimized. The minimization, however, is memory and time intensive as well as there is not always a solution found.

5.3. Applied approach

Inversion is performed after processing raw data. A multilayer algorithm was developed based on an existing two layer inversion algorithm from GPR (van der Kruk et al., 2007) and applied to seismics by Werthmüller (2007). The aim was to be able to jointly invert multilayer models using Rayleigh and Love waves and P- and S-wave first arrivals. Such multilayer models are conducted to enhance the resolution of the inverted model (Xia et al., 2002) and to examine efficiency and stability of the inversion algorithm (Xia J., 1999). Faeh et al. (2008) further recognized that if more geophysical layers are inverted than lithological units, even velocity gradients within layers are resolvable.

There are different ways to perform an inversion using first arrival and dispersion information. An overview is given in Figure 5.3.

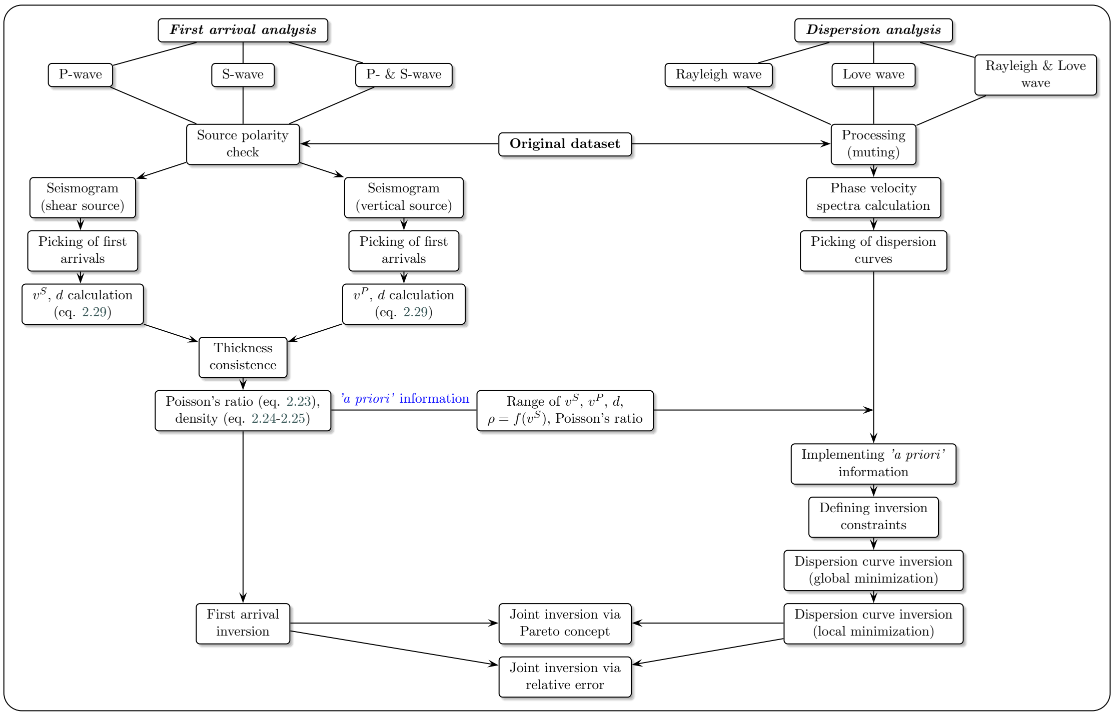

Figure 5.3: Flowchart to separately and jointly invert first arrival and dispersion information

5.3.1. Applied global search scheme

Depending on the implemented global minimizer, initial model parameters are explicitly defined (pattern search methods) or generated between given boundaries (methods with adaptive sets of search directions). Basically, the more sampling steps and layers are considered, the higher is the number of calculated initial models (e.g. for four step increments and three and four layers, 4^5 and 4^7 models are respectively calculated. The use of more than four layers considering the same or higher number of steps makes pattern search inefficient due to the computational effort. In this case, other global search algorithms (e.g. GA) provide better efficiency.
For all initial models, a dispersion curve is calculated using the forward modeling algorithm after Lai and Rix (1998), which solves the eigenvalue problem of an elastic, vertically heterogeneous model for Rayleigh waves. Appendix A describes the Rayleigh wave forward modeling for a two-layer model. The solution for Love waves was implemented by van der Kruk and is described in section 3.1.1 for a two-layer model.
The inversion variables are only S-wave velocity and thickness. Since P-waves have a limited influence on dispersion curves, the corresponding P-wave velocity is fixed through a pre-defined v^P/v^S from first arrival analysis. Note, one v^P/v^S ratio is used for all layers. Picked and calculated dispersion curves are then compared in the cost-function (e.g. equation 5.5). The absolute error between these curves and frequency overlap is written out. To ensure that only dispersion curves with a low cost-function and high

frequency overlap are employed, a frequency constraint (RA) is introduced. In our case, models with a frequency overlap of less than 90% are neglected. Furthermore, models with a misfit of zero between picked and calculated dispersion curve are ignored.

Many models are often left from the global search having a low cost-function and high frequency coverage with the theoretical dispersion curve. To narrow again the number of best initial models, a function is integrated comprising a zero-finding routine. A pre-defined number of models is chosen, where the ones with the lowest cost-function survive. Our default value is set to 30. The parameters of those models are minimized with a local search algorithm.

5.3.2. Applied local search scheme

Local search begins optimizing at the selected models returned from the global search. The model, which generates the lowest cost-function value obtained from the local search, is assumed to be the global minimum and forms our inversion result.

Two local minimizer were conducted: Occam's inversion and Simplex search. First minimizer showed poor converging efficiency in cases, where the starting model was too far away from the true one whereas the second one was robust and converged well. It finally turned out that the combination of the pattern search (global optimizer) and Simplex search (local optimizer) algorithm leads to the optimum result. This combination is robust, converges in an adequate time frame and is used unless otherwise mentioned.

6. Synthetic data

Synthetic seismograms are generated by Sabine Latzel[1] using a forward modeling algorithm originally written by Friederich and Dalkolmo (1995). They are calculated for a point (delta) source located at the origin over a horizontally layered three-dimensional earth. The wavelet has a frequency bandwidth of 1-60Hz. In the following, we discuss the processing and the inversion results.

6.1. Models

Several synthetic models were adopted from literature and generated. Table 6.1 gives an overview of the models and corresponding density, P- and S-wave velocity as well as thickness. The quality factors, which are a measure of seismic wave attenuation, are set to $Q^K = 100$ and $Q^\mu = 50$. In the following, only results of model 1 are presented and further discussed. Models 2-10 were also processed to verify the obtained results.

Table 6.1: Model parameters with velocity in [ms^{-1}], thickness [m] and density [gcm^{-3}]

	v_1^P	v_2^P	v_3^P	v_1^S	v_2^S	v_3^S	d_1	d_2	ρ_1	ρ_2	ρ_3
model 1:	1000	1500	2000	300	450	600	5	5	1.7	2	2.3
model $2^{a)}$:	800	1200	1600	400	600	800	10	10	1.8	2.2	2.6
model $3^{a)}$:	1750	1875	2000	400	600	800	5	5	1.8	2.2	2.6
model $4^{b)}$:	340	1120	1900	140	620	1100	8	8	1.7	2.05	2.4
model $5^{b)}$:	340	2770	5200	140	1570	3000	8	8	1.7	2.05	2.4
model $6^{b)}$:	1100	1450	1800	333	437	540	5	5	1.6	1.8	2
model $7^{c)}$:	1100	1450	1800	590	775	960	10	10	1.6	1.8	2
model $8^{d)}$:	1100	1450	1800	590	775	960	5	6	1.6	1.8	2
model $9^{c)}$:	1100	1450	1800	300	350	400	5	5	1.6	1.8	2
model $10^{e)}$:	650	1725	2800	194	467	740	2	4	1.82	1.96	2.1

---

[a] Adopted (and modified) from Xia et al. (2005)
[b] from Dal Moro et al. (2006)
[c] from Roth and Holliger (1999)
[d] from Roth et al. (1998)
[e] from Xia J. (1999)

---

[1] PhD-student at the Institute of Applied and Environmental Geophysics, ETH Zürich

6.2. Processing

Model 1 comprises two finite layers of five meter thickness each overlying a semi-infinite homogeneous halfspace. The upper, intermediate layer, and underlying halfspace have densities of $\rho_1 = 1.7\mathrm{gcm}^{-3}$, $\rho_2 = 2\mathrm{gcm}^{-3}$, $\rho_3 = 2.3\mathrm{gcm}^{-3}$ and S-wave velocities $v_1^S = 300\mathrm{ms}^{-1}$, $v_2^S = 450\mathrm{ms}^{-1}$ and $v_3^S = 600\mathrm{ms}^{-1}$, respectively. P-wave velocities are chosen $v_1^P = 1000\mathrm{ms}^{-1}$, $v_2^P = 1500\mathrm{ms}^{-1}$ and $v_3^P = 2000\mathrm{ms}^{-1}$. Seismograms for Love and Rayleigh waves are shown in Figure 6.1. One can recognize the dispersion phenomena indicated by the shingling pattern. By comparing both plots in Figure 6.1, we see that the Love wave dispersion clearly differs from the Rayleigh wave dispersion.

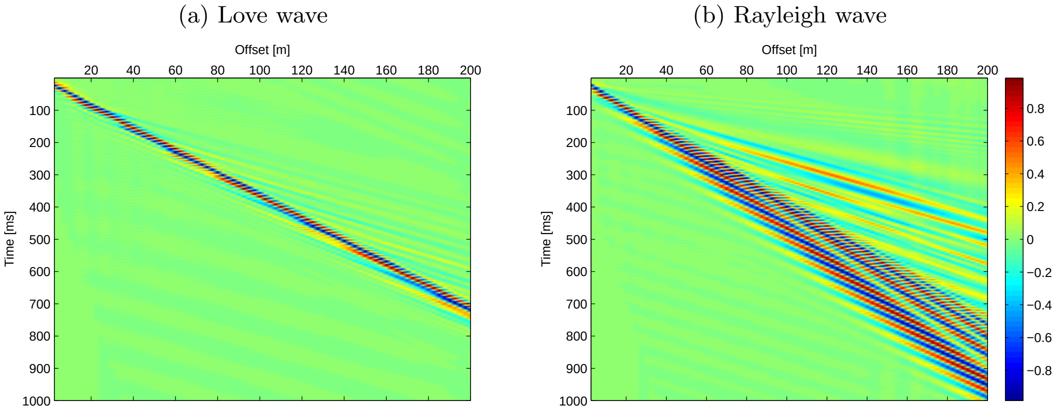

Figure 6.1: Original, trace-normalized seismograms for (a) Love and (b) Rayleigh waves

For obtaining dispersion curves, some processing steps are essential. Raw synthetic data are saved in SEG-Y or SEG-2 format and read in. The average frequency spectrum for the Rayleigh wave data is shown in Figure 6.2a. In a next step, each trace is normalized by its maximum amplitude. The normalization accounts for the offset dependent amplitude-decrease due to energy attenuation in the subsurface. Undesired events like noise, refractions, reflections and the air wave can be supressed by selecting a certain window. Figure 6.2b shows a phase velocity spectrum calculated using equations 4.1-4.3. The maximum amplitudes in the phase velocity spectrum represent the dispersion curve and is obtained by picking the maximal velocities for each frequency (green line in Figure 6.2b). Higher order modes with higher amplitudes can be also identified in Figure 6.2b (not picked).

6.3. Separate and joint inversion results of Love and Rayleigh waves

Below, multilayer inversion results are presented followed by a frequency reduction used to speed up the inversion process.

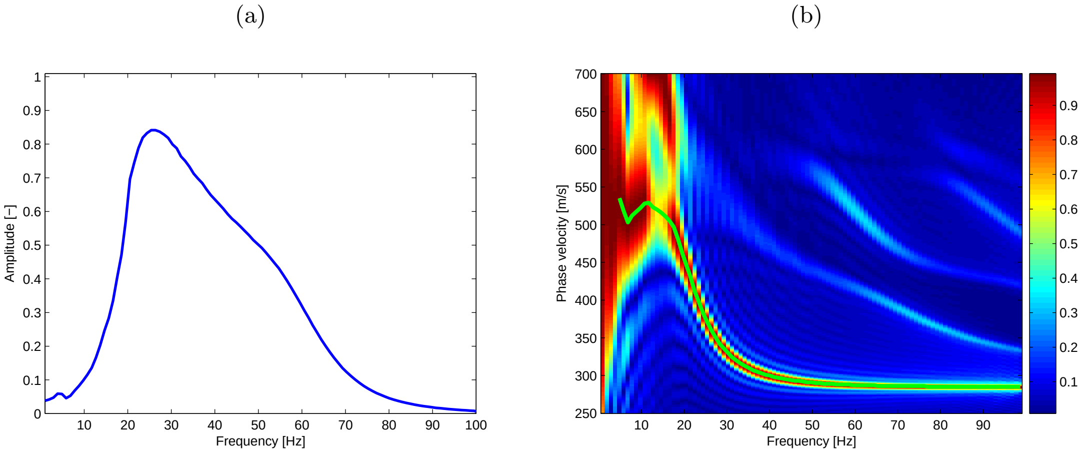

Figure 6.2: (a) Frequency spectrum from the Rayleigh wave seismogram shown in Figure 6.1b and (b) the Rayleigh phase velocity spectrum and picked fundamental dispersion curve (green line).

6.3.1. Multilayer inversion results

Our synthetic three layer model 1 (Table 6.1) is inverted with different initial starting models. The initial search spaces for two, three and four layer inversions are given in Table 6.2. We assume $\rho = 1.5\mathrm{gcm}^{-3}$ and $v^P/v^S = 2.37$ for all layers.

Table 6.2: Search space for 2-, 3- and 4-layer models

	$v^S[\mathrm{ms}^{-1}]$	d[m]		$v^S[\mathrm{ms}^{-1}]$	d[m]		$v^S[\mathrm{ms}^{-1}]$	d[m]
layer 1	200-500	3-10	layer 1	200-500	3-10	layer 1	200-400	3-10
layer 2	400-700	-	layer 2	300-600	3-10	layer 2	300-500	3-10
			layer 3	400-700	-	layer 3	400-600	3-10
						layer 4	500-700	-

Table 6.3 shows 2-, 3- and 4-layer inversion results and their corresponding cost-function values. In Figure 6.3, the Love wave phase velocity spectra are plotted with the L_{012} dispersion curves obtained from the 2-(left), 3-(middle) and 4-layer (right) model inversion. Figure 6.4 shows depth-profiles for the 2-(left), 3-(middle) and 4-layer (right) inversion results. The dispersion curve of the 2-layer inversion does only fit for the higher frequencies. The limited number of parameters only allowed fitting the shallow part (high frequencies) of the model and not the deeper part (low frequencies) of the model. Both dispersion curves for the 3- and 4-layer L_{012} inversions fit the underlying spectra. Table 6.3 further shows that for the L_{012} inversion the upper two layers are correctly inverted by assuming a 2-layer model. Rayleigh wave and joint inversion cannot or only suggestively resolve the second layer. Note that the third layer can not be discovered with any of these inversions.

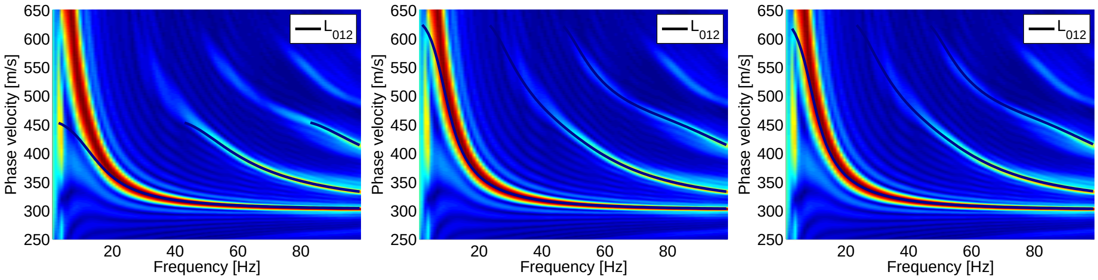
(a) Two layer (b) Three layer (c) Four layer

Figure 6.3: Results from the (a) two, (b) three and (c) four layer L_{012} inversions are plotted as dispersion curves in the Love wave phase velocity spectra. Their values are listed in Table 6.3. Both three and four layer inversion results fit well the true curves also at low frequencies.

Table 6.3: Selected joint Love and Rayleigh wave inversion results for 2-, 3- and 4-layer model

Inversion	Layers	$v_1^S[\mathrm{ms}^{-1}]$	$v_2^S[\mathrm{ms}^{-1}]$	$v_3^S[\mathrm{ms}^{-1}]$	$v_4^S[\mathrm{ms}^{-1}]$	$d_1[\mathrm{m}]$	$d_2[\mathrm{m}]$	$d_3[\mathrm{m}]$	$C[\mathrm{ms}^{-1}]$
true	-	300	450	600	-	5	5	-	-
L_0	2	301.4	582.1	-	-	5.7	-	-	1.3
L_{012}	2	300.9	455.7	-	-	5.0	-	-	12.2
R_0	2	303.2	573.9	-	-	5.3	-	-	1.5
R_{012}	2	298.8	344.9	-	-	2.7	-	-	16.7
L_0R_0	2	301.0	576.3	-	-	5.4	-	-	5.6
$L_{012}R_{012}$	2	306.0	306.0	-	-	3.1	-	-	23.3
L_0	3	299.5	422.8	606.5	-	4.6	3.1	-	0.5
L_{012}	3	300.1	444.6	629.0	-	4.9	5.3	-	5.2
R_0	3	302.7	508.4	273.0	-	5.0	5.8	-	0.2
R_{012}	3	302.7	460.0	281.5	-	5.0	9.7	-	3.7
L_0R_0	3	299.2	400.0	599.0	-	4.2	2.8	-	4.5
$L_{012}R_{012}$	3	302.4	452.1	628.9	-	5.0	5.4	-	20.1
L_0	4	692.5	299.9	398.6	689.2	6.2	9.8	5.4	0.5
L_{012}	4	299.2	301.3	446.1	628.8	1.8	3.1	5.3	5.2
R_0	4	301.8	311.5	557.7	744.1	2.7	2.7	9.5	0.4
R_{012}	4	302.7	457.6	509.5	330.4	5.0	7.7	4.1	5.8
L_0R_0	4	296.9	316.8	503.8	600.0	2.5	2.8	2.9	4.3
$L_{012}R_{012}$	4	302.7	299.3	453.0	629.7	3.3	1.6	5.4	19.9

When assuming a 3-layer model, the inversions map well the true model properties - see Table 6.3 and Figure 6.3b. For the 4-layer inversion, we observe small deviations from the true model for Love and joint inversion in Figure 6.3c. The R_{012} inversion failed in properly recognizing the third layer and indicates a velocity reversal (Table 6.3 and Figure 6.3c).
Analyzing the cost-function values in Table 6.3 shows that a correct assumption of the number of layers results in the smallest cost-function value and all inversions show similar results (Figure 6.4b). In a few cases, the 4-layer inversions have a similar (L_0 and L_{012}) or even smaller (L_0R_0 and $L_{012}R_{012}$) cost-function values. For the L_0R_0, $L_{012}R_{012}$ and L_{012} 4-layer inversions, the upper layer values have almost identical properties as the 3-layer inversions. The L_0 inversion result is too little constrained for a 4-layer inversion. Here, the higher order modes indicate that this inversion result is not correct (see Figure 6.5).
In general, velocities and layer thicknesses are slightly overestimated by inversion with increasing depth. Sometimes, wrong inversion results were obtained with low misfit values. Analyzing the phase velocity spectrum and the dispersion curve of the inversion results shows then that the frequency coverage parameter (RA) was set too low. As a consequence, higher values for RA should be used if the dispersion curve is reliable.

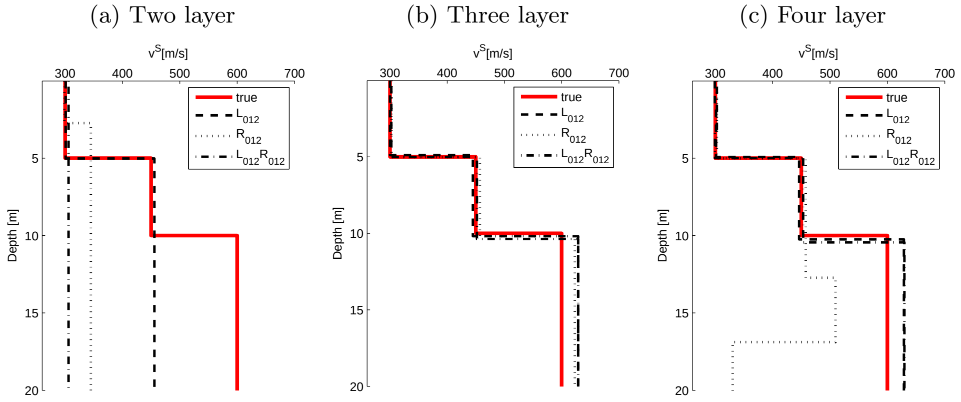
(a) Two layer (b) Three layer (c) Four layer

Figure 6.4: A three layer model was inverted with (a) two, (b) three and (c) four model layers. The Love and joint surface wave inversions fit the true model best. Letters L and R stand for Love and Rayleigh wave and the subscripts for the incorporated modes.

6.3.2. Frequency reduction

Inversion of dispersion curves over a great frequency range is time intensive. Consider that a fundamental dispersion curve can be picked from ~1-100Hz with a sampling of 1Hz - see for example Figure 6.2b. In this case the cost-function is called a hundred times. Dal Moro et al. (2007) stated that in a phase velocity spectrum image going from 1-80Hz, a frequency reduction up to 50% of the high frequency range does not limit the accuracy of the retrieved model. This is only true, if the considered higher order modes lie in the calculation range. In other words, the tails of the dispersion curves, which vary only slightly decrease with higher frequencies and approach the low phase velocity limit, can be cut away to a certain extent. If low frequency parts of the dispersion curves are cut, it reduces the accuracy of the inversion especially for the deeper layers.

Table 6.4: Broad search space and initial parameterization of a three layer model

	$v^S[\mathrm{ms}^{-1}]$	d[m]	$\rho[\mathrm{gcm}^{-3}]$	v^P/v^S
layer 1	100-400	3-10	1.5	2.37
layer 2	400-600	3-10	1.5	2.37
layer 3	600-1000	halfspace	1.5	2.37

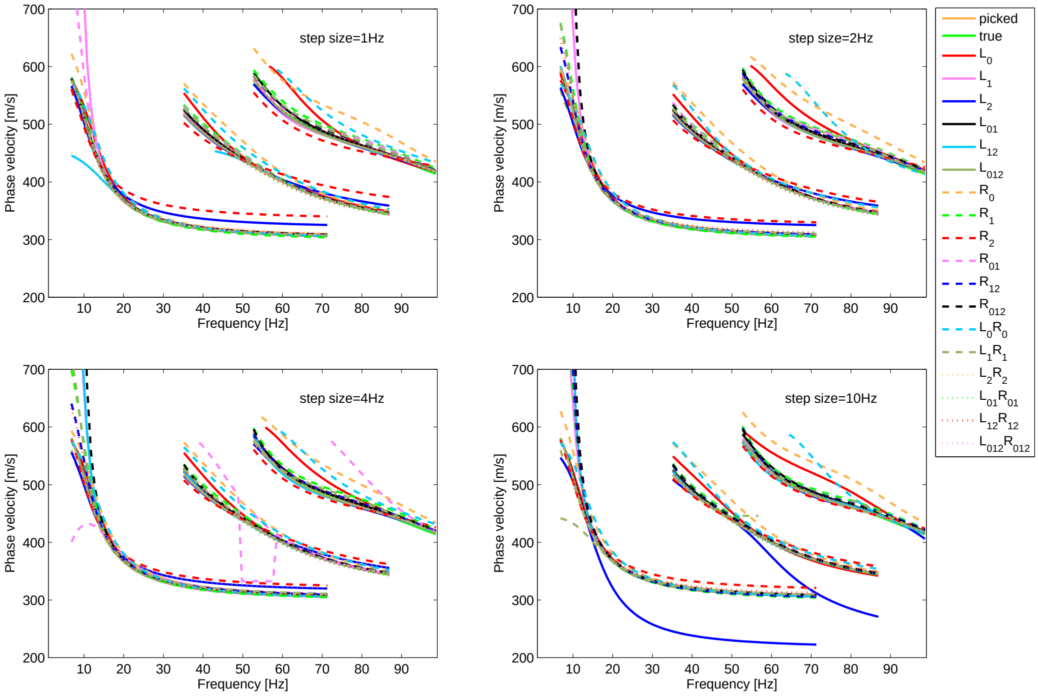

Figure 6.5: Inversion results with search space given in Table 6.4 are plotted as dispersion curves. The picked dispersion curve was sampled with 1, 2, 4 and 10 Hz frequency steps. Up to 4 Hz steps, no harmful effect on the inversion result can be observed.

Aside from a reduction of the considered range limits, frequency steps of the dispersion curve can be increased. We tested how a larger frequency sampling influences the accuracy of the results. Inversions were run for the following step sizes: 1, 2, 3, 4, 6, 8 and 10 Hz. The search space and initial parameterization is given in Table 6.4. Figure 6.5 illustrates the fit of their dispersion curves for certain frequency steps. Selected inversion results are tabulated in Table 6.5. A good fit is guaranteed up to a step size of 4 Hz for the chosen model. With increasing frequency steps, the overlap of the inverted curves decrease. In particular, single mode inversions tend to stronger deviations with increasing frequency steps from the true dispersion curve. As in other inversions, velocity of the deepest layer is generally overestimated. A glance on Love and joint inversion results with higher order modes (results not shown) reveals less fluctuations of the model parameters. Optimizing the frequency range and step size considerably speed up the inversion process. Accuracy of the inversion with large frequency steps is mainly assured, if Love or joint inversion can be conducted and higher order modes are integrated. If only fundamental modes can be identified, frequency sampling can be done with only 2 or 3 Hz. Note that the accuracy of the frequency steps strongly depends on the curvature of the picked dispersion curve.

Table 6.5: Selected inversion results from Figure 6.5 for various frequency steps

	step size [Hz]	$v_1^S[\mathrm{ms}^{-1}]$	$v_2^S[\mathrm{ms}^{-1}]$	$v_3^S[\mathrm{ms}^{-1}]$	d_1[m]	d_2[m]	$C[\mathrm{ms}^{-1}]$
true	–	300.0	450.0	600.0	5.0	5.0	–
L_0	1	299.3	408.4	605.8	4.5	3.0	0.5
L_0	2	299.8	442.0	607.0	4.8	3.4	0.4
L_0	4	299.7	437.3	605.3	4.8	3.1	0.3
L_0	10	300.7	498.2	615.0	5.2	5.3	0.1
R_0	1	302.6	499.7	664.4	4.9	5.4	0.3
R_0	2	302.8	482.0	623.5	4.9	3.9	0.2
R_0	4	302.9	482.9	624.0	4.9	3.9	0.2
R_0	10	302.7	512.9	673.3	5.0	6.1	0.1
L_0R_0	1	299.3	431.0	601.1	4.5	3.1	4.5
L_0R_0	2	298.0	364.9	594.3	3.8	2.7	4.4
L_0R_0	4	298.8	428.1	599.9	4.5	2.9	4.6
L_0R_0	10	298.4	367.4	595.9	4.0	2.4	4.0
$L_{012}R_{012}$	1	302.3	452.1	628.9	5.0	5.4	20.1
$L_{012}R_{012}$	2	302.8	451.8	650.6	5.0	5.5	20.0
$L_{012}R_{012}$	4	302.7	451.4	628.8	5.0	5.3	21.1
$L_{012}R_{012}$	10	302.4	451.4	628.7	5.0	5.3	21.0

6.4. Integration of refraction information to find the optimized search space

Refraction information is used to calculate P-, S-wave velocity and thickness of each identifyable layer (eq. 2.29) and to find optimal starting ranges of the model parameters. Appendix C describes this in more detail. Due to the fact that the first and deepest layer possess a higher accuracy, their limits can be set narrower than for layers in between. The Poisson's ratio is defined using equation 2.23. One ratio is implemented for all layers calculating the v^P/v^S values obtained from the deepest layer.

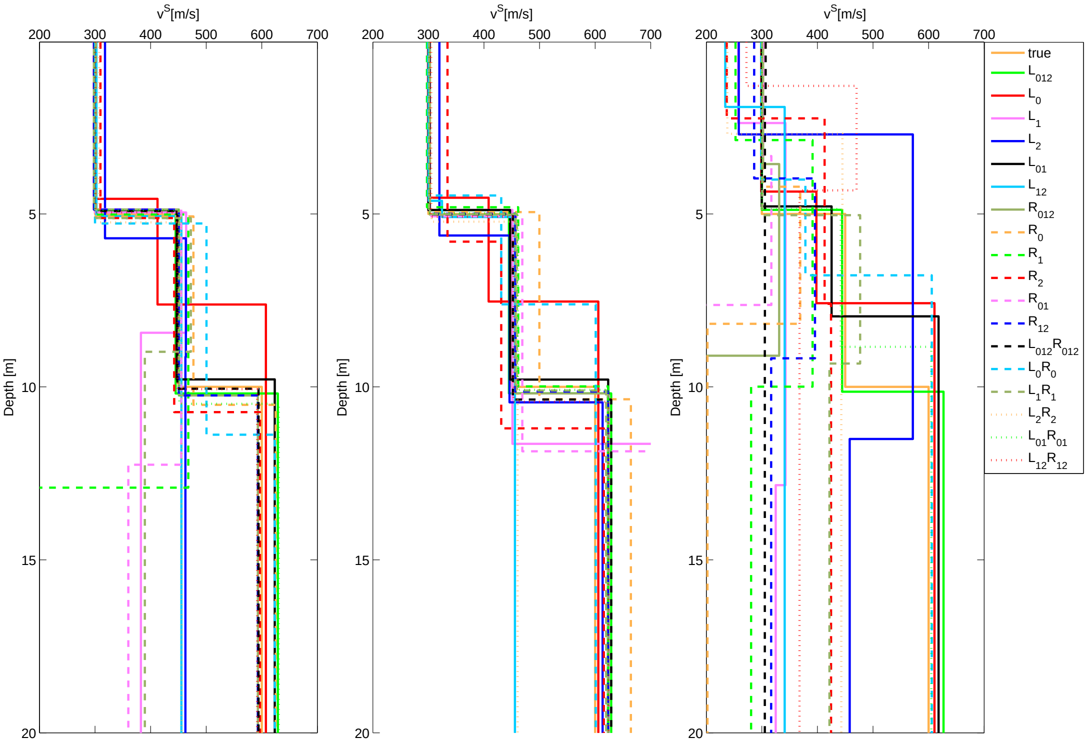

Figure 6.6: Depth-profiles based on dispersion curve inversions with different search space boundaries. The narrow (left), wide (middle) and wrong (right) search space is given in Table 6.6. Some values from the middle depth-profile are listed in Table 6.5 under step size 1Hz.

Table 6.6: Narrow, wide and wrong search space (from left to right)

	$v^S[\mathrm{ms}^{-1}]$	d[m]		$v^S[\mathrm{ms}^{-1}]$	d[m]		$v^S[\mathrm{ms}^{-1}]$	d[m]
layer 1	275-375	3-12	layer 1	100-400	3-10	layer 1	150-200	3-10
layer 2	260-560	3-12	layer 2	400-600	3-10	layer 2	250-350	3-10
layer 3	560-660	-	layer 3	600-1000	-	layer 3	400-600	-

Figure 6.6 shows inversion results as depth-profiles, which are obtained with different search spaces given in Table 6.6. Different starting parameter ranges lead to good inversion results as long as the true model parameters are lying within the correct parameter range. An initial search range, which does not include the true velocity parameters, produces bad inversion results especially for single mode inversions. Pitfalls occur sometimes, if for single mode inversions the starting velocity ranges overlap. In all cases, it is

important to analyze the phase velocity spectrum, the dispersion curves of the inversion results and obtained cost-function values.

6.5. Joint inversion of surface waves and refracted waves

Two different ways to jointly invert first arrival (refraction) and dispersion information are described in section 5.1. Both methods were implemented in a local search scheme after the global dispersion curve minimization using 100 and 250 iterations for first arrival and dispersion curve minimization. We considered SH-wave first arrival information and fundamental mode Love wave dispersion information.

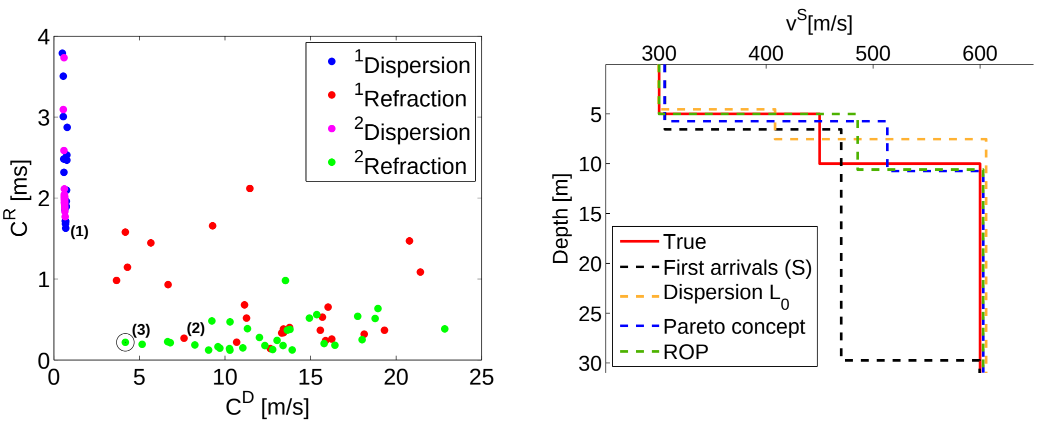
(a) Bi-objective plot (Pareto concept)

(b) Depth-profile

Figure 6.7: The MOP of a fundamental Love wave dispersion curve and S-wave first arrivals solved via Pareto concept shown as (a) bi-objective plot. An envelope around the lowest objective values lead to the Pareto front. The results of the dispersion, joint (Pareto, ROP) inversion and first arrival analysis are plotted as (b) depth-profile and listed in Table 6.7.

Figure 6.7a shows the joint inversion result of our minimization via Pareto concept as bi-objective plot (details in section 5.1.4). The names in the legend stand for the applied inversion whereas the superscripts 1 and 2 indicate first and second local inversion, respectively. C^D and C^R are the dispersion and refraction cost-functions, respectively. After the first local minimization, a new starting model range for each individual minimization (no. (1) and (2) in Figure 6.7a) is obtained for the second run by choosing the parameters between the model parameters of (1) and (2). The red dots and green stars in Figure 6.7a show that we achieved in the second local minimization lower cost-function values. Our finally selected point is marked with an auxiliary circle (no. (3)) and its corresponding model parameters are given in Table 6.7.
The results from the joint inversion via Pareto concept, relative error (ROP), separate dispersion curve minimization and refraction analysis are plotted in Figure 6.7b as depth-profiles together with the true model and listed in Table 6.7. We recognize that v^S of

the first and third layer is almost identical for all methods compared whereas the layer in between is not. Both joint inversions obtain layer thicknesses close to the true model whereas the separate dispersion inversion did not properly resolve the thickness of the middle layer. With the refraction analysis both thicknesses cannot be well reconstructed. A comparison between both joint inversions shows that the optimization via ROP and Pareto optimal concept led to almost identical results with respect to velocities and layer thicknesses, although the ROP minimization slightly fit the true model parameters better.

Table 6.7: Joint inversion results of dispersion and refraction information

	$v_1^S[\mathrm{ms}^{-1}]$	$v_2^S[\mathrm{ms}^{-1}]$	$v_3^S[\mathrm{ms}^{-1}]$	d_1[m]	d_2[m]	C^D	C^R
true	300.0	450.0	600.0	5.0	5.0	-	-
First arrivals	305.4	470.2	599.6	6.5	29.7	-	-
L_0	299.3	408.4	605.8	4.5	3	$0.5\mathrm{ms}^{-1}$	-
Pareto concept	305.0	513.3	603.1	5.7	5.0	$4.2\mathrm{ms}^{-1}$	0.2ms
ROP	300.0	485.6	603.0	5.0	5.6	0.6[-]	

6.6. Discussion

Analysis of different dispersion curve modes shows that higher order modes resolve the uppermost layer(s) better than the fundamental mode. A combination of different modes leads to more accurate results. In the case where only two higher order modes are incorporated, the properties of the lower halfspace are not properly reconstructed. If the fundamental and first higher order mode are inverted, we obtain a good fit for the halfspace and for the overlying layers.

Synthetic modeling disclosed that resulting phase velocities are less sensitive to P-wave velocity changes. As a consequence, P-waves are less important in dispersion analysis. We further observed that Rayleigh wave inversions resolve the model worse than Love wave inversions especially if higher order modes are included. In cases where the fundamental mode is only determined, Rayleigh wave inversions especially reconstruct the thickness of the layers better than Love waves. A joint inversion of both waves leads to more accurate results compared to separate wave inversions.

We finally focused on joint inversions of refraction and dispersion information. In cases where only the fundamental or one higher order mode is extractable from a phase velocity spectrum, joint surface and refracted wave inversions become essential to determine also the deepest layer(s). The velocities of the deepest layers can be better reconstructed. We showed that a joint inversion via relative error and Pareto optimal concept lead to almost identical inversion results. The difference to the ROP minimization is that the Pareto minimization further allows to incorporate the quality of fit and data interpretation (Figure 5.2). In this way, available information can be combined to choose the best inversion result.

An overview of the obtained results is given in Table 6.8. ++, +, ○, - and – indicate, how well the model parameters could be reconstructed after inversion. Note that it is expected that including R_0 in the joint surface and refracted wave inversion will render better results due to the additional constraint. However, this has not been carried out.

Table 6.8: Results of different inversion approaches

	v_1^S	d_1	v_2^S	d_2	v_3^S
L_0	++	○	○	○	+
R_0	++	+	○	+	–
L_0R_0	++	○	+	○	+
First breaks (S) & L_0	++	+	++	○	++

7. Experimental data

In the framework of a site characterization project initiated by the Swiss Seismological Service, measurements were performed in November 2007. Goals of the study are to resolve near-surface layers and their related parameters. First, the experimental set-up is presented, processing steps are explained and finally, results are shown and discussed.

7.1. Data acquisition

The field dataset was collected close to the village Visp in the canton Wallis, Switzerland. The test site was located in the large mountain valley plain, which mainly comprise Quarternary material. These fills are usually fluvial, lacustrine and morain deposits. The top is probably reclaimed land overlain by a few tens of centimeters of soil. Although, boreholes were drilled near the survey area and their cores were geologically described, no intrusive test has been performed at the test site.

7.1.1. Three component P- and S-wave measurements

For recording wave fields in all spatial directions, three component geophones are arranged in an array. The expected useful information that can be acquired lies higher than 4.5Hz (the natural frequency of our geophones). 48 geophones were placed in an array with 2m interspace between each receiver. First shot was set in variable distances in front of the first geophone. Shots were located in between two adjacent geophones with an interspace of 2m.
For obtaining Love and Rayleigh waves, specific sources have to be employed. Waves were induced with the sledge hammer method. Different sources were taken: an iron triangle, iron plate and wooden block as shown in Figure 7.1. The iron plate (a) acts mainly as a vertical source and creates P- and SV- waves, whereas the wooden block (b) acts mainly as a horizontal source exciting SH-waves. As a combined horizontal and vertical source, the iron triangle can be employed (c-e). It is hit from both sides of the triangle indicated with A and B in Figure 7.1. Both A and B shots generate P- and S-waves. Addition of the two datasets obtained by A and B results in constructive and destructive interference of the generated P- and S-waves, respectively, and renders vertical P-waves and Rayleigh wave measurements. Subtraction of the two datasets leads to constructive and destructive interference of P- and S-waves, respectively, and results in horizontal S-waves and Love wave measurements. For most shot points, waves are generated with vertical and crossline source components.

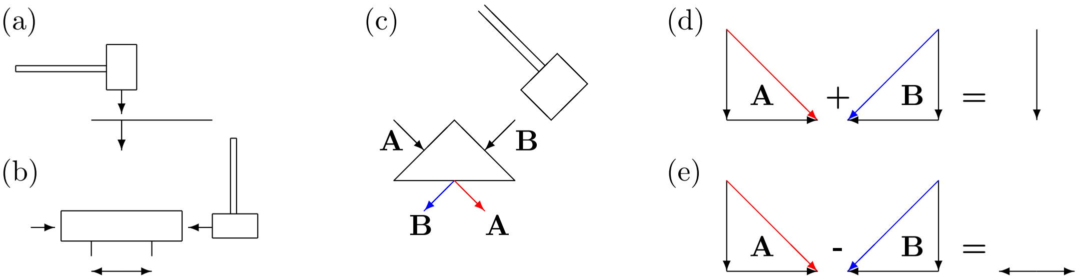

Figure 7.1: Three different sledge hammer methods: (a) the iron plate, (b) wooden block, and (c) iron triangle. In case of the iron triangle, each side is hit. By adding (d) and subtracting (e) the obtained datasets, vertical and horizontal source components could be reconstructed.

7.1.2. Measured data Visp

A six line grid was measured in Visp, Switzerland. Survey location and spanned measurement grid is shown in Figure 7.2a and 7.2b. Note that the yellow stars indicate drilled boreholes and the colored dots represent recording positions of an earlier performed passive seismic investigation done by Roten (2007).

Table 7.1: Acquisition parameters of the three component survey

Shot interval	2m
Number of shots	49 (48 in line 1)
Receiver spacing	2m
Number of geophones	48
Channels	144
Minimum offset	1m
Maximum offset	95m
Sampling interval	0.125ms
Acquisition time	1s
Number of stacks	5

In our survey, all three sources were used. Vertical and horizontal incident waves are generated at every shot point in line 1, 2, and 6. In line 3, 4, and 5, shear waves were only induced at both ends of these lines and in the middle. Due to the large amount of data, not every shot could be processed. Mainly shots were selected, which allowed to analyze a large offset. Therefore, both shot-end positions were preferred as well as the ones in the middle of the lines. If the data quality was not guaranteed, adjacent shot positions were used.

Table 7.2 gives an overview about the source availability of each line. +, ∘, and - stand for the source availability at each shot position, both shot-end positions and in the middle of the line, and no shot position, respectively. Due to the source availability, different analyses (e.g. separate dispersion curve analysis) are performed for the different lines (see Table 7.2).

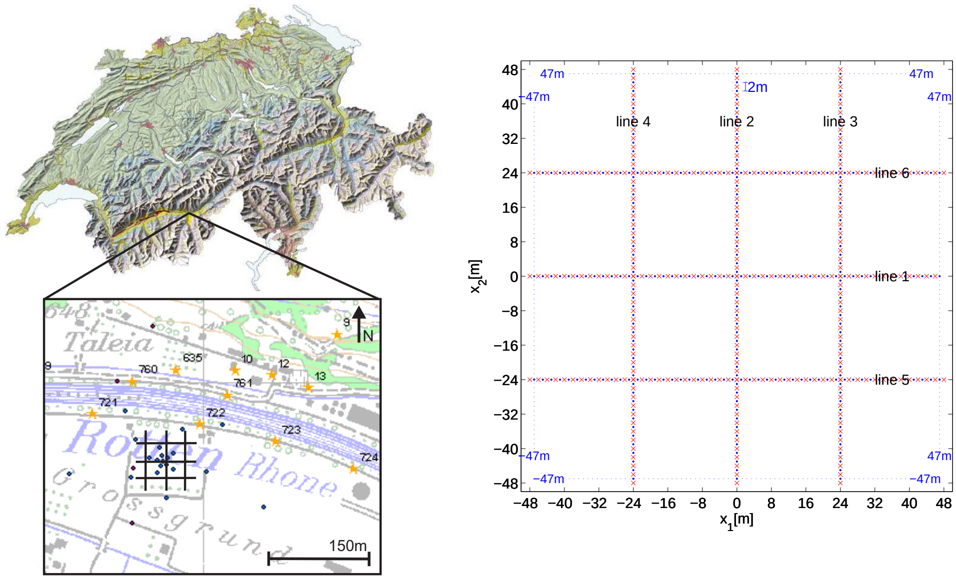

(a) Field location

(b) Measurement grid

Figure 7.2: Measurements were performed in (a) Visp, Switzerland. A six line grid was acquired (b) whereas the blue dots and red crosses mark receiver and shot positions, respectively.

Table 7.2: Source availability: considered lines for the analyses

	Line 1	Line 2	Line 3	Line 4	Line 5	Line 6
Iron plate	+	+	○	+	+	-
Wooden block	+	+	○	-	-	-
Iron triangle	-	-	○	○	○	+
Lateral homogeneity			sec.7.5			
Separate dispersion			sec.7.6.1			
Joint dispersion					sec.7.6.2	
Joint refraction & dispersion						sec.7.6.3

7.2. Source quality

For the iron triangle source, a polarity check was performed by adding and subtracting the vertical and horiontal geophone components shown in Figures 7.3a and 7.3b. The figures confirm that it is possible to obtain separate refracted P- and SH-waves by combining the triangle source since P- and SH-wave first arrivals can be clearly identified within the marked circles for the plot (A+B) and (A-B), respectively. Both the first arrival and dispersion characteristics are different, which indicates that P- and SH-waves are correctly separated.
Figure 7.4 shows a P- and SH-wave seismogram and the corresponding picked first arrivals. Their amplitudes were scaled up to see first breaks at greater offset since they hold little energy. Different seismic sources produce very similar first arrivals what indicates that we can combine inversions of datasets acquired with different sources (Figure 7.5).

7.3. Refraction analysis

After picking the first breaks, the velocity and thickness of each layer were calculated using equation 2.29. The first arrivals shown in Figure 7.5 from line 3 were analyzed and the results are listed in Table 7.3. By examining the P- and S-wave velocities, we observe an extremely low v^P/v^S ratio. If we divide the highest P-wave velocity by the lowest S-wave velocity of a certain layer, we find ratios slight around the lower physical limit of ~ 1.42. This value corresponds to Poisson's ratio of nearly zero. Note that the ticknesses calculated over P- and S-wave first arrivals are different.

Table 7.3: Model parameters from line 3 obtained by refraction analysis

	Line	$v_1^S[\mathrm{ms}^{-1}]$	$v_2^S[\mathrm{ms}^{-1}]$	$v_3^S[\mathrm{ms}^{-1}]$	d_1[m]	d_2[m]
P-wave (iron plate)	3	251.6	296.2	388.3	3.0	8.9
P-wave (iron triangle)	3	274.9	280.6	383.0	7.0	6.7
P-wave (wooden block)	3	252.5	293.9	386.5	3.1	8.4
S-wave (iron triangle)	3	166.4	216.8	279.8	5.3	24.9
S-wave (wooden block)	3	170.6	217.3	293.8	5.2	24.0

7.4. Phase velocity spectra calculation

The main processing to obtain picked dispersion curves is employed in the same manner as in the synthetic case. Some points, which are specifically related to real data processing are pointed out here. Muting in time and offset considerably enhances the resolution of the calculated phase velocity spectrum due to ambient noise. Especially at critical distances in south-eastern direction, where a big company complex (~200m away) is located, we observe a higher noise level. Furthermore, near-field effects are

(a) Vertical geophone components

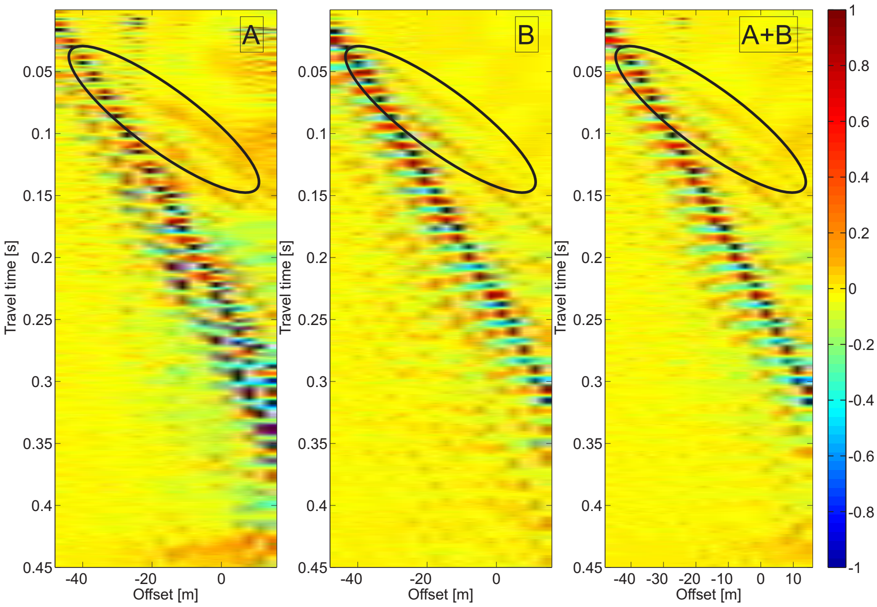

(b) Horizontal geophone components

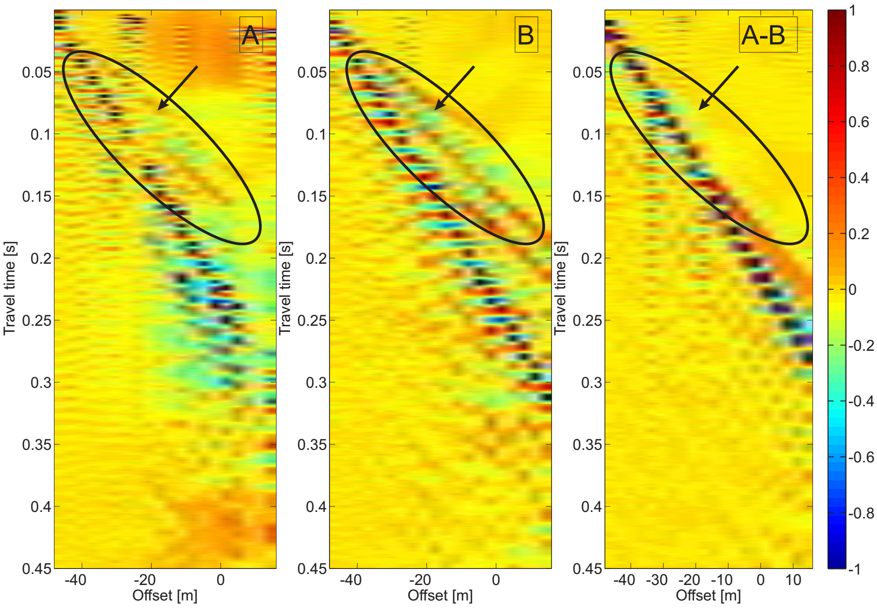

Figure 7.3: (a) and (b) show the vertical and horizontal geophone components, respectively. For (a), A and B are added and show in the A+B seismogram the P-wave first arrivals (black circle) and Rayleigh waves. For (b), A and B were subtracted and the A-B seismogram shows the SH-wave first arrivals and Love waves. Note, the P-wave first arrival are not present anymore (see arrows).

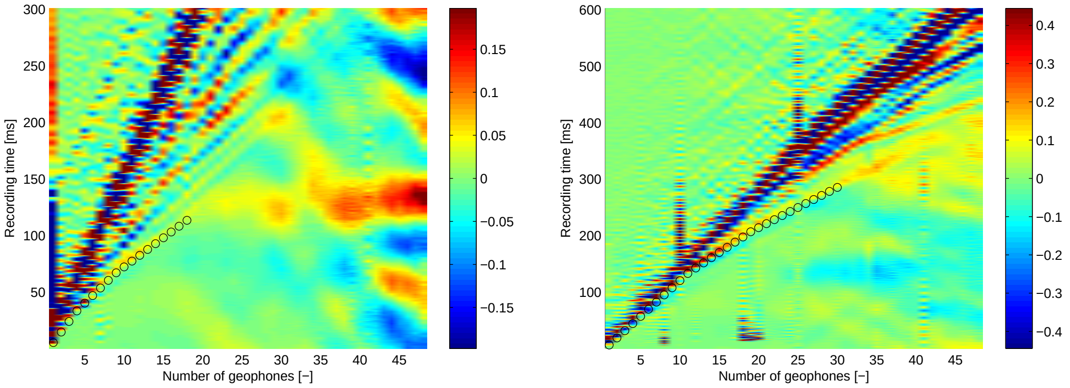
(a) P-wave seismogram

(b) SH-wave seismogram

Figure 7.4: Trace-normalized P- and S-wave seismograms are shown in (a) and (b), respectively. Both shots were generated in line 3 at 48m. The circles indicate the picked first breaks. Due to applied amplification, noise (or artefacts) is blown up and visible at the right side of (a).

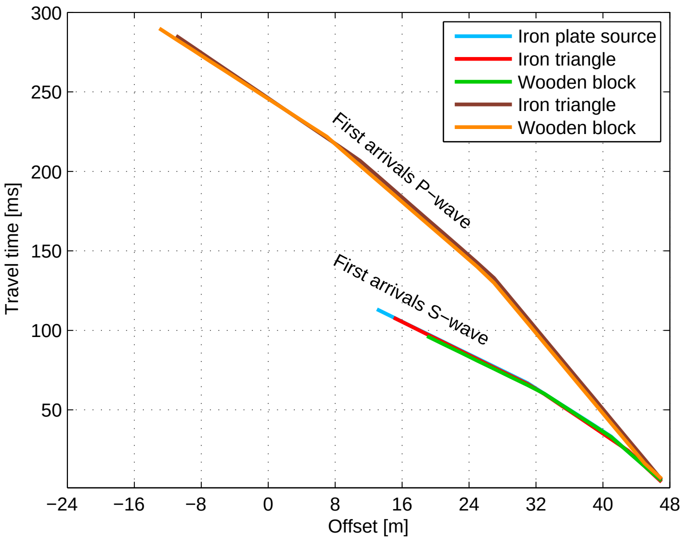

Figure 7.5: Source comparison: P- and S-wave first arrivals obtained with different seismic sources in line 3 at shot point 1. The model parameters obtained by refraction analysis of these first breaks are listed in Table 7.3

present, which are not in accordance with our plane wave assumption. To minimize these effects, seismogram windows are selected starting a few meters ($3-10$m) away from the sources (Stokoe et al., 1994). For obtaining a high S/N ratio and well defined dispersion curves, long offsets (40-80m) are preferred. Due to the relatively high attenuation for long offsets, higher order modes were rarely observed in this case.
Depending on the picked window width, areas in the phase velocity spectrum are more or less pronounced. A clear dispersion curve of the fundamental mode is obtained by choosing a relatively narrow window, which encloses the strong dispersive events. Figure 7.6a shows a shot generated by the iron plate source at position 48m in line 1. The window encloses the dispersion information and leads to the phase velocity spectrum shown in Figure 7.6b. A clear and well defined fundamental dispersion curve is obtained.

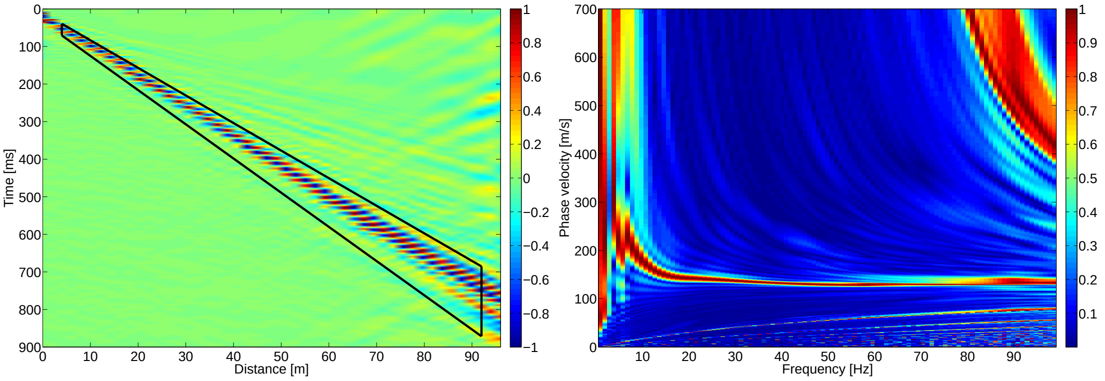
(a) P-wave seismogram

(b) Rayleigh wave phase velocity spectrum

Figure 7.6: Selection of an appropriate window (a) in a seismogram leads to (b) a clear phase velocity spectrum image with well defined fundamental mode dispersion curve.

7.5. Validation of the assumption of lateral homogeneity

To validate the 1D model assumption of the surface wave method, an extended refraction analysis and first arrivals from opposite shot directions were examined in line 3 and 6. Every 4^{th} meter, a shot and altogether 25 shots per line were examined. Figure 7.7 shows histograms of the model parameters from the extended P-wave refraction analysis in line 3 whereas the red star at the bottom of each histogram indicates the mean. The mean and standard deviation (std) of each histogram is given in Table 7.4.

Table 7.4: Mean and standard deviation of the P-wave shotanalysis in line 3

	$v_1^S[\mathrm{ms}^{-1}]$	$v_2^S[\mathrm{ms}^{-1}]$	$v_3^S[\mathrm{ms}^{-1}]$	d_1[m]	d_2[m]
mean	236.4	277.7	358.3	3.3	8.4
std	14.4	17.0	17.1	0.5	2.2

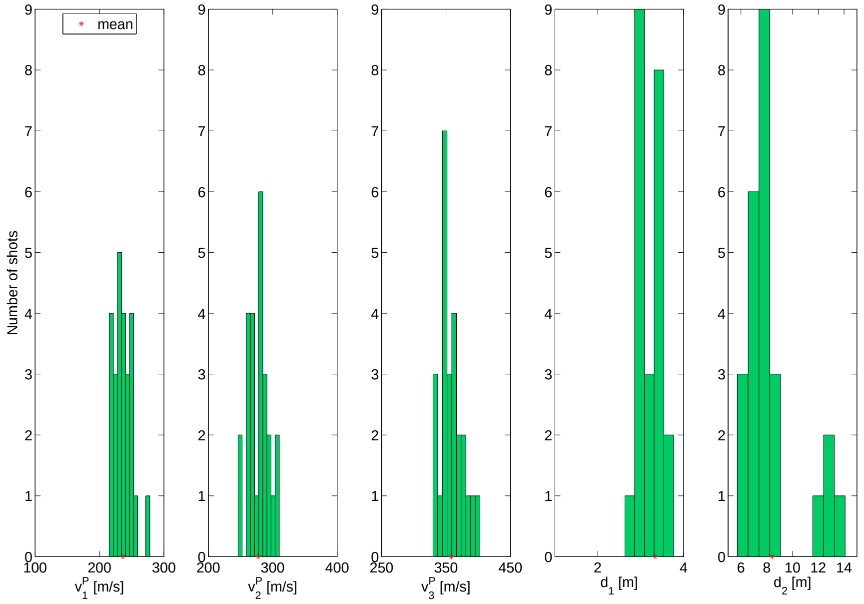

Figure 7.7: A P-wave refraction analysis of 25 shot positions was performed in line 3. Three layers could be identified using the iron plate source.

Note that the obtained information is used to gain a good estimation of model parameter ranges and fed as *'a priori'* information into the inversions. In addition, representative Poisson's or v^P/v^S ratio was obtained.
A similar approach was performed for the SH-waves. The velocities and thicknesses from these expanded analyses in line 3 and 6 are finally assumed to be valid for all other lines too. In addition, we used these parameters to calculate a density (eq. 2.24-2.25) and Poisson's ratio (eq. 2.23) guess for each layer. We also examined and compared histograms obtained with different sources. The smallest standard deviations of model parameters are obtained when acquiring data with the iron plate and iron triangle source. In Figure 7.8 P- and S-wave first arrivals are shown, which were picked from a seismogram with shot positions ±32m in line 6. No severe asymmetry can be recognized, which means that our 1D model assumption is valid. Corresponding velocities and thicknesses obtained by equation 2.29 are given in Table 7.5.

Table 7.5: Model parameters from line 6 obtained by refraction analysis

	Line	v_1^S[ms^{-1}]	v_2^S[ms^{-1}]	v_3^S[ms^{-1}]	d_1[m]	d_2[m]
P-wave (shot 9)	6	254.2	277.6	369.0	3.6	7.9
P-wave (shot 41)	6	275.2	296.6	410.6	3.9	9.1
S-wave (shot 9)	6	184.3	214.5	300.0	3.8	15.1
S-wave (shot 41)	6	200.3	220.6	275.5	4.0	16.6

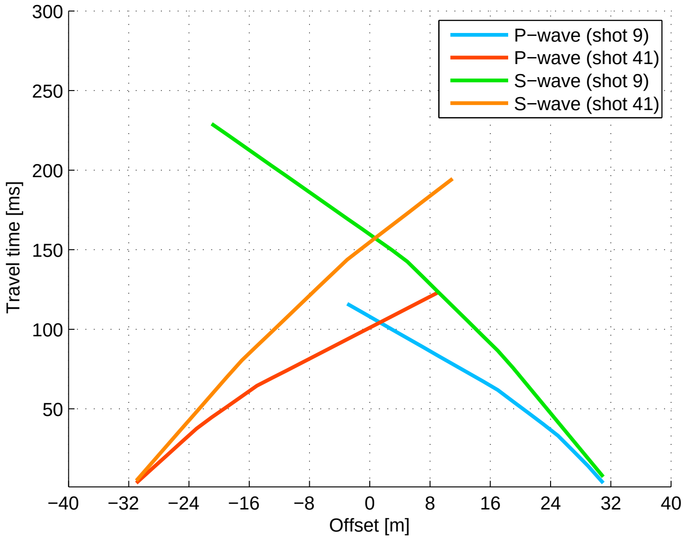

Figure 7.8: To verify our 1D model assumption, P- and S-wave first arrivals from opposite shot positions were picked in line 6. The results are listed in Table 7.5.

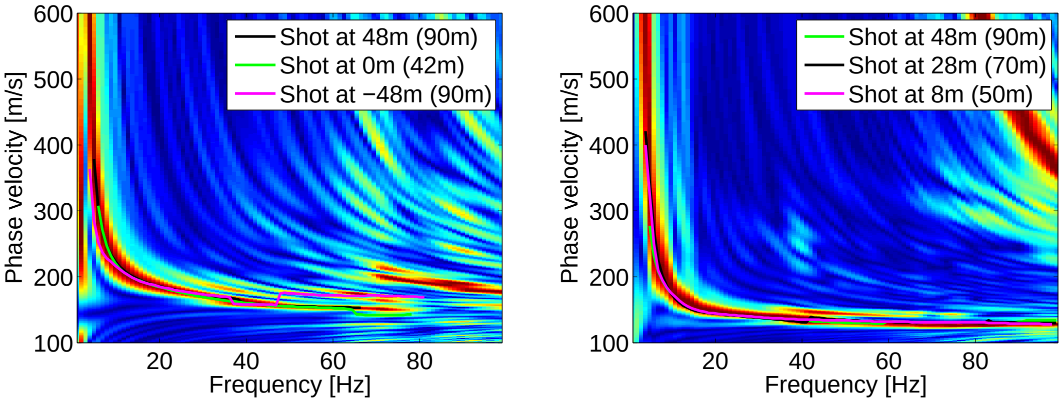

(a) Picked Love wave dispersion curves

(b) Picked Rayleigh wave dispersion curves

Figure 7.9: Dispersion curves are picked in the normalized (a) Love and (b) Rayleigh phase velocity spectra of line 3. Numbers in brackets indicate the considered offset length. The background spectra is calculated for shot positions (a) 48m and (b) 28m.

They show that the second layer is weakly resolved by first arrival analysis. As explained in the Appendix C, slopes of intermediate layers are not well defined. Only slopes from the first and deepest layer can be well determined.
The 1D model assumption can also be verified by comparing the picked dispersion curves from different shot positions. Figure 7.9 shows three picked dispersion curves for Love and Rayleigh waves obtained at different shot positions in line 3. As background images, the phase velocity spectra from shot position 48m and 28m are calculated for the Love and Rayleigh wave case, respectively. The numbers between the brackets incidate the considered offset lengths for which the phase velocity spectra are calculated. Although there are minor differences between the dispersion curves, they are similar and consequently our 1D model assumption is valid.

7.6. Inversion results

Altogether, three main inversion runs with different initial starting values were performed similar as in the synthetic data. Love and Rayleigh wave dispersion curves from three shot positions were inverted for each line. In some cases, the inline and vertical receiver components were separately invoked for the Rayleigh wave inversion. From the extended refraction analysis in section 7.5, we obtained a density and v^P/v^S ratio estimation of each layer.

Table 7.6: Initial parameterization and search space

	run 1	run 2	run 3
Number of layers	2	3	4
Density of each layer [gcm^{-3}]	1.9/2.01	1.9/2.01/2.07	1.9/1.95/2.01/2.07
v^P/v^S for all layers	1.81	1.81	1.81
RA [%]	90	90	90
Number of initial models	125	3125	15625
No. of models for local inversion	30	30	30
Considered frequency steps [Hz]	1	1	1
Considered frequency range [Hz]	1-100	1-70	1-70
v_1^S[ms^{-1}]	100-350	140-200	100-200
v_2^S[ms^{-1}]	300-800	180-300	150-350
v_3^S[ms^{-1}]	–	330-600	200-450
v_4^S[ms^{-1}]	–	–	300-800
d_1 [m]	1-15	1-5	1-10
d_2 [m]	–	5-15	2-10
d_3 [m]	–	–	2-10

Run 1, 2, and 3 deal with a 2-, 3-, and 4-layer model (Table 7.6), respectively. Separate and joint inversion results from the Visp survey are presented now. In each case, one representative line is discussed, albeit we performed inversions for all other lines too.

7.6.1. Separate inversion of Love and Rayleigh waves

A separate Love and Rayleigh wave fundamental mode inversion with search space of run 2 (Table 7.6) is performed. A three layer model is chosen since three layers were identifyable in the first arrival analysis. The results of the picked dispersion curves in Figure 7.9 are shown in Figure 7.10. By plotting these results we tested if our inversion is properly running and if the obtained inversion results agree with the real data.
Figure 7.10a shows that the initiated inversion process properly minimized all three picked dispersion curves since the picked dispersion curve from shot position 48m is well covered by the dispersion curve obtained from the inversion. In contrast, the Rayleigh wave inversion results show in Figure 7.10b a relatively bad fit of the picked dispersion curves. The black picked dispersion curve from shot position 28m is still recognizable. Furthermore, the orange dispersion curve obtained at shot position 8m exhibits a higher phase velocity at around 10Hz in contrast to its picked dispersion curve.

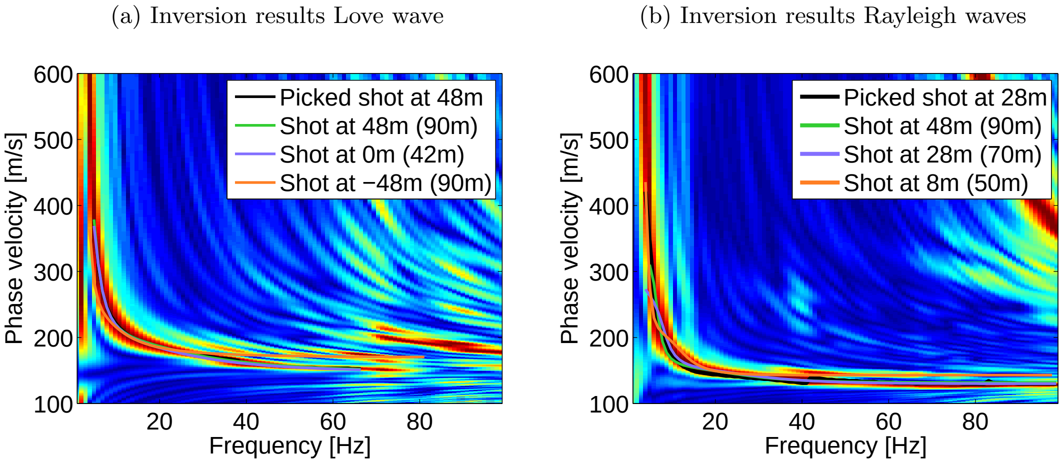
(a) Inversion results Love wave

(b) Inversion results Rayleigh waves

Figure 7.10: The inversion results from the picked dispersion curves in Figure 7.9 are shown here. Love wave inversion results (a) fit better the picked dispersion curves than (b) Rayleigh wave inversion results.

Table 7.7: Fundamental Love and Rayleigh wave inversion of line 3

Inversion	Shot position [m]	$v_1^S[\mathrm{ms}^{-1}]$	$v_2^S[\mathrm{ms}^{-1}]$	$v_3^S[\mathrm{ms}^{-1}]$	d_1[m]	d_2[m]	$C[\mathrm{ms}^{-1}]$
L_0	48	144.5	205.3	508.5	1.5	7.9	1.3
L_0	0	144.3	204.6	476.9	1.6	7.5	0.4
L_0	-48	169.2	251.0	1551.0	4.3	15.4	3.7
R_0	48	142.4	175.8	432.4	2.3	8.5	1.9
R_0	28	140.5	173.9	333.5	2.0	6.5	3.5
R_0	8	154.6	247.2	847.9	4.9	18.6	3.0

Resulting model parameters obtained from the fundamental mode inversion are given in Table 7.7. A glance to the cost-function values already demonstrates that the inversion results with $C \geq 3\text{ms}^{-1}$ are not reliable compared to the other results. The L_0 inversion at -48m cannot be correct since the picked dispersion curve has a velocity jump - see Figure 7.9a. R_0 inversion at 28m and 8m showed a bad fit with the picked dispersion curve shown in Figure 7.9b and 7.10b so that these results are not reliable too. The other inversion results are reliable since they have a relatively low cost-function value and the picked and inverted dispersion curve fit each other. These inversion results show similar velocity and thickness values for at least the first two layers. Inversions of the other survey lines led to similar results as in line 3.

7.6.2. Joint inversion of Love and Rayleigh waves

Joint inversions of Love and Rayleigh waves are more stable than separate inversions. We show joint inversion results representative for line 2. We selected the best L_0R_0 and L_0I_0 results in each case with the lowest cost-function value. Since the number of subsurface layers is not *a priori* known here, models with two, three and four layers were inverted. The search space (starting values) for the two, three, and four layer inversion is given in Table 7.6 under run 1, run 2, and run 3, respectively.

Table 7.8: Joint inversion results of Love and Rayleigh waves for 2, 3 and 4 model layers

Inversion	Layers	$v_1^S[\text{ms}^{-1}]$	$v_2^S[\text{ms}^{-1}]$	$v_3^S[\text{ms}^{-1}]$	$v_4^S[\text{ms}^{-1}]$	d_1[m]	d_2[m]	d_3[m]	$C[\text{ms}^{-1}]$
L_0R_0	2	149.6	149.6	-	-	1.0	-	-	16.7
L_0I_0	2	158.2	158.3	-	-	0.8	-	-	12.2
L_0R_0	3	146.4	211.4	459.3	-	2.7	12.2	-	12.7
L_0I_0	3	149.1	227.3	648.2	-	3.4	16.4	-	12.3
L_0R_0	4	145.7	187.4	281.5	507.4	2.2	6.6	12.3	12.2
L_0I_0	4	170.4	222.8	348.6	892.1	3.3	9.2	16.8	19.6

The inversion results for line 2 are presented in Table 7.8. Letter I stands for inline Rayleigh wave component. Note that these results are from different shot positions and therefore, we cannot exactly expect the same velocities and thicknesses in each inversion, although we assume that our 1D assumption is valid. Mean and standard deviation of the tabulated inversion results are given in Appendix D.

The cost-function is calculated using equation 5.5 whereas the value is dependent on how many frequencies are considered for each picked dispersion curve. We are able to compare the cost-function values because we applied a frequency cut at 70Hz and the starting frequencies are almost the same for all dispersion curves. The cost-functions show that the lowest value of a corresponding layer inversion lie around 12.2-12.3ms^{-1}. No specific layer inversion led to the lowest C-value. The obtained inversion results are illustrated as depth-profiles in Figure 7.11.

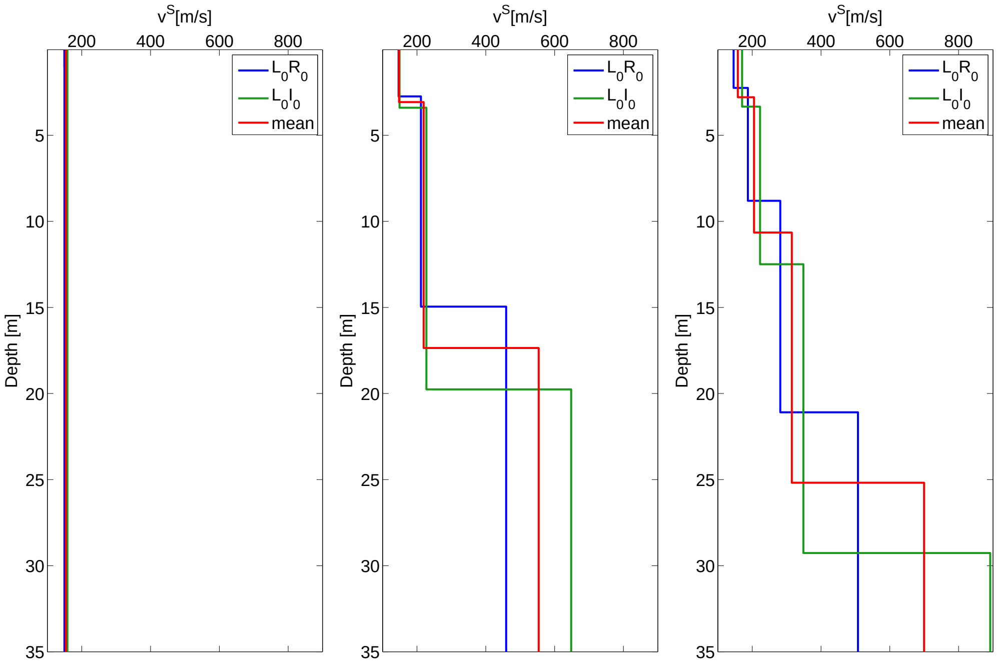

Figure 7.11: Joint Love and Rayleigh wave inversion results plotted as depth-profiles. They are listed in Table 7.8. From left to right: two, three and four layer inversions.

Three inversion results in Table 7.8 are not reliable. The 2-layer inversion results cannot be correct since they propose a model with exactly the same velocities in both layers. Similar to the synthetic case shown in Figure 6.3a and 6.4a only high frequencies fit and return a reliable velocity result for the upper layer. Furthermore, the 4-layer inversion result L_0I_0 is probably not reliable because the cost-function value is relatively high. The 3-layer L_0R_0, L_0I_0 and 4-layer L_0R_0 are the three reliable inversion results, which fit the picked dispersion curves also at low frequencies (e.g. Figure 6.3b and 6.3c), and possess a low C-value (Table 7.8. The uppermost layer(s) could be well resolved with all three reliable inversions with respect to velocity and thickness. Velocities of deeper layers show stronger deviations due to the low sensitivity (low S/N ratio and little wave energy) in this depth.

7.6.3. Joint inversion of surface waves and refracted waves

We performed a joint inversion for line 2 at position 48m including Love, Rayleigh and refracted P- and S-waves. The refraction analysis of P- and S-waves denotes a three layer model and therefore, we initiated a three layer joint inversion. Initial parameterization and search space were defined equal to run 2 in Table 7.6 whereas the results are tabulated in Table 7.9. The bi-objective plot and the final picked result obtained from the Pareto minimization can be seen in Figure 7.12a.

Table 7.9: Joint inversion results of dispersion and refraction information (FA (P)and (S) stands for the result obtained by picking first arrivals from P- and S-wave seismograms)

	v_1^S[ms^{-1}]	v_2^S[ms^{-1}]	v_3^S[ms^{-1}]	d_1[m]	d_2[m]	C^D	C^R
FA (P)	261.6	270.4	414.5	5.2	6.9	-	-
FA (S)	157.4	226.1	270.3	4.8	25.6	-	-
L_0R_0	146.4	211.4	459.3	2.7	12.2	12.7ms^{-1}	
Pareto concept	144.8	227.2	595.6	1.9	16.4	15.3ms^{-1}	20.5ms
ROP	146.1	234.2	604.5	2.2	17.5	49.1[-]	

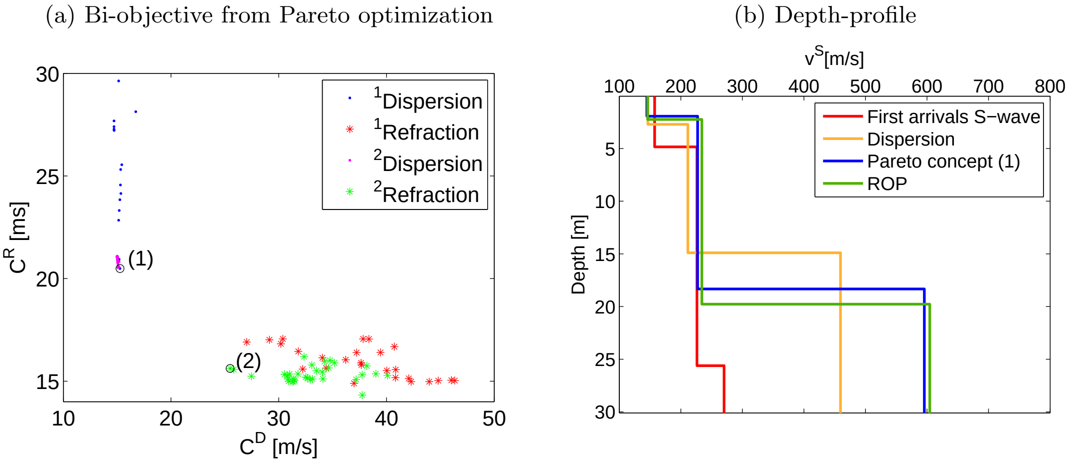
(a) Bi-objective from Pareto optimization

(b) Depth-profile

Figure 7.12: In diagramm (a), misfit values from the minimization via Pareto concept are plotted. The finally picked results are indicated with a small circle. Results obtained from (1) and (2) are listed in Table 7.10. On the left side (b), depth-profiles of the joint and separate L_0R_0 inversion are illustrated as well as the model parameters obtained from the first arrival picking. Corresponding values are listed in Table 7.9.

Table 7.10: The two best results obtained from the Pareto minimization indicated with (1) and (2) in Figure 7.12a

	v_1^S[ms^{-1}]	v_2^S[ms^{-1}]	v_3^S[ms^{-1}]	d_1[m]	d_2[m]	C^D[ms^{-1}]	C^R[ms]
Pareto (1)	144.8	227.2	595.6	1.9	16.4	15.3	20.5
Pareto (2)	150.1	207.0	587.0	1.6	17.0	25.5	15.6

Resulting values with the lowest cost-functions are listed in Table 7.10. To be able to compare between different inversion concepts of the multi-objective problem, results are plotted as depth-profile in Figure 7.12b. The solution of the joint inversion via relative error agrees with the results obtained from the dispersion inversion within the first layer. In the second layer, only the velocity lie in the same range. We know from synthetic data analysis that the 3-layer ROP and Pareto inversion produce very similar results. However, the ROP result were slightly better and therefore, the ROP result is assumed to give here the most reliable estimate of the surface parameters.

7.7. Borehole information and comparison

Hundreds of shallow boreholes (30m) were drilled in the fill of the Rhone valley. In a distance 100m away of our test site, boreholes 721 and 722 are located and marked with yellow stars in Figure 7.2a. Both feature a similar stratigraphic profile. They comprise sequences of gravel, sand, silt and clay components in various fractions. As reference borehole for our geophysical comparison, borehole 722 is selected. A geological description of this core is given in Figure 7.13. The borehole is situated upstream in north-eastern direction with respect to our measurement grid. Since no petrophysical analysis was performed, rock properties of unconsolidated materials are listed from literature in Table 7.11. S-wave velocity ranges for those soil types could not be found.

Table 7.11: Bulk densities of unconsolidated rocks

Soil Type	$^{a)}\rho$[gcm^{-3}]	$^{b)}\rho$[gcm^{-3}]
Poorly graded gravel	1.78-2.09	1.99-2.24
Silty gravel	1.63-2.09	1.99-2.24
Clayey gravel	1.63-2.09	1.99-2.24
Silty sand	1.27-2.14	1.78-2.24
Clayey sand	1.38-2.09	1.78-2.14

---

[a] Density above groundwater table after Coduto (1999)

[b] Density below groundwater table after Coduto (1999)

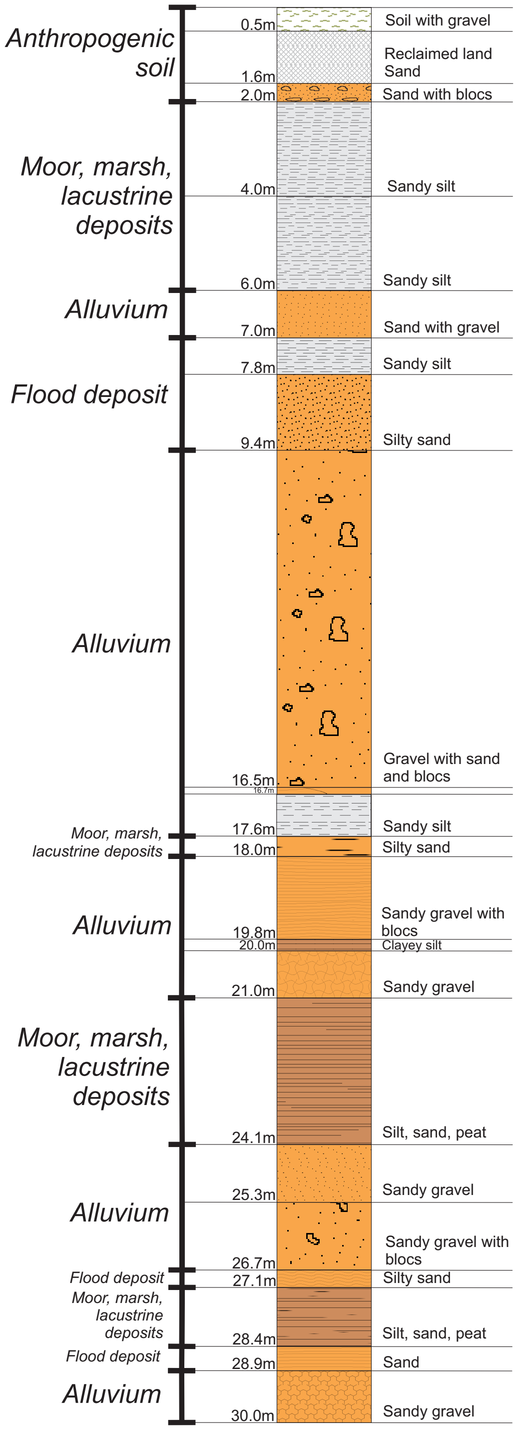

Figure 7.13: Stratigraphic sequence of borehole 722: the interpretation of the deposition environment is given on the left side and their geological description on the right side of the column.

A short comparison is given between the final inversion result (Figure 7.12b) and borehole data (Figure 7.13). Differences in lithology are expected since the discussed survey line 2 and borehole 722 are separated by more than 50m from each other and the geology is probably different. We already observed small variations in terms of velocities and thicknesses between adjacent survey lines. Furthermore, we know that S-waves are only influenced by the grain structure of the materials because they cannot propagate in the pore space. We expect thereby in silty and clayey materials no velocity increase since they contain water. Water is responsible for the plasticity of soft materials like silt and clay. They additionally possess lower bulk densities due to their water content. Sand and gravel comprise bigger pores, but their interface contact is better compared to silt and clay. Hence, the wave energy can pass well through such material. Sand and and gravel usually hold higher velocities compared to soft materials especially if pore spaces of blocks, gravel or sand are filled up with silt, sand or gravel.

Several transition zones were identified in the core - see Figure 7.13. Considering the comments above, our first geophyiscal layer may resolve the transition zone between reclaimed land and sand at 2m depth. The second geophysical layer (Figure 7.12b) shows a velocity increase at 19.7m depth. It probably resolves one of the deeper layers consisting of silt, clay or peat. A more comprehensive interpretation between borehole lithology and our inversion result cannot be made at such a scale, the borehole-profiles are separated and too far away from each other.

P- and S-wave velocities obtained from the refraction analysis were used to estimate bulk densities. With respect to our borehole 722, we expect poorly consolidated sediments with density ranges given in Table 7.11. When comparing these values with the densities obtained by the first arrival analysis (see Table 7.6 run 2), we see that they fit well.

7.8. Discussion

At different shot positions, first arrival curves of P- and S-waves were studied. We obtained layer velocities, which differ from each other less than 10% for various shot positions. Their corresponding layer thicknesses show greater deviations especially the second layer thickness is not well resolved. A comparison between the Poisson values obtained from first breaks with the values from Table 2.1 shows that we deal with a poorly consolidated subsurface. This was confirmed by the borehole analysis.

P-wave velocities and bulk densities of our final model were inferred from the expanded refraction analyses. The 1D model assumption was verified by an extended refraction analysis, comparing first breaks from opposite shot directions and picked dispersion curves from different shot positions. We demonstrated with all three methods that our 1D assumption is appropriate and consequently, dispersion analysis could be carried out.

Joint inversions of Love and Rayleigh waves for various model layers were performed. Three reliable inversion results were obtained with similar properties for the uppermost layer(s) and larger property deviations for deeper layers. Furthermore, three layer joint inversions of surface waves and refracted waves were carried out. According to the synthetic case, the joint inversion result (ROP) is assumed to be most reliable. But note that the Pareto inversion gave very similar results confirming that we have a good representation of the subsurface model. The depth-profile and corresponding values of our final result as well as the mean and standard deviation from the 30 locally minimized models via ROP are summarized and presented in Figure 7.14.

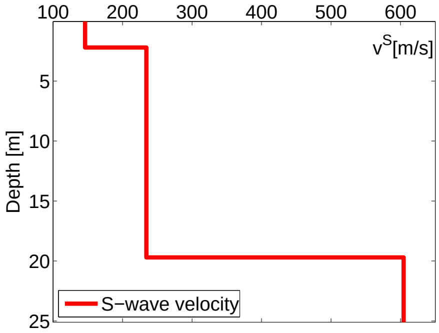

(a) Final depth-profile

(b) Result, error, mean and standard deviation

Layer	$v^S[\mathrm{ms}^{-1}]$	d[m]	$\rho[\mathrm{gcm}^{-3}]$
1 (result)	146	2.2	1.9
2	234	17.5	2.01
3	605	-	2.07
1 (mean±std)	147±1	2.5±0.2	-
2	245±9	12.2±3.8	-
3	488±163	-	-

Figure 7.14: A representative S-wave velocity profile from the test site in Visp is shown in (a) whereas the resulting values as well as the mean and standard deviation (std) of 30 local minimizations via ROP are listed in (b). Note, the velocity values are rounded to integers. The cost-function error of the resulting inversion constitutes 49.1[-].

8. Conclusion and Outlook

We have presented an reliable method for extracting shallow subsurface information by separate and joint inversion of dispersive Love and Rayleigh waves and first breaks of P- and S-waves. Underlying assumption is that we deal with a horizontally layered subsurface.

Analysis of both dispersive surface wave types requested transforming the data from a travel time-distance to phase velocity-frequency domain rendering the picked maxima as dispersion curves. There are different methods to obtain a phase velocity spectrum. We compared a wave field and fk-MUSIC method to construct the dispersion curves. Latter proved to be a method of outstanding resolving power when only a small offset range is considered. In the presence of higher order modes, the wave field transformation produced better defined dispersion curves.

First arrivals of P- and S-waves were picked in the corresponding seismograms. With simple travel time analysis, we obtained velocities and thicknesses of identifiable subsurface layers. The dispersion curves were inverted using a combined global and local optimization algorithm by minimizing the misfit between the picked dispersion curve and synthetically calculated dispersion curves. Global optimization was based on a grid search method of which the search range was estimated using the inversion results of the first arrivals. The separate and joint Rayleigh and Love wave inversions were implemented for two, three and four layer subsurface models. To keep the calculation time limited, only 30 (best-fit) models, obtained from the global minimization, were used as input for the local minimization. In addition, a joint Rayleigh, Love and first arrival P- and S-wave inversion scheme was implemented. Since the cost-functions have different physicals units, a joint inversion via Pareto concept and relative error were performed.

Love wave inversions rendered good estimates of the shallow S-wave velocity values, whereas thicknesses were less well resolved. In contrary, the Rayleigh waves gave good estimates of the shallow layer thicknesses, whereas the S-wave velocity values were less well reconstructed.

Consequently, combined Rayleigh and Love wave inversions were able to reconstruct shallow layer thicknesses and the shallow S-wave velocities values well. However, the deep layer parameters could not be well reconstructed, which was probably due to the limited penetration depth of the Rayleigh and Love waves.

Refracted wave inversions showed good results for the deep layer parameters, whereas the shallow layer parameters could not be well reconstructed. Limitation of the joint Love, Rayleigh and first break P- and S-wave inversion is that we cannot calculate models with velocity reversals due to the refraction assumption of increasing velocity with depth. Therefore, we always suggest to do separate inversion of Love and Rayleigh waves beside the joint surface and refraction wave inversion.

A field survey was carried out in the Rhone valley plane, Switzerland, to test the applicability of our method. Altogether, data were collected for six lines, each 95 meter long. Acquisition of Love and Rayleigh wave data requested the use of three component geophones and special sources. We showed that our three different sources were suitable for horizontal and vertical wave excitation using the sledge hammer method. First arrivals from various shot positions were investigated. On the basis of these results, we could validate our assumption of lateral homogeneous medium for three shallow layers. The same verification of this assumption was made by comparing dispersion curves in the phase velocity spectra at different shot positions and integrating different offset ranges. Similar results were obtained as in the refraction analysis. On the basis of this result, we could finally perform joint inversions. The inversion results showed that our investigated survey area comprises material with extremely low S-wave velocities from ~150-800m/s down to a depth level of 20m. Poisson ratios close to zero were calculated what implies, that the subsurface material is poorly consolidated.

We conclude that a combination of surface and refracted waves in a joint inversion scheme yields to optimal results, since we benefit from both methods. The applied Pareto and relative objective scheme produced very similar results. Finally, subsurface properties could be resolved, in particular Poisson ratios, a density guess, P- and S-wave velocities, and the thicknesses of the subsurface layers.

8.1. Future developments and applications

From the implementational aspect, future developments can be done since the full potential of our inversion algorithms is still not achieved. Instead of our proposed frequency reduction strategy, a variable frequency sampling can be employed to respect the important dispersion information at low frequencies in the phase velocity spectra. Further, both dispersion and refraction cost-functions comprise weighting factors to account for data resolution. In particular, a first arrival weighting factor has not been presented. Finally, a faster forward modeling algorithm for surface waves has to be used to be able to invert for more than four layers with a grid search inversion scheme. So far, our method includes refraction and dispersion information, but also a joint inversion of refraction, reflection and dispersion information can be carried out in future applications, if reflections can be observed. However, we propose as next step a full-waveform inversion of surface waves. Our method will then provide an accurate starting model, which is essential in full-waveform inversions.

For lateral varying media, further studies at test sites with laterally varying geology will help to define the application limit of the method. Since we can calculate well resolved phase velocity spectra with the fk-MUSIC method using a few traces, we expect, that we can also identify lateral heterogeneity with the surface wave method. A dataset in such an area has already been collected and the results will be processed soon.

Bibliography

Abramowitz, M., & Stegun, I. A. (1965). *Handbook of Mathematical Functions with Formulas, Graphs, and Mathematical Table* (M. Abramowitz & I. A. Stegun, Eds.). Washington D.C.: Dover Publications Inc.

Aki, K., & Richards, P. G. (2002). *Quantitative Seismology* (Second ed.; J. Ellis, Ed.). New York: University Science Books.

Barnola, A., & White, R. (2001). Gardner's relations and AVO inversion. *first break*, *19*, 607-611.

Bates, C., & Phillips, D. (2000). Multi-component seismic surveying for near surface investigations:examples from central Wyoming and southern England. *Journal of Applied Geophysics*, *44*, 257-273.

Ben-Menahem, A., & Singh, S. J. (1981). *Seismic waves and sources.* New York: Springer Verlag New York Inc.

Bodin, T., & Maupin, V. (2008). Resolution potential of surface wave phase velocity measurements at small arrays. *Geopyhsical Journal International*, *172*, 698-706.

Bolt, B. (1982). *Inside the Earth* (B. A. Bolt, Ed.). San Francisco: W.H. Freeman.

Brocher, T. M. (2005). Empirical Relations between Elastic Wavespeeds and Density in the Earth's Crust. *Bulletin of the Seismological Society of America*, *95*, 2081-2092.

Butler. (2005). *Near-Surface Geophysics* (D. K. Butler, Ed.). Tulsa OK: Society of Exploration Geophysicists.

Coduto, D. P. (1999). *Geotechnical engineering: principles and practices* (M. Horton, Ed.). Prentice-Hall International London: Abt, Alan.

Dal Moro, G., Forte, E., Pipan, M., & M., S. (2006). Velocity spectra and seismic-signal identification for surface-wave analysis. *Near Surface Geophysics*, *4*, 243-251.

Dal Moro, G., & Pipan, M. (2007a). Joint inversion of surface wave dispersion curves and reflection travel times via multi-objective evolutionary algorithm. *Journal of Applied Geophysics*, *61*, 56-81.

Dal Moro, G., & Pipan, M. (2007b). Vs and Vp determination via joint inversion of Rayleigh waves and refraction travel times by means of Pareto criterion and evolutionary algorithms. *GNGTS*, *Sessione 3.2*, 508-510.

Dal Moro, G., Pipan, M., & Gabrielli, P. (2007). Rayleigh wave dispersion curve inversion via genetic algorithms and Marginal Posterior Probaility Density estimation. *Journal of Applied Geophysics*, *61*, 39-55.

Domenico, S. (1977). Elastic properties of unconsolidated porous sand reservoirs. *GEOPHYSICS*, *42*, 1339-1368.

Drijkoningen, G. G. (2004, September). *Introduction to Reflection Seismology.* TU Delft. (TA3520)

Ewing, M., Jardetzky, W., & Press, F. (1957). *Elastic waves in layered media.* New York: McGraw-Hill Book Company, Inc.

Faeh, D., Kind, F., & Giardini, D. (2001). A theoretical investiation of average H/V ratios. *Geophysical Journal International*, *145*, 535-549.

Faeh, D., Stamm, G., & Havenith, H.-B. (2008). Analysis of three-component ambient vibration array measurements. *Geophysical Journal International*, *172*, 199-213.

Forbriger, T. (2001). *Inversion flachseismischer Wellenfeldspektren.* Unpublished doctoral dissertation, Institut für Geophysik der Universität Stuttgart.

Forbriger, T., & Friederich, W. (2005). A propsal for a consistent parameterization of earth models. *Geophysical Journal International*, *162*, 425-430.

Foti, S., Sambuelli, L., Socco, V., & Strobbia, C. (2003). Experiments of joint acquisition of seismic refraction and surface wave data. *Near Surface Geophysics*, *1*, 119-129.

Friederich, W., & Dalkolmo, J. (1995). Complete synthetic seismograms for a spherically symmetric earth by a numerical computation of the Green's function in the frequency domain. *Geophysical Journal International*, *122*, 537-550.

Gabriels, P., Snieder, R., & Nolet, G. (1987). In situ measurements of shear-wave elocity in sediments with higher-mode Rayleigh waves. *Geophysical Prospecting*, *35*, 187-196.

Gardner, G., Gardner, L., & Gregory, A. (1974). Formation velocity and density - the diagnostic basics for stratigraphic traps. *GEOPHYSICS*, *39*, 770-780.

Ghose, R., & Slob, E. (2006). Quantitative integration of seismic and GPR reflections to derive unique estimates for water saturation and porosity in subsoil. *Geophysical Research Letter*, *33*, L05404.

Giardini, D. (2006). *Seismologie.* (Vorlesungsskript WS05-06)

Grandjean, G. (2006). A seismic multi-approach method for characterizing contaminated sites. *Journal of Applied Geophysics*, *58*, 87-98.

Halliday, D., Curtis, A., & Kragh, E. (2008). Seismic surface waves in a suburban environment: Active and passive interferometric methods. *The Leading Edge*, *27*, 210-218.

Iranpour, K., Muyzert, E., & Grion, S. (2002). Local velocity analysis by parametric wavenumber estimation in seismic (fk-MUSIC). In *EAGE 64th Conference in Florence, Italy.* Florence: EAGE 64th Conference and Exhibition.

Ivanov, J., Park, C., Miller, R., & Xia, J. (2000a). Joint analysis of surface-wave and refraction events from river-bottom sediments. *SEG*, *70th Ann. Meeting*, Expanded Abstracts.

Ivanov, J., Park, C., Miller, R., & Xia, J. (2000b). Mapping Poisson's ratio of unconsolidated materials from a joint analysis of surface-wave and refraction events. *SAGEEP*, *February 20-24*, 11-19.

Johnston, D., Toksöz, M., & Timur, A. (1979). Attenuation of seismic waves in dry and saturated rocks: 2. Mechanisms. *GEOPHYSICS*, *44*(4), 691-711.

Kearey, P., Brooks, M., & Hill, I. (2002). *An Introduction to Geophysical Exploration* (Third ed.). Oxford: Blackwell Publishing.

Kirsch, R., & Rabbel, W. (1997). Seismische Verfahren in der Umweltgeophysik. In K. K. (Ed.), (3rd ed., p. 251-265). Berlin/ Heidelberg: Springer.

Knoedel, K., Lange, G., & Voigt, H.-J. (2007). *Environmental geology. Handbook of Field Methods and Case Studies.* Berlin: Springer.

Lagarias, J., Reeds, J. A., Wright, M., & Wright, P. (1997). Convergence properties of the Nelder-Mead simplex method in low dimensions. *Society for Industrial and Applied Mathematics*, *9*(1), 112-147.

Lai, C., & Rix, G. (1998). *Simultaneous Inversion of Rayleigh Phase Velocity and Attenuation for Near-Surface Site Characterization.* Unpublished doctoral dissertation, Georgia Institute of Technology.

Lanz, E., Maurer, H., & Green, A. (1998). Refraction tomography over a buried waste disposal site. *GEOPHYSICS*, *63*(4), 1414-1433.

Lanz, E., Pugin, A., Green, A., & Horstmeyer, H. (1996). Results of 2- and 3-D high-resolution seismic reflection surveying of surficial sediments. *Geopyhsical Research Letters*, *23*(5), 491-494.

Latzel, S. (2004). *Modellierung vollständiger Seismogramme in der Flachseismik.* Unpublished master's thesis, Universität Stuttgart.

Lewis, R., Torczon, V., & Trosset, M. (2000). Direct Search Methods: Then and now. *Langley Research Center*, *2000-26*, 1-16.

Lowrie, W. (1997). *Fundamentals of geophysics.* Cambridge: Cambridge University Press.

Manificat, G., & Guéguen, Y. (1998). What does control Vp/Vs in granular rocks? *Geophysical Research Letters*, *25*(3), 381-384.

McMechan, G., & Yedlin, M. (1981). Analysis of dispersive waves by wave field transformation. *GEOPHYSICS*, *46*(6), 869-874.

Menke, W. (1989). *Geophysical Data Analysis: Discrete Inversion Theory* (Revised ed., Vol. 45). London: Academic Press: International Geophysics Series.

O'Neill A., M. T. (2005). Higher Surface-wave Modes and Possible Inversion Pitfalls. *JEEG*, *10*(2), 185-201.

Park, C., Miller, R., & Xia, J. (1998). Imaging dispersion curves of surface waves on multi-channel record. *SEG*, *Expanded Abstracts*, 1-4.

Robertsson, J., Holliger, K., & Green, A. (1996). Source-generated noise in shallow seismic data. *European Journal of Environmental and Engineering Geophysics*, *1*, 107-124.

Robertsson, J., Holliger, K., Green, A., Pugin, A., & Iaco, R. de. (1996). Effects of near-surfae waveguides on shallow high-resolution seismic refraction and reflection. *Geophysical Research Letters*, *23*, 495-498.

Roten, D. (2007). *Site effects in the Rhone valley analysed by ambient noise, weak motion records and numerical simulations.* Unpublished doctoral dissertation, Swiss Federal Institute of Technology.

Roth, M., & Holliger, K. (1999). Inversion of source-generated noise in high-resolution seismic data. *The Leading Edge*, *December*, 1402-1406.

Roth, M., Holliger, K., & Green, A. (1998). Guided waves in near-surface seismic surveys. *Geophysical Research Letters*, *25*(7), 1071-1074.

Safani, J., O'Neill, A., Matsuoka, T., & Sanada, Y. (2005). Applications of Love wave dispersion for improved shear-wave velocity imaging. *JEEG*, *10*(2), 135-150.

Sheriff, R. (1999). *Encyclopedic dictionary of exploration geophysics.* New Brunswik: Society of Exploration Geophysicists.

Shillington, D., Minshull, T., Peirce, C., & O'Sullivan, J. (2008). P- and S-wave velocities of consolidated sediments from a seafloor seismic survey in the North Celtic Sea Basin, offshore Ireland. *Geophysical Prospecting*, *56*, 197-211.

Sigrist, M. (2005). *Kontinuumsmechanik.* (ETH Zurich)

Snieder, R. (1994). *A guided tour of mathematical physics.* Utrecht: Samizdat Press.

Socco, L., & Boiero, D. (2008). Improved Monte Carlo inversion of surface wave data. *Geophysical Prospecting*, *56*, 357-371.

Socco, L., & Strobbia, C. (2004). Surface-wave method for near-surface characterization a tutorial. *Near Surface Geophysics*, *2*, 165-185.

Song, X., Gu, H., Liu, J., & Zhang, X. (2007). Estimation of shallow subsurface shear-wave velocity by inverting fundamental and higher-mode Rayleigh waves. *Soil Dynamics and Earthquake Engineering*, *27*, 599-607.

Stokoe, K., Wright, S., Bay, J., & Roesset, J. (1994). Characterization of geotechnical sites by SASW method. In R. D. Woods (Ed.), (p. 15-27). New Delhi: A.A.Balkema Rotterdam.

Strobbia, C. (2002). *Surface Wave Methods.* Unpublished doctoral dissertation, Politecnico di Torino.

Strobbia, C., & Cassiani, G. (2007). Multilayer ground-penetrating radar of guided waves in shallow soil layers for estimating soil water content. *GEOPHYSICS*, *72*(4), J17-J29.

Tarantola, A. (2005). *Inverse Problem Theory and Methods for Model Parameter Estimation.* Philadelphia: SIAM.

Telford, W., Gedart, L., & Sheriff, R. (2004). *Applied geophysics* (Second ed.). New Brunswik: Cambridge University Press.

van der Kruk, J. (2006). Properties of Surface Waveguides Derived From Inversion of Fundamental and Higher Mode Dispersive GPR Data. *IEEE Transactions on geoscience and remote sensing*, *44*(10), 2908-2915.

van der Kruk, J., Arcone, S. A., & Liu, L. (2007). Fundamental and Higher Mode Inversion of Dispersed GPR Waves Propagating in an Ice Layer. *IEEE Transactions on geoscience and remote sensing*, *45*(8), 2483-2491.

van der Kruk, J., Streich, R., & Green, A. (2006). Properties of surface waveguides derived from separate and joint inversion of dispersive TE and TM GPR data. *GEOPHYSICS*, *71*(1), K19-K29.

van Veldhuizen, D. A., & Lamont, G. B. (2000). Multiobjective Evolutionary Algorithms: Analyzing the State-of-the-Art. *Evolutionary Computation 8*, *2*, 125-147.

Wapenaar, C., & Berkhout, A. (1989). *Elastic wave field extrapolation.* Amsterdam: Elsevier Science.

Werthmüller, D. (2007). *Separate and joint inversion of dispersive Rayleigh and Love waves.* (Bachelor Thesis)

Winsborrow, G., Huws, D., & Muyzert, E. (2003). Acquisition and inversion of Love wave data to measure the lateral variability of geo-acoustic properties of marine sediments. *Journal of Applied Geophysics*, *54*, 71-84.

Wood, R. (1968, July). Screening of surface waves in soils. *Journal of the soil mechanics and foundations division*, *SM4*, 951-979. (Proceedings of the American Society of Civil Engineers)

Xia, J., Chen, C., Tian, G., Miller, R., & Ivanov, J. (2005). Resolution of High-frequency Rayleigh-wave Data. *JEEG*, *10*(2), 99-110.

Xia, J., Miller, R., Park, C., & Tian, G. (2002). Determining Q of near-surface materials from Rayleigh waves. *Journal of Applied Geophysics*, *51*, 121-129.

Xia J., P. C., Miller R.D. (1999). Estimation of near-surface shear-wave velocity by inversion of Rayleigh waves. *GEOPHYSICS*, *64*(3), 691-700.

Yilmaz, O. (2001). *Seismic data analysis.* Tulsa OK: Societiy of Exploration Geophysicists.

Acknowledgment

Foremost, I would like to thank Jan van der Kruk for suggesting me this topic, his great technical and mental support and invested time. He guided and motivated me through the entire work with extraordinary enthusiasm. I hope, I will have in future the same energy and enthusiasm as he showed to me. Furthermore, I appreaciated his help to structure my future plans.

Thanks to Sabine Latzel for her help and appreciated advices. Solving all the small difficulties without her experience would have claimed more time. I am grateful to Alain, Caroline, Jan and Sabine for carefully acquire the dataset over three cold days. I also got the chance to lead a three component seismic survey in St.Nikolaus, Switzerland. Jan and Tobias were kindly to help me with preparation and data acquisition. I wish to further express my thanks to Heinrich Horstmeyer for helping me in technical matters no matter what time of day and both co-examiners for their constructive comments.

This work would never have the same practical relevance without mention the Swiss Seismological Service. I thank Donat Fäh, Valerio Poggi and Gabriela Stamm from the seismological group for discussions and suggestions.

Thanks to Oliver and Fabian for the time we spent together the last half a year. They inspired me day-to-day and let me know that there is also another life beside working. I further allude the creative ambiance of my office: turbulent, ingenuous but also constructive and helpful. My fellows Giovanni, Stefano, Edgar, Alain, Mark and Sabine always supported me if desired. Since this thesis completes the first two year joint master program, I also thank my five fellow students for the memories we share and I cherish. Lastly, I would like to express my thank to my parents for their support and advices especially for making difficult decisions.

Glossary

C	Cost-function. 32
C_{ijkl}	Elastic moduli tensor. 86
E	Young's modulus. 8
F^B	Body force. 85
F^E	Force. 7
F^S	Stress tensor equal to $\boldsymbol{\sigma}$. 85
G	Function in the space-frequency domain. 6
K	Bulk modulus. 8
L	Abbreviation for Love wave. 32
M^P	Number of models. 31
N^F	Number of frequencies. 33
N^L	Number of layers. 32
N^M	Number of modes. 32
N^O	Number of observations. 31
N^R	Number of receivers. 26
N^S	Number of signals. 27
N^T	Number of traces. 32
P^S	Phase velocity spectrum. 25
P^W	Power spectra. 26
Q	Quality factor. 9, 10
Q^K	Quality factor bulk modulus. 10
Q^P	Quality factor compressional wave. 10
Q^S	Quality factor shear wave. 10
Q^μ	Quality factor shear modulus. 10
R	Abbreviation for Rayleigh wave. 32
V^E	Volume. 7
Θ^C	Critical incident angle. 12
α	Attentuation factor. 9
$\boldsymbol{\sigma}$	Stress matrix. 7
δ_{ij}	Kronecker delta or unit tensor. 87
λ	Lamé constant. 8
λ^E	Eigenvalues. 26
λ^L	Wavelength. 15, 23
μ	Shear modulus and Lamé constant. 8, 20
ν	Poisson's ratio. 10
ω	Angular frequency. 6, 20, 22

ρ	Density. 7, 20
$\mathbf{A}$	Matrix including Lamé parameters. 88
$\mathbf{R}$	Correlation matrix. 26
$\mathbf{d}$	Data vector. 31
$\mathbf{e}^S$	Steering vector. 26
$\mathbf{m}$	Model parameter vector. 31
$\mathbf{v}^E$	Eigenvector. 26
$\mathbf{w}$	Weighting factor. 26
θ	Phase-shift. 25
$\tilde{D}$	Dispersion term. 26
$\tilde{G}$	Function in wavenumber-frequency domain. 6
$\tilde{R}^E$	Displacement eigenfunctions. 88
$\tilde{S}$	Source excitation term. 26
a^C	Accelaration. 7
c	Phase velocity. 15, 18
d	Layer thickness or interface depth between two media. 12, 20
d^G	Downgoing wave. 20
e_3	Unit vector in depth direction. 87
g	Function in the space-time domain. 6
k	Wavenumber. 6, 20
m	Mass. 7
m^L	Linear momentum. 85
n_i	Normal vector. 87
p	Acoustic pressure field. 18
r^D	Radial distance. 17
s_i	Slowness vector. 18
t^R	Trace. 32
u^G	Upgoing wave. 20
u_i	Displacement vector. 19
v	Velocity in a media. 7
v^G	Group velocity. 15
v^P	Compressional wave velocity. 8
v^S	Shear wave velocity. 9, 20, 22
w^D	Dispersion objective weighting factor. 34
w^{Fs}	Wave field, where a slant stack is applied. 26
w^F	Wave field in the space-time domain. 25
w^R	Refraction objective weighting factor. 34
z_i	Displacement amplitude vector. 19, 20

List of Figures

1.1. Earthquake wave propagates from high to low velocity medium 1
1.2. Narrow optimum reflection window 2

2.1. Overview about the important seismic wave paths 12
2.2. Refracted waves: travel time vs distance curves 13
2.3. Difference between group and phase velocity 15
2.4. Surface waves: geometric dispersion 16

3.1. Particle motion of a Love wave 17
3.2. Simplest medium in which Love waves can be generated 20
3.3. Most simple solution of the Love wave dispersion equation 22
3.4. Particle motion of a Rayleigh wave 23

4.1. Comparison between wave field and fk-MUSIC method considering long offsets 28
4.2. Comparison between wave field and fk-MUSIC method considering short offsets 29
4.3. Analysis of picked dispersion curves integrating five traces 29
4.4. Analysis of picked dispersion curves integrating various number of traces . 30

5.1. Inversion of surface waves 31
5.2. Pareto front of a bi-objective problem 33
5.3. Flowchart to separately and jointly invert first arrival and dispersion information 37

6.1. Synthetic Love and Rayleigh wave seismogram 40
6.2. Frequency spectra and picked dispersion curve of a Rayleigh wave 41
6.3. Inversion results compared as dispersion curves with underlying phase velocity spectra 42
6.4. Underlying three layer model inverted with two, three and four layers . . 43
6.5. Influence of frequency reduction on the shape of dispersion curves 44
6.6. Depth-profiles based on inversion results with different search spaces . . . 46
6.7. Joint inversion of synthetic surface and refracted waves 47

7.1. Applied sources in the field survey 52
7.2. Location and measurement grid 53
7.3. Source polarity check of the iron triangle source 55
7.4. P- and S-wave seismograms showing the picked first breaks 56

7.5. Source comparison 56
7.6. Seismogram and the corresponding phase velocity spectra 57
7.7. Expanded refraction analysis done in line 3 58
7.8. 1D assumption verfication with first breaks 59
7.9. Comparison of fundamental mode dispersion curves 59
7.10. Resulting fundamental mode dispersion curves from inversion 61
7.11. Depth-profiles of the joint Love and Rayleigh inversions 63
7.12. Bi-objective plot and depth-profiles from the joint surface and refracted wave inversion 64
7.13. Stratigraphic description of borehole 722 66
7.14. Final interpreted results of the Visp survey 68

B.1. Inversion results, obtained from the model given in Table B.2, are plotted in a depth-profile. 92

List of Tables

2.1. Poisson ratios of various rocks 11

6.1. Synthetic models 39
6.2. Search space for 2-, 3- and 4-layer models 41
6.3. Selected joint Love and Rayleigh wave inversion results for 2-, 3- and 4-layer model 42
6.4. Broad search space of a three layer inversion 44
6.5. Selected results from inversion with various frequency sampling 45
6.6. Narrow, wide and wrong search space parameters 46
6.7. Joint refraction and surface wave inversion results 48
6.8. Results of different inversion approaches 49

7.1. Aquisition parameters of the field survey 52
7.2. Source availability: considered lines for the analyses 53
7.3. Model parameters from line 3 obtained by refraction analysis 54
7.4. Mean and standard deviation of the P-wave shotanalysis in line 3 57
7.5. Model parameters from line 6 obtained by refraction analysis 58
7.6. Inversion parameters and search space 60
7.7. Results of the fundamental Love and Rayleigh inversion 61
7.8. Results of a 2, 3 and 4 layer joint inversion 62
7.9. Joint refraction and surface wave inversion results from Visp 64
7.10. Two best results from joint Pareto inversion 65
7.11. Bulk densities of unconsolidated rocks 65

B.1. Model parameters 91
B.2. Search space 91

D.1. Statistical evaluation of the joint Love and Rayleigh wave inversion 95

A. Rayleigh wave dispersion equation

Rayleigh waves show dispersive characteristics in layered media. We derive in this section Rayleigh wave dispersion and phase velocity equations mainly after Ben-Menahem and Singh (1981) and Lai and Rix (1998). Through the entire derivation, we assume that there is no change of mass over time.

If we change from Lagrangian to Eulerian point of view, the partial to total time derivative relation is used

$$\frac{d}{dt} = \frac{\partial}{\partial t} + (v_i \partial_i). \tag{A.1}$$

We may write the conservation law of mass in terms of

$$0 = \frac{dm}{dt} = \frac{d}{dt}\int_{V^E} \rho dV^E = \int_{V^E} \left[\frac{d\rho}{dt} + \rho \partial_i v_i\right] dV^E = \int_{V^E} \left[\frac{\partial \rho}{\partial t} + \partial_i(\rho v_i)\right] dV^E, \tag{A.2}$$

where v_i describes the velocity field and $m = V^E \rho$ is mass. This equation has to be valid for arbitrary volumes at each point, which leads to the continuity equation (Snieder, 1994)

$$0 = \frac{d\rho}{dt} + \rho \partial_i v_i, \tag{A.3}$$

$$0 = \frac{\partial \rho}{\partial t} + \partial_i(\rho v_i). \tag{A.4}$$

In the next step, the conservation law of linear momentum ρv_i is derived - see section 2.4.1. The total linear momentum of a body can be expressed as $m^L{}_i(t) = \int_{V^E} v_i \rho dV^E$. Starting point of view is again the Lagrangian relation (A.3) between partial and total derivative. The linear momentum of an arbitrary volume reads

$$\frac{d}{dt} m_i^L = \frac{d}{dt}\int_{V^E} \rho v_i dV^E = \int_{V^E} \left[\frac{d(\rho v_i)}{dt} + \rho v_i \partial_j v_j\right] dV^E. \tag{A.5}$$

It can be rewritten by applying the product rule, or Leibniz's law, and considering equation (A.3). We obtain

$$\int_{V^E} \left[\frac{d(\rho v_i)}{dt} + \rho v_i \partial_j v_j\right] dV^E = \int_{V^E} \left[\rho \frac{dv_i}{dt} + v_i \left(\frac{d\rho}{dt} + \rho \partial_j v_j\right)\right] dV^E = \int_{V^E} \rho \frac{dv_i}{dt} dV^E. \tag{A.6}$$

A force that acts on a mass can be split up in body forces $\rho F^B{}_i$ and surface forces $n_i F_i^S$, where F_i^B represents the body force per unit mass, n_i indicates the normal vector and F^S the stress tensor. We do not introduce here sigma as stress tensor because we consider forces. Therefore, it is assigned to another variable. The linear momentum can then be written in terms of forces

$$\frac{d}{dt}m_i^L = \oint_S (F_i^S dS_i) + \int_{V^E} \rho F_i^B dV^E = \int_{V^E} (\partial_i F_i^S + \rho F_i^B) dV^E, \tag{A.7}$$

where we applied the theorem of Gauss. From equation A.6 and A.7, we get the Euler's equation of motion in terms of forces acting on an arbitrary volume

$$\partial_i F_i^S + \rho F_i^B = \rho \frac{dv_i}{dt} dV^E. \tag{A.8}$$

To accomplish an explicit expression for the velocity field v_i in terms of displacements, the continuity equation A.3 is used. The assumption is introduced that spatial displacements changes $\partial_i u_j$ are small, the velocity field v_i reads

$$v_i = \frac{du_i}{dt} = \frac{\partial u_i}{\partial t} + v_i \partial_i u_j \simeq \frac{\partial u_i}{\partial t}, \tag{A.9}$$

$$\frac{dv_i}{dt} = \frac{\partial v_i}{dt} + v_i \partial_i v_j \simeq \frac{\partial^2 u_i}{\partial t^2}. \tag{A.10}$$

Under these assumptions, Euler's equation of motion (A.8) simplifies to the Cauchy's equation of motion

$$\partial_i F_i^S + \rho F_i^B = \rho \frac{\partial^2 u_i}{\partial t^2}. \tag{A.11}$$

As we know from mechanics, a volume increase per unit volume can be described as $\frac{dV^{E'} - dV^E}{dV^E} = \partial_i u_j$ where $V^{E'}$ indicates the end volume. Change of density in that body is inversely proportional to volume and leads to (Ben-Menahem & Singh, 1981)

$$\frac{\rho' - \rho}{\rho} = -\frac{\partial u_j}{\partial x_i} = -\partial_i u_j. \tag{A.12}$$

Furthermore, we need the generalized Hook's law, which describes the stress-strain relation in an ideal elastic solid. Without deriving Hook's law in detail, the stress components can be expressed in subscript notation as

$$\sigma_{ij} = C_{ijkl} \epsilon_{kl}, \tag{A.13}$$

where C_{ijkl} indicates the tensor of elastic moduli and ϵ_{kl} describes the strain components. We know that each point is represented by six components of stress. In general, each of these stress components are related to the three strain components. C_{ijkl} becomes a 36 element matrix. In isotropic elastic medium (Ewing et al., 1957), the number of elements reduces to 21. Since we have the symmetry $C_{ijkl} = C_{klij}$, $C_{ijkl} = C_{jikl} = C_{ijlk}$, we obtain $\sigma_{ij} = \sigma_{ji}$ and $\epsilon_{kl} = \epsilon_{lk}$ (Ben-Menahem & Singh, 1981) and all remaining components can be expressed with Lamé parameters. We finally find the well known expression

$$\sigma_{ij} = \lambda\delta_{ij}\epsilon_{kk} + 2\mu\epsilon_{ij} = \lambda\delta_{ij}\frac{\partial u_k}{\partial x_k} + \left(\frac{\partial u_j}{\partial x_i} + \frac{\partial u_i}{\partial x_j}\right). \tag{A.14}$$

We reformulate this equation (A.14) in terms of a surface force acting on a mass since $F^S{=}\sigma_{ij}$ and following

$$F_i^S = \lambda\delta_{ij}\partial_k u_k + \mu(\partial_i u_j + \partial_j u_i), \tag{A.15}$$

where δ_{ij} indicates the unit tensor or Kronecker delta. So far, we derived an expression known as Hook's law. For efficiently writing cross products in subscript notation, the $Levi - Civit\grave{a}$ tensor is introduced and defined as

$$\epsilon_{ijk} = \begin{cases} +1, & \text{if (ijk) is an even permutation of (123)} \\ -1, & \text{if (ijk) is an odd permutation of (123)} \\ 0, & \text{otherwise} \end{cases}. \tag{A.16}$$

A vector product can then be written for example as $(\mathbf{a} \times \mathbf{b})_i = \sum_{j=1}^3 \sum_{k=1}^3 \epsilon_{ijk} a_j b_k = \epsilon_{ijk} a_j b_k$. We substitute equation A.15 in equation A.11. First, we write the first term on the left-hand side

$$\partial_i F_i^S = \partial_i \left[\lambda\delta_{ij}\partial_j u_j + \mu(\partial_i u_j + \partial_j u_i)\right]. \tag{A.17}$$

We further express

$$n_j(\partial_i u_j + u_j\partial_i) = n_i(2\partial_i u_j + \epsilon_{ijk}\partial_j u_k \epsilon_{kml}\delta_{ml}) = 2\frac{\partial u_i}{\partial N^M} + \epsilon_{ijm} n_j(\epsilon_{mkl}\partial_k u_l), \tag{A.18}$$

where n_i is the normal vector, N^M is the radial mode number and the curl of a vector field is defined as $\epsilon_{ijk}\partial_j u_k = curl\ \mathbf{u} = \nabla \times \mathbf{u}$. Replace this expression in equation A.17 and further set the expression $\partial_j F_j^S = \nabla \cdot \mathbf{F}^S$ into Cauchy's equation of motion (A.11). Resulting equation is known as Cauchy-Navier equation of motion. For vertically heterogeneous media, where the Lamé parameters and density are only depth dependent, we read

$$\mu\partial_i\partial_i u_j + (\lambda+\mu)\partial_i\partial_i u_i + e_3\partial_3\lambda\partial_j u_j + \partial_3\mu(2\partial_3 u_i + \epsilon_{i3m}e_3(\epsilon_{mkl}\partial_k u_l) + \rho F_i^B = \rho\partial_t^2 u_i, \tag{A.19}$$

where e_3 is the unit vector along the x_3-coordinate. The Cauchy-Navier equation of motion is our starting point to derive the dispersion equation of Rayleigh waves (Lai & Rix, 1998). A solution can be found by considering plane wave displacement fields. Each component of the displacement with depth dependent parameters can be formulated as

$$u_1 = \tilde{R}_1^E(k(\omega), \omega, x_3)e^{i(\omega t - kx_\alpha)} \tag{A.20a}$$

$$u_2 = 0 \tag{A.20b}$$

$$u_3 = i\tilde{R}_2^E(k(\omega), \omega, x_3)e^{i(\omega t - kx_\alpha)}, \tag{A.20c}$$

where $\tilde{R}^E$ denotes displacement eigenfunctions and x_α is the direction of propagation. The imaginary part $i = \sqrt{-1}$ indicates a phase-shift of 90°. Similar as in the Love wave derivation, we involve three boundary conditions. There is no traction at the free surface, no stress at infinity and the equation of motion (see equation A.8) must be valid over each interface. First boundary condition at the free surface $x_3 = 0$ leads to

$$\frac{\partial u_i}{\partial x_3} = 0, \tag{A.21a}$$

$$\sigma_{i3} = 0. \tag{A.21b}$$

σ_{ij} is the Cauchy's stress tensor. Note that the horizontal transverse displacement component u_2 is zero. The radiation condition, which states that there is no stress at infinity, reads

$$u_i \rightarrow 0, \tag{A.22a}$$

$$\sigma_i \rightarrow 0. \tag{A.22b}$$

Third condition says that continuity of displacement and traction must hold over an interface. Hence, displacements and stresses slight above and below an interface have to be the same.

Now, we construct the solution. Equation A.20 can be substituted into the Cauchy-Navier equation A.19. To simplify the representation we rewrite the result of the substitution in a compact form

$$\frac{d\mathbf{f}(x_3)}{dx_3} = \mathbf{A}(x_3)\mathbf{f}(x_3). \tag{A.23}$$

Matrix **A** integrates elements, which are a function of the Lamé parameters, wavenumber or frequency and are depth dependent. Vector **f** contains displacement eigen-functions. The vector is depth dependent and takes account for displacement and stress of particles. To the previous stated $\tilde{R}_1^E(k(\omega), \omega, x_3)$ and $\tilde{R}_2^E(k(\omega), \omega, x_3)$, two additional functions are added to describe the additional stress-components

$$\sigma_{3\alpha} = \tilde{R}_3^E(k(\omega), \omega, x_3)e^{i(\omega t - kx_\alpha)}, \tag{A.24a}$$

$$\sigma_{33} = i\tilde{R}_4^E(k(\omega), \omega, x_3)e^{i(\omega t - kx_\alpha)}. \tag{A.24b}$$

Of course, for those two functions the boundary conditions have to be valid as well. We obtain

$$\tilde{R}_{3,4}^E(k(\omega), \omega, x_3) = 0 \qquad x_3 = 0, \tag{A.25a}$$

$$\mathbf{f}(k(\omega), \omega, x_3) \rightarrow 0 \qquad x_3 \rightarrow \infty. \tag{A.25b}$$

Equation A.23 can be written in matrix form (Aki & Richards, 2002)

$$\frac{d}{dx_3}\begin{bmatrix}\tilde{R}_1^E\\ \tilde{R}_2^E\\ \tilde{R}_3^E\\ \tilde{R}_4^E\end{bmatrix} = \begin{bmatrix} 0 & k(\omega) & \frac{1}{\mu(x_3)} & 0 \\ \frac{-k(\omega)\lambda(x_3)}{\lambda(x_3)+2\mu(x_3)} & 0 & 0 & \frac{1}{\lambda(x_3)+2\mu(x_3)} \\ k(\omega)^2 4\mu\frac{\lambda+\mu}{\lambda+2\mu} - \omega^2\rho(x_3) & 0 & 0 & \frac{k(\omega)\lambda(x_3)}{\lambda(x_3)+2\mu(x_3)} \\ 0 & -\omega^2\rho(x_3) & -k(\omega) & 0 \end{bmatrix}\begin{bmatrix}\tilde{R}_1^E\\ \tilde{R}_2^E\\ \tilde{R}_3^E\\ \tilde{R}_4^E\end{bmatrix}, \tag{A.26}$$

where $\tilde{R}_3^E(k(\omega),\omega,x_3) = \mu(\frac{d\tilde{R}_1^E}{dx_3} - k\tilde{R}_2^E)$ and $\tilde{R}_4^E(k(\omega),\omega,x_3) = (\lambda+2\mu)\frac{d\tilde{R}_2^E}{dx_3} + k\lambda\tilde{R}_1^E$. This system represents a linear differential eigenvalue problem with the displacement eigenfunctions $\tilde{R}_{1,2}^E$ and stress eigenfunctions $\tilde{R}_{3,4}^E$. All functions are related to wavenumber, angular frequency and depth. A solution can be derived by reformulating equation A.26 and taking right parts of the equal sign to the left. These terms could be expressed as a Rayleigh wave functional $\tilde{F}_R$

$$\tilde{F}_R(\lambda(x_3), \mu(x_3), \rho(x_3), k_{NM}, \omega) = 0. \tag{A.27}$$

This expression is also called Rayleigh dispersion equation or Rayleigh secular function. Solution A.27 is obtained for special wavenumber eigenvalues k_{NM}. Subscript N^M indicates different modes. For a medium that comprises a finite number of layers, the number of modes is also finite (Lai & Rix, 1998; Ewing et al., 1957). Solving this equation for certain medium properties renders a dispersion curve. This forward modeling of a dispersion curve is the basis of our inversion scheme discussed in Chapter 5.

B. Velocity reversal

It can occur that a velocity reversal in the subsurface is present where the wave velocity decreases with depth due to a low velocity layer. Such a low velocity layer can lead to erroneous results and interpretations. To illustrate those effects, a three layer model with velocity reversal is inverted. The model parameters are given in Table B.1 and the inversion search space in Table B.2.

Table B.1: Model parameters

	$v^S[\mathrm{ms}^{-1}]$	$v^P[\mathrm{ms}^{-1}]$	$\rho[\mathrm{gcm}^{-3}]$	d[m]
layer 1	450	1500	2	5
layer 2	300	1000	1.7	5
layer 3	600	2000	2.3	-

Table B.2: Search space

	$v^S[\mathrm{ms}^{-1}]$	d[m]
layer 1	100-400	3-10
layer 2	400-600	3-10
layer 3	600-1000	-

Although a high velocity contrast is present, only a few inversions resolve the velocity reversal. Inversion results with various combinations of Rayleigh and Love wave modes are shown in Figure B.1. Separate inversions of Love and Rayleigh waves do not provide a consistent subsurface model. Most of them indicate a velocity increase with depth instead of a reversal. However, the Rayleigh wave inversions resolve better the velocity reversal than Love waves. The more modes we integrate, the better should be the resolution (Song et al., 2007). In fact, separate Love wave inversion only seems to detect the reversal by including both higher order modes whereas all other combinations failed. If we look to joint inversions of Love and Rayleigh waves, we see that they uniquely recognize the velocity reversal.

As a summary, joint inversions of Rayleigh and Love waves produce the best results and can identify a velocity reversal although, the low velocity layer is usually overestimated. This can be observed in almost every dispersion inversion. Remarkable as well is that Rayleigh wave inversions are more accurate than Love wave inversions and therefore resolve all three layers.

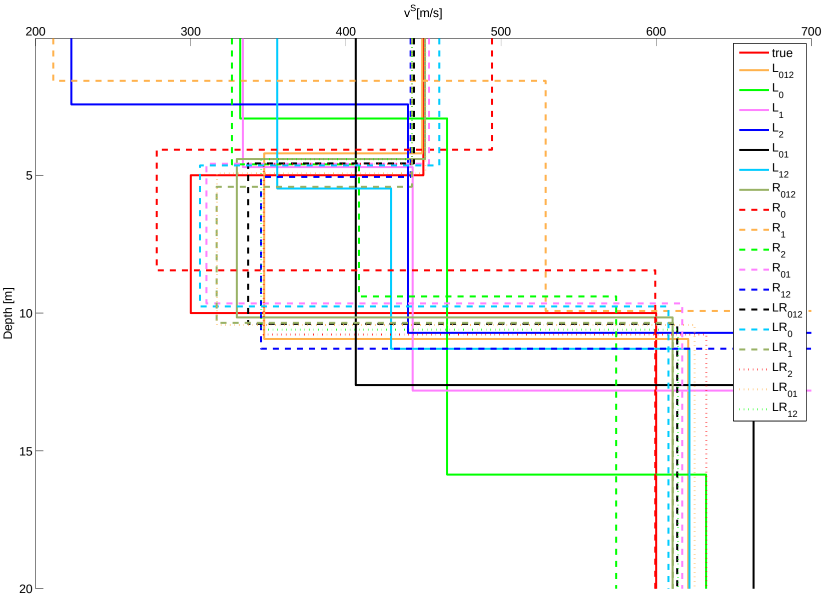

Figure B.1: Inversion results, obtained from the model given in Table B.2, are plotted in a depth-profile.

C. Extraction of refraction information

Picking refraction events or more precisely first arrivals in a seismogram provide us information about the true (subsurface) model. Two *Matlab*^{TM} scripts are mainly used and written for preparing and plotting data. They are originally implemented by H. Maurer[1] and adapted to crosshole seismics by S. Marelli and E. Manukyan[2].

The script *processini.m* reads in the raw data given in SEG-Y and SEG-2 format. Extra information, which is not contained in those data files, has to be manually specified. It can happen that there are so-called dead traces present in the seismogram. Dead traces are receiver records, which do not possess useful seismic information. They can be cancelled out in a created *Excel*^{TM} sheet. Further processing comprises a trace normalization. The filter is an optional tool to surpress undesired frequencies. All information is then sorted and saved in a binary file. The prepared file is further loaded with *picktool.m*. It includes a variety of possibilities to plot processed data. First arrivals can so be picked in the amplitude-travel time image or in a wiggle plot. Although, there is the possiblity to automatically adjust manual picks, this tool is ignored. Picked points and their related values are saved in a simple data file.
Two aspects of first break picking should be kept in mind. In the presence of high frequency guided waves, a high-cut filter is employed and second, the air wave is muted away in low velocity media (Ivanov et al., 2000a). There are cases where refracted waves cut the straight air wave line two times in the seismogram. The resulting velocities obtained by the refraction analysis should be compared then with the air wave velocity $v = 343\text{ms}^{-1}$ to avoid misinterpretations.
After we picked the first arrivals, we use equation 2.29 to attain the velocity and thickness information of each layer. In most cases, however, the number of layers cannot be uniquely determined. The higher the velocity contrast between layers, the easier the separation of different slopes in the travel time-offset plot. Hence, a subsurface with continuous or slight velocity changes across a layer boundary are nearly invisible by looking at first arrivals. In addition, accuracy is best where the first arrival line for a specific layer can be followed over a long offset range. This is often true for the first and deepest layer but depends, of course, on the thickness and velocity of the layers.

---

[1] Professor at the Institute of Applied and Environmental Geophysics, ETH Zürich

[2] PhD-students at the Institute of Applied and Environmental Geophysics, ETH Zürich

D. Expanded experimental data analysis

We study and discuss in this section further results obtained from the Visp data inversions.

D.1. Statistics of the joint Love and Rayleigh wave inversion

Each inversion result was selected among 30 other locally minimized starting models. The mean and standard deviation of the 30 models show, how reliable our final inversion result is. Often, the global minimum is not achieved and the inversion process terminates because the iteration number exceeds a certain limit. The result with the lowest cost-function value is then assumed to be the final result. Here, means and standard deviations of the joint Love and Rayleigh wave inversion are listed in Table D.1. We see

Table D.1: Statistic of the joint Love and Rayleigh inversion of 2, 3 and 4 layers in line 2: considered are the 30 local minimized models for each joint inversion run.

Inversion	Layers	v_1^S[ms^{-1}]	v_2^S[ms^{-1}]	v_3^S[ms^{-1}]	v_4^S[ms^{-1}]	d_1[m]	d_2[m]	d_3[m]	C[ms^{-1}]
L_0R_0	2	149.6	149.6	-	-	1.0	-	-	16.7
mean	2	151.5	248.2	-	-	4.4	-	-	17.5
std	2	0.5	22.6	-	-	0.8	-	-	0.2
L_0I_0	2	158.2	158.3	-	-	0.8	-	-	12.2
mean	2	169.6	301.6	-	-	6.0	-	-	21.2
std	2	2.7	112.0	-	-	2.1	-	-	2.6
L_0R_0	3	146.4	211.4	459.3	-	2.7	12.2	-	12.7
mean	3	147.1	211.9	272.3	-	2.7	12.2	-	12.9
std	3	1.3	8.6	57.7	-	0.5	1.2	-	0.3
L_0I_0	3	149.1	227.3	648.2	-	3.4	16.4	-	12.3
mean	3	147.4	215.2	503.2	-	2.9	13.4	-	12.5
std	3	1.6	11.7	89.9	-	0.6	2.3	-	0.3
L_0R_0	4	145.7	187.4	281.5	507.4	2.2	6.6	12.3	12.2
mean	4	146.4	206.9	304.0	498.4	2.6	8.5	9.6	12.5
std	4	0.7	12.4	59.6	38.0	0.2	2.3	4.5	0.1
L_0I_0	4	170.4	222.8	348.6	892.1	3.3	9.2	16.8	19.6
mean	4	146.6	206.9	304.0	498.4	2.6	8.5	9.6	12.5
std	4	0.6	29.8	66.2	128.9	1.1	3.5	4.5	0.2

that in the two uppermost layers, the velocity deviations are less than 10% of the mean. The deviations calculated for the thicknesses lie between 5-40% of the mean for the first and second layer. These deviations reflect the observations we made in the synthetic and real data. Thicknesses can be resolved much worse than velocities with the dispersion curve analyses. For deeper layers, the deviations become larger.

A comparison between L_0R_0 and L_0I_0 inversion with respect to their standard deviations show that results from a L_0R_0 inversion are better determined. Fundamental Love and inline Rayleigh wave inversions vary stronger and therefore, L_0R_0 results should be preferred.